Study of Small-Scale Features observed in Solar Atmosphere

A thesis

submitted for the degree of

Doctor of Philosophy

in

The Department of Physics,

Pondicherry University,

Puducherry - 605 014, India

by

Nancy Narang

Indian Institute of Astrophysics,

Bangalore - 560 034, India

July 2019

Study of Small-Scale Features observed in Solar Atmosphere

Nancy Narang
Indian Institute of Astrophysics

Indian Institute of Astrophysics
Bangalore - 560 034, India

Title of the thesis	:	**Study of Small-Scale Features observed in solar atmosphere**
Name of the author	:	**Nancy Narang**
Address	:	Indian Institute of Astrophysics II Block, Koramangala Bangalore - 560 034, India
Email	:	nancy@iiap.res.in
Name of the supervisor	:	**Prof. Dipankar Banerjee**
Address	:	Indian Institute of Astrophysics II Block, Koramangala Bangalore - 560 034, India
Email	:	dipu@iiap.res.in

Declaration of Authorship

I hereby declare that the matter contained in this thesis is the result of the investigations carried out by me at the Indian Institute of Astrophysics, Bangalore, under the supervision of Prof. Dipankar Banerjee. This work has not been submitted for the award of any other degree, diploma, associateship, fellowship, etc. of any other university or institute.

Signed: _____

Date: _____

Certificate

This is to certify that the thesis entitled **'Study of Small-Scale Features observed in Solar Atmosphere'** submitted to the Pondicherry University by Ms. Nancy Narang for the award of the degree of Doctor of Philosophy, is based on the results of the investigations carried out by her under my supervision and guidance, at the Indian Institute of Astrophysics. This thesis has not been submitted for the award of any other degree, diploma, associateship, fellowship, etc. of any other university or institute.

Signed: _____

Date: _____

List of Publications

1. *Statistical study of network jets observed in the solar transition region: A comparison between coronal holes and quiet sun regions*
   N. Narang, R. T. Arbacher, H. Tian, D. Banerjee, S. R. Cranmer, E. E. DeLuca, S. McKillop, 2016, **Solar Physics**, 291, 1129-1142

2. *Association of calcium network bright-points with underneath photospheric magnetic patches*
   N. Narang, D. Banerjee, K. Chandrashekhar, V. Pant, 2019, **Solar Physics**, 294:40

3. *High-frequency dynamics of an active region moss as observed by IRIS*
   N. Narang, V. Pant, D. Banerjee, T. V. Doorsselaere, 2019, **Frontiers in Astronomy and Space Sciences**, 6:36

4. *IRIS view on two-component structure of the transition region emission lines*
   N. Narang, H. Peter, H. Tian, D. Banerjee, 2019, **Astronomy & Astrophysics**, in preparation

Conference Proceedings

1. *Association of calcium network brightness with polar magnetic fields*
   N. Narang, K. Chandrashekhar, V. Pant, D. Banerjee, 2018, **Proceedings of the International Astronomical Union**, Volume 13, IAUS 340

Presentations

1. Oral Presentation in *37th Annual Meeting of the ASI*, at CHRIST (Deemed to be University), Bangalore during 18-22 February 2019.

2. Poster Presentation in *IRIS 9 Meeting*, at Max-Planck Institute for Solar System Research, Goettingen during 25-29 June 2018.

3. Poster Presentation in *IAU Symposium 340*, at B. M. Birla Auditorium, Jaipur during 19-23 February 2018.

4. Oral Presentation in *Joint HINODE 11/ IRIS 8 Meeting*, at Bell Harbor Conference Centre, Seattle during May 30-2 June 2017.

5. Oral Presentation in *IRIS 7 Workshop*, at Shandong University, Weihai during 11-15 April 2016.

6. Poster Presentation in international conference on *Dynamic Sun I: MHD Waves and Confined Transients in the Magnetised Atmosphere*, at IIT BHU, Varanasi during 22-26 February 2016.

7. Poster Presentation in *IRIS 5 Workshop*, at IUCAA, Pune during 26-29 October 2015.

8. Poster Presentation in *14th International Solar Wind Conference*, at Shandong University, Weihai during 22-26 June 2015.

Dedicated to

my

Grandmother

Acknowledgements

There are few people I wish to thank for their sustained guidance, friendship and support during the five years I spent at IIA for my Ph.D. Firstly, I want to thank my supervisor Prof. Dipankar Banerjee for providing me with his help and guidance which has made me understand what research is all about. I am grateful to him for his invaluable support in my research and personal life.

I thank all my collaborators for their valuable guidance. I extend my gratitude to the referees of my papers and doctoral committee members for their insightful comments that have helped me to improve the quality of my research work. I thank IIA for providing me with necessary facilities to carry out the research work.

I express my sincere thanks to all my friends at IIA with whom I had great times. I would like to convey my special thanks to Bhoomika who has been my best friend throughout. We had many good laughs and together we cherished many of our common hobbies. I also thank her for the unconditional support which she provided me in my good and bad times.

Leaving the best for the last, I am deeply indebted to my family for their encouragement and faith in me. A big thanks from the bottom of my heart to my husband Chandrashekhar. Just words cannot express how grateful I am. Thanks for not only encouraging me to pursue my dreams but also for being understanding and helpful throughout the thesis. I owe him a million thanks for his invaluable love and support, which I will cherish throughout my life.

Data Usage Acknowledgements

Data from various space-based instruments are used in the studies presented in the thesis. I duly acknowledge the usage of the data from these facilities, and I thank the respective instrument team members for providing the data in the public domain.

Hinode is a Japanese mission developed and launched by ISAS/JAXA, with NAOJ as domestic partner and NASA and STFC as international partners. It is operated by these agencies in co-operation with ESA and NSC.

IRIS is a NASA small explorer mission developed and operated by LMSAL with mission operations executed at NASA Ames Research center and major contributions to downlink communications funded by ESA and NSC.

SDO data is supplied, courtesy of the SDO/HMI and SDO/AIA consortia. SDO is the first mission to be launched for NASA's Living With a Star (LWS) Program.

Abstract

The solar atmosphere is populated with various small-scale features which are observed to be very dynamic and highly structured. The advent of modern instruments with high spatial, spectral and temporal resolution, have aided us to study the evolution and different dynamical properties of the fine-scale structures. This thesis is a compilation of detailed analysis of different small-scale features and events as observed in the solar chromosphere and transition region. The chromosphere and transition region act as an interface between highly dense but cool photospheric plasma and hot low dense coronal plasma. Together, known as interface region, chromosphere and transition region play a key role in mass and energy supply from photosphere to corona. These layers are home of various small-scale features and events which are being proposed to play a vital role in coronal heating and acceleration of solar wind. The statistical study of various properties of the some of the small-scale features is the aim of the thesis. The effect of the magnetic field in generation and evolution of the features is also investigated.

We have explored the possible association of polar network bright points, observed in chromopshere, with the photospheric magnetic fields using special *HINODE* campaigns devoted to observe polar regions of the Sun. The intensity of such bright points is found to be correlated well with the underneath photospheric magnetic field strength with a linear relation existing between them. These chromospheric Ca H bright points seems to be co-spatial with groups of G-band bright points in the photosphere. This indicates that these different features are directly coupled with each other. Though, present in different layers of the solar atmosphere they happen to be manifestations of the magnetic field concentrations present in the lower photosphere.

We have performed a statistical study of network jets and estimated their dynamical properties using IRIS C II 1330 Å images. We have reported that the coronal hole jets appear to be faster and longer than those in the quiet sun. In spite of different magnetic

structures in the coronal hole and quiet sun in transition region, there appears to be no substantial difference for the increase in foot-point brightness of the jets. This has led us to infer that the generation mechanism of these network jets is likely the same in both regions. Whereas, the larger speeds and extents of the jets in coronal holes can be attributed to the presence of open magnetic field lines in coronal holes in comparison to the quiet-sun.

Using joint spectral and imaging observations of IRIS, we have investigated the sources responsible for origin of the two-components of the double Gaussian profiles deduced from Si IV 1403 Å transition region emission line. A very close spatial association is observed between the raster images of the spectral properties with intensity in IRIS images and magnetic field in magnetograms. By the statistical analysis, we have showed that the double Gaussian fitting model is preferred over the single Gaussian model in bright network regions and neighbouring locations. On comparison with IRIS images, these locations can be seen to be associated with the complex jet structures and thus are claimed as signatures of transition region transients.

We have studied the dynamics of high-frequency oscillations of an active region moss as recorded by simultaneous imaging and spectral data of IRIS. Power maps generated from IRIS images in Si IV 1400 Å passband and sit-and-stare spectroscopic observations of Si IV 1403 Å spectral line reveal the presence of high-frequency oscillations with periodsof 1–2 minutes. The presence of such short periods is further confirmed by intrinsic mode functions (IMFs) as obtained by empirical mode decomposition (EMD) technique. We find evidence of presence MHD waves as well as repetitive reconnection events that can be held responsible for the observed short-period variability in the bright moss regions.

Contents

List of Figures

List of Tables

Abbreviations

JAXA	**J**apan **A**erospace E**X**ploration **A**gency
ISAS	**I**nstitute of **S**pace and **A**stronautical **S**cience
NAOJ	**N**ational **A**stronomical **O**bservatory of **J**apan
STFC	**S**cience and **T**echnology **F**acilities **C**ouncil
SOT	**S**olar **O**ptical **T**elescope
NASA	**N**ational **A**eronautics and **S**pace **A**dministration
ESA	**E**uropian **S**pace **A**gency
NSC	**N**orwegian **S**pace **C**entre
LMSAL	**L**ockheed **M**artin **S**olar and **A**strophysics **L**aboratory
IRIS	**I**nterface **R**egion **I**maging **S**pectrograph
SDO	**S**olar **D**ynamics **O**bservatory
AIA	**A**tmospheric **I**maging **A**ssembly
HMI	**H**elioseismic and **M**agnetic **I**mager
MHD	**M**agneto**H**ydro**D**ynamics
CCD	**C**harge **C**oupled **D**evice
NUV	**N**ear **U**ltra**V**iolet
FUV	**F**ar **U**ltra**V**iolet
EUV	**E**xtreme **U**ltra**V**iolet
UT	**U**niversal **T**ime
TR	**T**ransition **R**egion
$\mathbf{R}_\odot$	Solar **R**adius
AU	**A**stronomical **U**nit

Chapter 1

Introduction

The Sun is a second-generation star, formed by the coalescence of material left by first-generation stars in our Galaxy that underwent supernova explosions. The Sun is a fairly ordinary star of spectral type G2 V and absolute stellar magnitude 4.8, but of course its proximity to the Earth makes it unique. The Sun is about 4.6 billion years old and is approximately half-way through its main sequence phase (10^{10} years) of life. With effective temperature of 5785 K, it has a mass of $\sim 1.99 \times 10^{30}$ kg and radius equal to 6.955×10^{8} m. The Sun is such a massive plasma ball that it is held together and compressed by its own gravitational attraction. It comprises mainly H (92%) and He (8%) atoms by number, mostly ionised due to the high temperature; the remaining elements, such as C, N and O, total about 0.1% and are present in roughly the same proportions as on Earth. The mean distance from the Earth to the Sun is 149.6 million km, which takes light 8 minutes to travel. Being the heart of the solar system, it has profound effects on the Earths climate and on space weather, and its study is of central importance for understanding the behaviour of stars and of cosmic plasma in general. The overall structure of the Sun is described briefly in the following sections.

1.1 The Solar Interior

The solar interior is divided into three regions, as sketched in Figure 1.1, namely the core, radiative zone, and convection zone. Energy is generated in the Sun's core by nuclear reactions, in particular, fusion of four protons to form 4 He nuclei. This energy leaks continuously outwards in a very gentle manner across the *radiative zone ($0.25R_\odot$ to $0.7R_\odot$)* by radiative diffusion, as the photons are absorbed and emitted many times, taking many years to cross it. In the *convection zone ($0.7R_\odot$ to $1.0R_\odot$)*, convection is the dominant means of outward energy transport. Convection transports energy because an individual blob of plasma carries heat as it rises and then gives up some of it before falling and picking up more. At the lower boundary of the convection zone, there exists a strong shear layer, called the *tachocline* (Spiegel and Zahn 1992), where much of the Sun's large-scale magnetic field is believed to be generated. The solar interior is so incredibly opaque that, whereas an unimpeded photon would take 2 sec (at the speed of light) to reach the surface from the center, there are so many collisions (absorptions and re-emissions) that photons in practice take 170,000 years for the journey (Mitalas and Sills 1992). The effect of these collisions is to increase the typical wavelength from that of high-energy gamma rays in the core to visible light at the solar surface, where most of the energy generated in the core is radiated into space.

1.2 The Solar Atmosphere

The solar atmosphere is defined as the part of the Sun from which the energy generated in the Sun's core escapes into space as radiation. It consists of four different regions (showcased in Figure 1.1), namely, *photosphere, chromosphere, transition region (TR)* and *corona*. The lowermost layer, *photosphere*, is the visible surface layer of the Sun. It is an extremely thin layer of plasma, only several

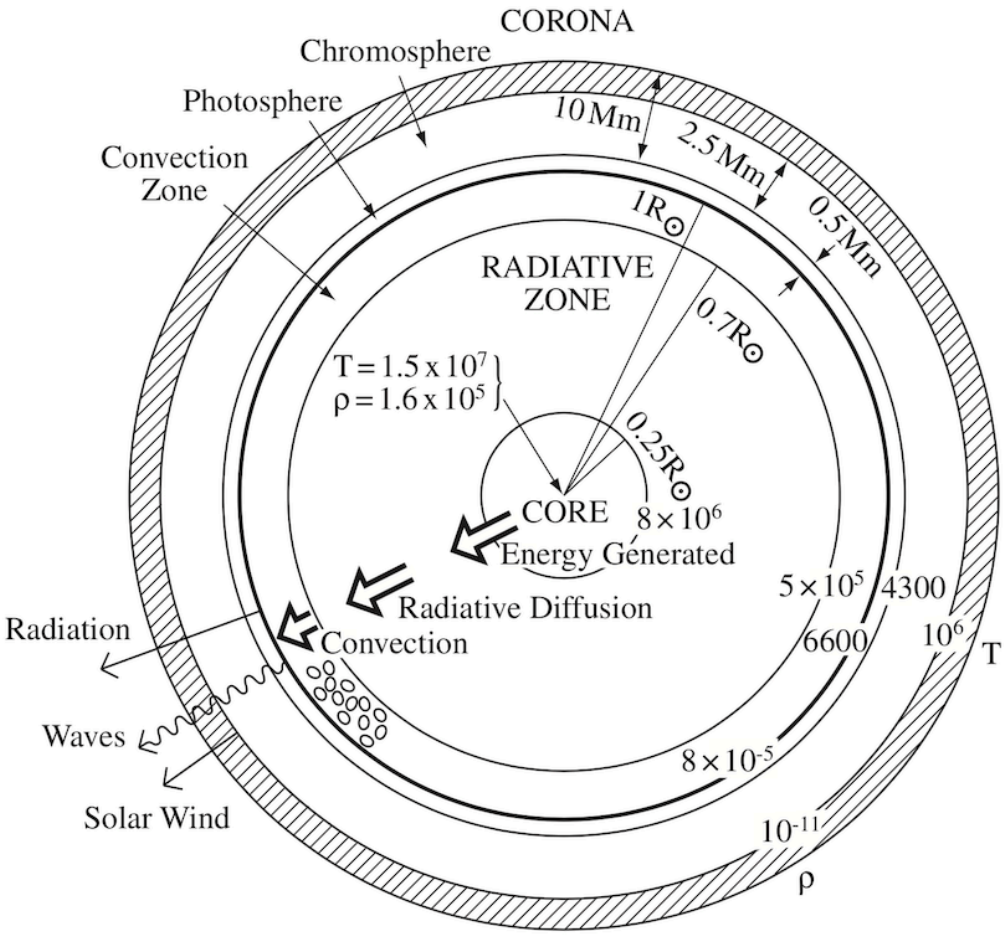

FIGURE 1.1: The overall structure of the Sun, indicating the sizes of the various regions and their temperatures (in K) and densities (in $kg\,m^{-3}$). The thickness of the various regions are not drawn to scale, and the boundary between chromosphere and corona is highly variable between 2.5 and 15 Mm, as indicated by the shaded region. *Image Credit: Priest (2014).*

hundred kilometers thick, which is relatively dense and opaque and emits most of the solar radiation. The base of the photosphere is generally defined as the layer where the optical depth τ is unity for radiation of wavelength 5000 Å, written $\tau_{5000} = 1$. It has an optical thickness $\tau \leq 1$ in the near-ultraviolet, visible and near-infrared continua, but is optically thick in all except the weakest spectral lines.

Above the photosphere lies the rarer and more transparent *chromosphere*, which is optically thin in the near-ultraviolet, visible and near-infrared continua, but is

optically thick in strong spectral lines. The *corona* extends from the top of a narrow *transition region* and out into the *solar wind*, which fills the *heliosphere*. The corona is optically thin over the whole electromagnetic spectrum, except for radio waves and a few spectral lines. The densities are very low in the solar corona as compared to photosphere or chromosphere. The number density (N) decreases rapidly with height: typical values are $10^{23}\,m^{-3}, 10^{19}\,m^{-3}, 10^{15}\,m^{-3}$ and $10^{13}\,m^{-3}$ in the photosphere, chromosphere, transition region, and corona.

The photosphere has an average temperature of $\sim$5700 K. By the First Law of Thermodynamics, the temperature continuously falls with distance from the energy-generating region at the Sun's core. This fall-off of temperature would be expected to continue in the solar atmosphere, starting from the base of the photosphere. In fact, the temperature rises, eventually reaching extremely large values, giving rise to an upper atmosphere which emits radiation at extreme ultraviolet and X-ray wavelengths.

According to the well- known *VAL model* (Vernazza *et al.* 1981) of average solar atmosphere, shown in Figure 1.2, there is a fall-off of temperature from about 6600 K (at the bottom of the photosphere, $\tau_{5000} = 1$), to a minimum value of $\sim$4400 K at a height of about 500 km above $\tau_{5000} = 1$ (the temperature minimum level). Above the temperature minimum, the temperature rises slowly through the chromosphere to form a broad plateau at $\sim$6000 K, over a height range of approximately 1000–2000 km. The temperature rises dramatically through the transition region (less than 100 km thick) to a few million degrees in the corona (Figure 1.2). Thereafter, it falls slowly in the outer corona, which is expanding outwards as the solar wind, to a value of 10^5 K at 1 AU. Figure 1.2 shows (solid curve) the variation of the temperature in the lower part of the solar atmosphere (heights up to 30000 km above the $\tau_{5000} = 1$ level), together with variations in the number densities (cm^{-3}) of neutral hydrogen (N_H) and free electrons (N_e), according to the three quiet-Sun models (Vernazza *et al.* 1981; Fontenla *et al.* 1990; Gabriel 1976).

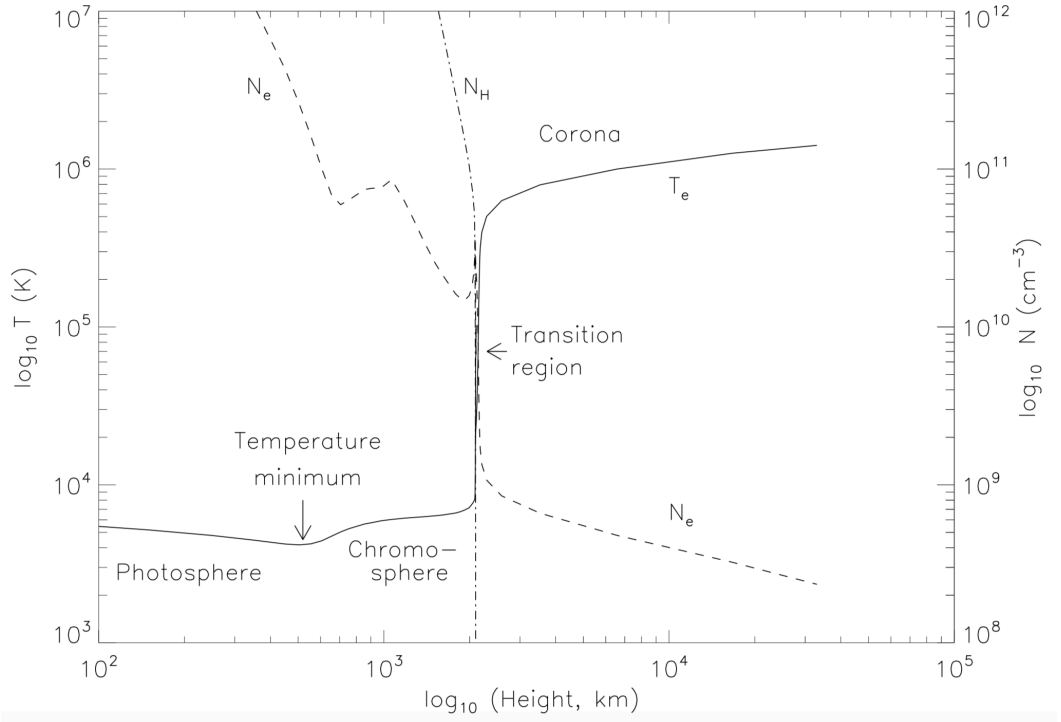

FIGURE 1.2: The variation of temperature with height in the solar atmosphere (solid curve), based on one-dimensional model calculations of Vernazza *et al.* (1981); Fontenla *et al.* (1990); Gabriel (1976). The chromospheric and transition region part of this model atmosphere is for the average quiet Sun. Based on these idealized representations of the solar atmosphere, the transition region is a thin layer with $T = 10^5$K separating the chromosphere and corona. Variations in the number densities (cm^3) of neutral hydrogen atoms (N_H) and electrons (N_e) (dotdash and dash curves respectively) are also shown. *Image Credit: Phillips et al. (2012).*

The *VAL model* of the solar atmosphere is a semi-empirical one-dimensional model that successfully fits a number of spectral lines from different regions and has been extremely useful. However, a representation such as in the Figure 1.2 of the atmospheric structure is a gross oversimplification, which indicates only the mean properties. The solar atmosphere is, in reality, a highly inhomogeneous, time-dependent non-equilibrium plasma with a far-from-uniform structure. The temperature and density at any location are continually changing as plasma heats and cools dynamically over tiny as-yet-unresolved length-scales and moves around in response to a variety of different physical processes. Indeed, along any line of

sight, there is an enormous range of temperatures. Thus, for instance, transition-region emission comes not in reality from a 100 km thick layer, but from plasma at many different heights that is heating up or cooling down through transition-region temperatures.

By a combination of theoretical advances (both analytical and computational), ground-based observations (from GONG and BiSON networks and from telescopes in La Palma, Tenerife, Sacramento Peak, Big Bear, and Kitt Peak) and especially space observations (mainly from Skylab (1973), Yohkoh (1991), Ulysses (1992), SoHO (1995), TRACE (1998), RHESSI (2002), STEREO (2006), Hinode (2006), SDO (2010) and IRIS (2013)), it has gradually become clear that much of the Sun's present observed structure and dynamic behaviour is due to the solar magnetic field. All aspects of solar activity owe their existence to the variation of magnetic field and represent different ways in which solar plasma is responding to the underlying magnetic field evolution. For instance, the *active Sun* generally consists of large scale magnetic features and transient phenomena, such as sunspots, prominences, flares and coronal mass ejections, which are caused by the presence and evolution of stronger ($>$1 kG) magnetic fields. The *quiet Sun* is also influenced markedly by the magnetic field ($\leq$1 kG), with smaller spatial structures; it is structured by the magnetic network above and around evolving granular and supergranular cells. The heating of the solar atmosphere, generally referred as *"coronal heating"*, can also be understood as an effect of different phenomena of the solar magnetic field at various spatial and time-scales.

In a nut-shell, the evolution of the complex magnetic structures at various scales in the different layers of the solar atmosphere determines the energetics of the atmosphere. This thesis is focussed on the study of some of the small-scale phenomena, in particular, observed in the solar chromosphere and transition region. Primarily the observations from *Solar Optical Telescope* (SOT, Tsuneta *et al.* (2008b)) and *Interface Region Imaging Spectrograph* (IRIS, De Pontieu *et al.* (2014b)) are used

for studying the chromosphere and transition region in the thesis (details of the instruments are provided in Chapter 2).

1.3 Significance of Chromosphere and Transition Region

The high temperatures of the chromosphere and corona, much exceeding the photospheric temperature, are departures from those expected from physical considerations. A heating mechanism, due to some non-radiant energy source, is therefore required. This energy source, as well as the structured nature of the chromosphere and corona is strongly correlated with the Sun′s magnetic field, a fact that is readily observed: regions of the solar atmosphere hotter than their surroundings, as deduced from their ultraviolet and X-ray spectra, are highly correlated with regions in the photosphere associated with the strong magnetic field. Understanding how the chromosphere is heated to 10^4 K and the corona to 10^6 K, by comparison with the photosphere at 6000 K, is a major challenge in astronomy (Klimchuk 2006; Reale 2010; Parnell and De Moortel 2012). Two major approaches to account for atmospheric heating are: (i) energy dissipation through magnetohydrodynamic (MHD) waves, and (ii) energy deposition through magnetic reconnection.

Coronal heating is only a few percent of chromospheric heating. The heating requirement for the chromosphere is at least an order of magnitude greater than for the corona, so a comprehensive model needs to treat the generation, propagation and dissipation of energy through the whole atmosphere. This includes the continual transfer to and fro of mass and energy between chromosphere and corona and the fact that transition-region plasma is material that happens to be heating up and cooling down dynamically through 10^5 K. The VAL model is the mean model of the solar atmosphere and assumes thermodynamic properties varying

only with height and are static. The model is important as a standard. However, the chromosphere and transition region are highly non-uniform and dynamic and far from a static plane-parallel "average" state. They are filled with a wide range of fine-scale flows, inhomogeneities and wave motions. Many recent observations and numerical simulations have also revealed the filamentary and time-dependent response of the overlying atmosphere to photospheric convection.

Observations, therefore, show that model atmospheres, while useful in describing the way in which temperature rises (and density decreases) with height, have limitations in that the high degree of structuring in the chromosphere and corona is not properly reproduced. The nature of the transition region, predicted to be a thin layer separating the chromosphere and corona in models, is also quite different in reality. It is not a narrow static horizontal layer but represents all the plasma that happens to be at transition region temperatures while heating up or cooling down to $\sim 10^5$ K. The chromospheric plasma is also continually accelerated, heated and cooled in a dynamic way, with some of the plasma heated to transition-region temperatures and most flowing back down. Only a small fraction is heated to coronal temperatures, and some flows out as the solar wind in open-field regions.

Chromosphere and transition region, together referred as *Interface Region*, are non-LTE region of transitions between photosphere and corona; from high to low beta, from optically thick to optically thin and from partially ionised to fully ionised plasma. It is important to study the complex behaviour of the dynamic, highly inhomogeneous interface region in order to understand the nature of the atmospheric heating. The interface region is coupled in complex ways to the overlying corona and mediates the energy flux from photosphere that heats the corona and drives the solar wind.

The solar chromosphere is observable in visible and near-ultraviolet (NUV) wavelengths ($\sim$6500 Å to 1600 Å). The chromosphere is often observed in Hα (Hydrogen

Balmer-α) absorption line at 6563 Å, which is most important for following the evolution of active regions and prominences and for observing the low-temperature part of solar flares. The lower chromospheric emission, Ca II H & K lines at 3968 Å & 3933 Å, reveals a *network* of supergranulation boundaries very clearly as an irregular bright pattern. As one goes higher in the solar atmosphere, the magnetic field above supergranule boundaries continues to spread out, causing the network to thicken with increasing temperature, and eventually, at coronal heights it ceases to exist. The upper chromosphere, observed with for *e.g.* Mg II h & k lines at 2803 Å & 2796 Å shows up like a forest of plasma jets called "spicules". Though the spicules are observed throughout the chromosphere, in the upper chromosphere they dominate the scene.

The transition region (TR) emission falls in the far-ultraviolet (FUV) and extreme-ultraviolet (EUV) wavelength ranges (∼1600 Å – 400 Å). Direct imaging of the TR is often achieved using the filters centered at the He II 304 Å, C II 1330 Å, and Si IV 1400 Å emission lines. The most prominent features in TR intensity images are the network structures. The TR network lanes are the upward extensions of the chromospheric network lanes. The sizes of the network lanes are generally larger than those in the chromosphere, which are likely a reflection of the expansion of magnetic flux tubes with height. As proposed by Dowdy *et al.* (1986), the dominant magnetic field structures in the network change from small loops to funnels through the TR (Figure 1.3). The TR emission lines are known to be red-shifted on average. The average Doppler shift turns from red-shift to blue-shift when the temperature is higher than ∼0.5 MK. The most intensively studied TR dynamics are the so-called TR explosive events, which are characterized by enhanced wings of TR line profiles. It is generally believed that bidirectional flows generated by magnetic reconnection are responsible for the enhanced wings.

Most of the upper chromosphere and TR emission is present generally in the ultraviolet spectral range. Imaging and spectroscopic observations in this spectral

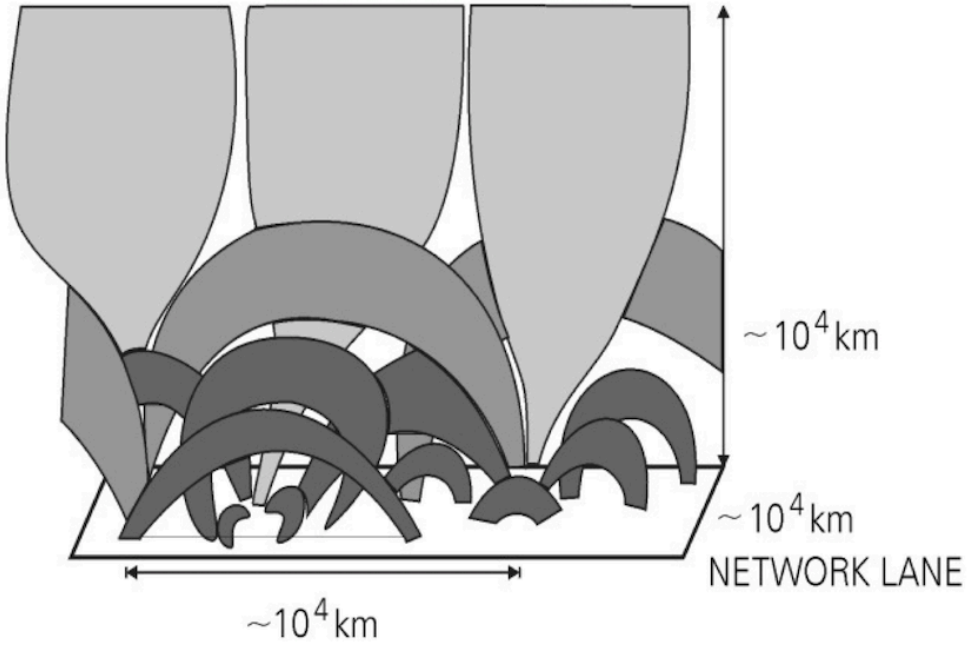

FIGURE 1.3: Magnetic field structures of the solar atmosphere (Dowdy *et al.* 1986). The TR network lane consists of both low-lying loops and locally open field lines.

range provide important avenues to obtain information about the physics of these regions. Since solar radiation in this wavelength range is almost completely absorbed by Earth's atmosphere, observations from space platform are required to obtain a complete picture of the "interface region".

1.4 Motivation and Aim of the Thesis

In the past decade our understanding of the Sun has been revolutionised by the high-resolution observations, especially from space-based telescopes and instruments, mainly *Hinode*, STEREO, SDO, and IRIS. Recent technological advancements have paved the way to explore the finer structures and fast dynamic phenomena present in the solar interface region. The high spatial and spectral resolution of modern data with an unprecedented cadence has probed the interface region in

greater details and resolved many of the small-scale structures which were previously unexplored due to the instrumental limitations. We are now presented with a picture of the solar atmosphere that is far more dynamic and complex than we ever expected from early spacecraft or ground-based telescopes.

Various small-scale features and phenomena of sub-arcsec sizes and short lifetimes (few seconds) are observed to dominate the interface region. Some examples of such small-scale events observed in the interface region are network bright points, mottles/fibrils, spicules, network jets, surges, ellerman bombs, blinkers, RBEs, RREs, explosive events, multi-component emission lines, UV bursts, umbral & penumbral jets, high-frequency oscillations etc. The persistent presence of such events with their generally high re-occurrence rates make them strong candidates for transport of mass and energy from the photosphere to corona and solar wind. Despite our knowledge on the dynamics of fine-scale structures is advancing with the recent high spatially, spectrally and temporally resolved observations, the solar interface region is still tough to be understood and modeled completely because of its high level of dynamic activity and inhomogeneous nature. It has really been the case that as fast as we solve some problems, others are created that need great ingenuity in finding satisfactory physical explanations.

The aim of the thesis is to study some of the small-scale features observed in the interface region which can possibly shed new light in obtaining a clearer picture of the atmospheric dynamics occurring at smaller spatial and temporal scales. Throughout the thesis, we have adopted a statistical approach to explore the role of the magnetic field in origin and evolution of different small-scale features and events. In particular, a possible relation between chromospheric network bright-points with the similar photospheric features and magnetic field concentrations is obtained by studying 20 such bright-points in Sun's polar region. Studying

∼60 network-jets in the coronal hole (CH) and a similar number in the quiet-Sun (QS) regions, we have performed a comparison between the dynamical properties of these jets between CH and QS regions. A statistical investigation of two-components of Si IV 1403 Å TR emission line is performed to analyse the sources responsible for deviation from single Gaussian line profiles. "High-frequency oscillations" (∼1 minute) observed at various locations of an active region moss are studied and their possible nature of origin is analysed. At the beginning of each chapter (Chapters 3 to 6), a detailed introduction about the phenomenon of interest is provided. The importance of the particular study and further explorations required are also discussed in the respective chapters. The outline of the thesis below briefly mentions the major results drawn from each study.

1.5 Outline of the Thesis

The solar atmosphere is populated with various small-scale features which are observed to be very dynamic and highly structured. The advent of modern instruments with high spatial, spectral and temporal cadence, have aided us to study the evolution and different dynamical properties of the fine-scale structures. This thesis is a compilation of detailed analysis of different small-scale features and events as observed in the solar chromosphere and transition region. The relation of these features with other layers of the atmosphere is also explored. The effect of the magnetic field in generation and evolution of the features is investigated. A summary of each chapter of the thesis is outlined below.

In this introductory chapter (Chapter 1), general properties of the Sun and its atmosphere are described. Detailed properties of chromosphere and transition region are discussed. The importance of small-scale features present in these layers is emphasized. The motivation and primary aim of the thesis is discussed.

Chapter 2 provides the details about the telescopes and instruments from which the different observations are analysed in the thesis. We have primarily used high-resolution observations from space-based observatories to study the small-scale features. Their dynamics and evolution are studied mainly using imaging and spectroscopic data. The important details about the instruments, different observation modes, and data-products are provided in the chapter.

In Chapter 3 a possible relationship between chromospheric polar network bright points with underneath photospheric magnetic patches is discussed. Recent studies have shown that the magnetic patches of strengths $\sim$1 kG coincide in position with polar faculae at the photosphere. We have shown the spatial intermittency of the magnetic field to persist even at the chromospheric level. We have studied 6 polar region observations from SOT on-board *HINODE* and established that the association between the calcium brightness and magnetic field holds good at the finer scales in polar regions of the Sun. We have developed an automated method for identification of calcium network bright points. By employing this method, we find that the bright points mostly exist at the locations of concentrated magnetic field. These chromospheric Ca H bright points seems to be co-spatial with groups of G-band bright points in the photosphere. This clearly indicates that these different features are directly coupled with each other, though present in different layers of the solar atmosphere, and happen to be manifestations of the magnetic field concentrations present in the lower photosphere. Along with considerable spatial association, a good correlation exists between normalized calcium network intensity and photospheric magnetic field strength of the network points with a linear relation between them.

In Chapter 4, a statistical comparison of dynamical properties of the network jets between Coronal Hole (CH) and Quiet Sun (QS) regions is presented. We have analysed different properties of the network jets (mainly apparent speed,

length, lifetime and increase in foot-point brightness) by using four different imaging observations of IRIS: two of which are of CH and two of QS. We observe that statistically, CH jets appear to be faster and longer than those in QS regions. We have described it as a consequence of different magnetic configurations of the two regions with open magnetic field lines dominant in CH and magnetic loops often present in QS. In CHs, open and expanding magnetic flux tubes at network boundaries must be assisting the small-scale network jets to propagate up to larger extents with higher speeds and, hence the jets are accelerated more efficiently in CHs than in QS regions. We find that the apparent speed of the network jets is independent of increase in foot-point brightness, although it is very much dependent on length of the jets. On the other hand, brightness increase at foot- points appears to be independent of any of the dynamical properties of the jets. Thus we have concluded that generation mechanism for origin of the network jets is of very similar nature in CH and QS. However, as the jets propagate in different ambient magnetic environments in the two regions, most of the dynamical properties get considerably effected. The recurrence of these high-speed network jets from the same location suggests that the oscillatory reconnection might be the possible mechanism for generation of the jets. As these jets reach up to higher layers (length of $\sim$ 5 Mm), they can serve as reasonable candidates for supplying mass and energy to the corona and solar wind.

In Chapter 5, we showcase a detailed study the two-component behaviour of the solar transition region (TR) which can account for the asymmetric emission line profiles often observed in the TR. Using simultaneous imaging data of chromosphere and spectral data of TR from IRIS, spectral properties of different components of the observed Si IV (1403 Å) line profiles and their possible relation to corresponding features in the chromospheric images is illustrated with a statistical significance. The technique of R-B asymmetry analysis is successfully employed on automated terms in order to resolve the asymmetric TR line profiles into two components and perform double Gaussian fits. The comparison of χ^2_r between

single Gaussian fit and double Gaussian fit model reveals that the double Gaussian model is a better representation of the data and is preferred over the single Gaussian model in the network regions. From the one-dimensional histograms of the fitted parameters, it is observed that on an average the secondary component of double Gaussian fits contributes about 34% to the total intensity of the line profile. The Doppler velocity distribution for the secondary component shows the excess populations clustering near ± 25 km/s which are indicated to be related to TR transient flows by analysing two-dimensional histograms. With the aid of different two-dimensional histograms, the spectral properties and specific locations of the transients are obtained. These locations predominantly happen to be at the boundaries of the network regions which can be clearly observed to be associated with spicules and network jets in the chromospheric images. It is concluded from the present work that the secondary component of double Gaussian fits indeed reveals the presence of transients in chromosphere and TR. Hence, double Gaussian model fitting to the spectral profiles is necessary to study small-scale short lived transients in details. This is important to obtain a better knowledge of TR structure and dynamics for the study of the mass and energy transport from the photosphere to corona responsible for coronal heating.

In Chapter 6, we illustrate a study of high-frequency dynamics of chromosphere and transition region. We have studied high-frequency oscillations of periods $\sim$ 1–2 minutes in an active region (AR 2376) moss as observed by IRIS. The techniques of wavelet-analysis and empirical mode decomposition (EMD) are employed in order to explore the behaviour of high-frequency oscillations. We have detected the presence of high-frequency oscillations (1–2 minutes) in the power maps of the observed region, deduced from the time-sequence of the images and different spectral parameters. We have reported that the power in shorter periodicities (1–2 minutes) is less than that in larger periodicities (2–4 minutes) and concentrated only in the brighter regions of the moss. EMD technique is further employed to study correlation and phase relationship between the observed spectral parameters

statistically. The observed phase-shifts indicate towards the presence of different wave modes as well as reconnection events to be present. Hence, we conclude that the high-frequency oscillations observed in the bright moss regions are signatures of different MHD waves combined with various reconnection events.

Chapter 7 summarises the entire thesis work. Main conclusions drawn from different studies are outlined here and possible future prospects are also listed.

Chapter 2

Instruments

Techniques and instruments for solar observation are ever changing with time. Early records of solar observations include a clay tablet (dating to 1223 BC). Chinese observations of sunspots, the Book of Changes, compiled in 800 BC. Several such observations, although extensive are irregular. As time progressed observations grew to be more accurate and exhaustive. The solar eclipse of 968 AD was documented in Annales Sangallenses with comments about the corona; Worcester Chronicles from 1128 AD contain drawings of sunspots with details of the penumbral region; Russian Chronicle of Novgorod describes prominences from the 1185 AD solar eclipse. The development of telescopes in the 17th century led to more systematic observations of the Sun, while that of spectroscopy allowed the discovery of the Fraunhofer lines from which the elemental composition of the Sun could be inferred. With the advancement of photography, maintaining daily records became easier. Ground based radio observations started in 1942 and in 1946 space travel enabled one to study the Sun in UV, unconstrained by absorption from the Earths atmosphere. At present, there are several space and ground based solar facilities which work together to refine our understanding of the Sun. The

research involved in this thesis makes use of data from some of these like *HINODE*, Interface Region Imaging Spectrograph (IRIS) and Solar Dynamics Observatory (SDO) and are discussed below.

2.1 Hinode

Hinode (Kosugi *et al.* 2007) was launched from Japan on 22 September 2006 as a collaborative project of institutions in Japan, United States and United Kingdom. The spacecraft was originally called by its development name Solar-B and named *Hinode* (meaning *Sunrise* in Japanese) only after its successful launch, in accordance to Japanese tradition. It is placed in a polar, Sun-synchronous, circular orbit around the Earth at an altitude of about 680 km. From here it can see the Sun continuously for a period of nine months and for the remaining three months it experiences breaks that can last up to 20 minutes during each of its 98 minute orbit when it is eclipsed by the Earth.

The scientific motivation for Hinode is to study the generation, transport and dissipation of magnetic energy. It has three instruments on-board (Figure 2.1), namely, Solar Optical Telescope (SOT), EUV Imaging Spectrometer (EIS) and X-Ray Telescope (XRT), which are designed to observe the response of the chromosphere and corona to the changes in the photospheric magnetic fields. These instruments, generally, work together imaging the same object of interest. However, EIS can be offset with respect to the telescope pointing by 15 arcmin in the East-West direction and XRT observes the full disk. The present thesis make use of observations from SOT, which is described in details further.

FIGURE 2.1: Hinode spacecraft with the positions of the instruments SOT, EIS and XRT. *Image credit:* JAXA

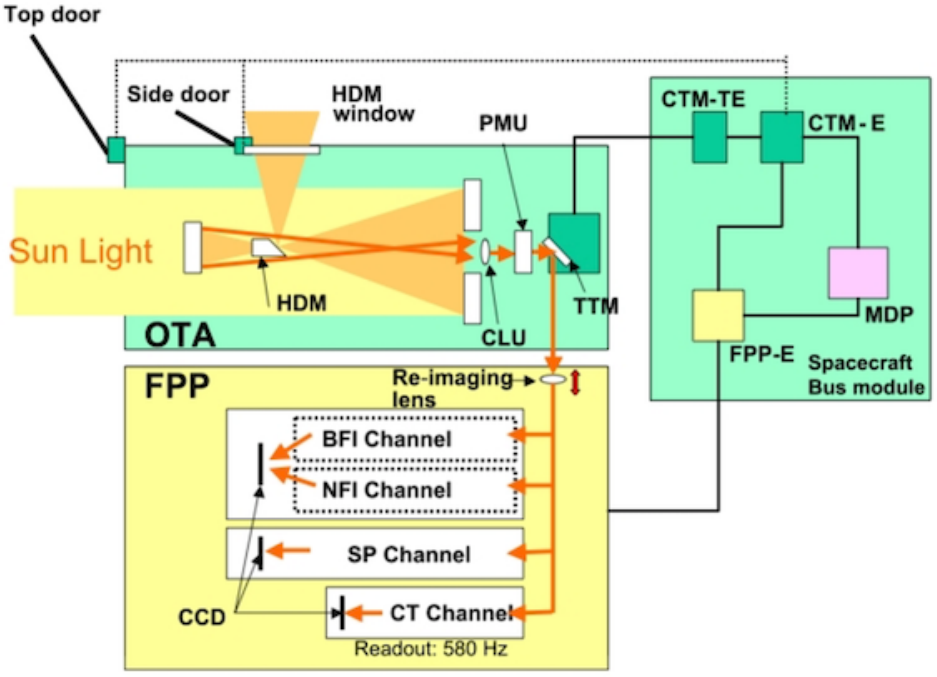

FIGURE 2.2: The working of SOT showing how the light from the OTA is distributed to the different instruments of the FPP and the various components of the Bus module. *Image credit:* Tsuneta *et al.* (2008b)

2.1.1 Solar Optical Telescope

The Optical Telescope Assembly (OTA, Suematsu *et al.* (2008)) and Focal Plane Package (FPP) are two components that make up the Solar Optical Telescope (SOT, Tsuneta *et al.* (2008b)). OTA, the largest optical solar telescope that is flown in space, is a Gregorian telescope which is diffraction limited in the wavelength range of 3880–6700 Å. It has a 0.5 m aperture and a $360'' \times 200''$ FOV. The instrument package of SOT referred to as the FPP includes a beam spitter which divides the incoming light into the Broad-band Filter Imager (BFI), Narrow-band Filter Imager (NFI), Spectro-Polarimeter (SP) and Correlation Tracker (CT). Figure 2.2 shows how the OTA and FPP work together. The FPP performs both filter (FG) and spectro-polarimetric (SP) observations, and both types of observation may be performed simultaneously, yet independently, in response to the macro-commands from the Mission Data Processor (MDP).

SOT provides diffraction limited images ($\sim$0.2″ resolution) of the photosphere and chromosphere. The combined SOT system is optimized for measurement of the vector magnetic field in the photosphere and to study the dynamics of both the photosphere and chromosphere. SOT employs active image stabilization to obtain continuous, seeing-free, diffraction limited observations with enhanced stability. On 2016 February 25, after 9.4 years of operation on-orbit, the FG camera suddenly developed an electrical short circuit and it is now permanently switched off. With the other two cameras unaffected, Hinode and SOT are continuing a full schedule observations, including Hinode Observing Programs (HOPs) with frequent coordination with the IRIS (IHOPs) and other observatories.

2.2 Interface Region Imaging Spectrograph

The Interface Region Imaging Spectrograph (IRIS, De Pontieu *et al.* (2014b)), small explorer spacecraft provides simultaneous spectra and images of the photosphere, chromosphere, transition region, and corona with 0.33″–0.4″ spatial resolution, 2 second temporal resolution, and 1 km/s velocity resolution over a field-of-view of up to 175″×175″. IRIS was launched into a Sun-synchronous orbit on 27 June 2013 using a Pegasus-XL rocket and consists of a 19-cm UV telescope that feeds a slit-based dual-bandpass imaging spectrograph. IRIS obtains spectra in passbands from 1332–1358 Å, 1389–1407 Å and 2783–2834 Å, including bright spectral lines formed in the chromosphere (Mg II h 2803 Å and Mg II k 2796 Å) and transition region (C II 1334/1335 Å and Si IV 1394/1403 Å). Slit-jaw images in four different passbands (C II 1330, Si IV 1400, Mg II k 2796, and Mg II wing 2830 Å) can be taken simultaneously with spectral rasters that sample regions up to 130″×175″ at a variety of spatial samplings (from 0.33″ and up). IRIS is sensitive to emission from plasma at temperatures between 5000 K and 10 MK. The main science goal of IRIS is to understand the flow of mass and energy through an *interface region*, formed by the chromosphere and transition region, between the photosphere and corona.

The IRIS telescope (Figure 2.3) feeds light from three passbands into the spectrograph box:

1. Far Ultraviolet (FUV1): 1331.56–1358.40 Å
2. Far Ultraviolet (FUV2): 1390.00–1406.79 Å
3. Near Ultraviolet (NUV): 2782.56–2833.89 Å

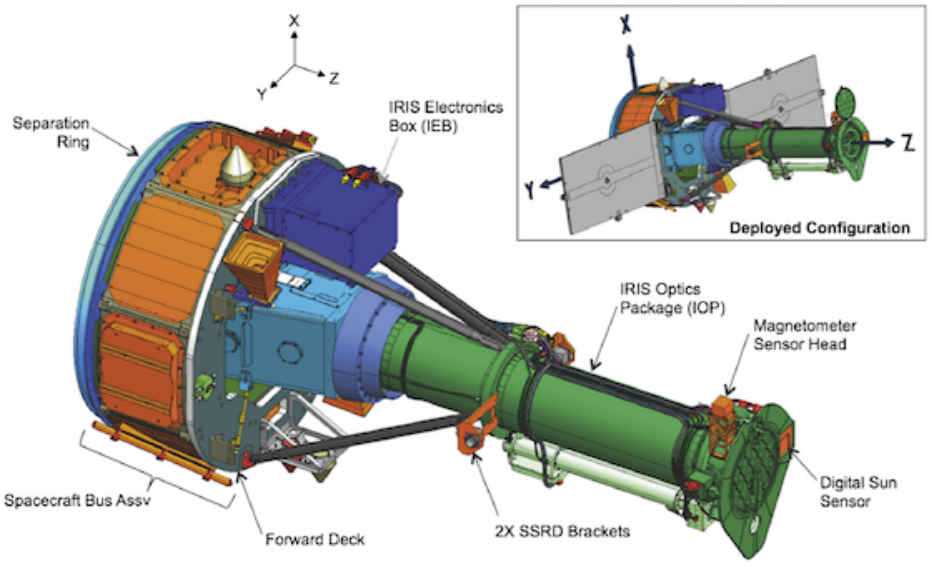

FIGURE 2.3: Schematic view of IRIS showing the 19-cm UV telescope, with and without solar panels (for clariity). Light from the Cassegrain telescope (green) is fed into the spectrograph box (light blue). *Image credit:* LMSAL IRIS mission (http://iris.lmsal.com).

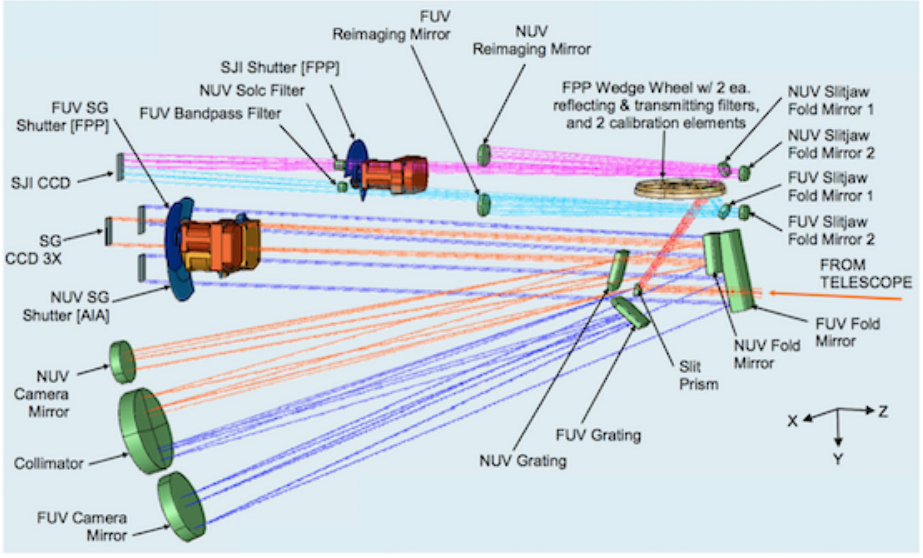

FIGURE 2.4: Schematic diagram of path taken by light in the FUV spectrograph (dark blue), NUV spectrograph (orange), FUV slit-jaw (light blue) and NUV slit-jaw (purple) path. *Image credit:* LMSAL IRIS mission (http://iris.lmsal.com).

In the spectrograph, the light follows several paths (see Figure 2.4), either:

- Spectrograph (SG): passing through a slit that is 0.33″ wide and 175″ long, onto a grating that is sensitive in both FUV and NUV passbands, then onto 3 CCDs to produce spectra in three passbands (FUV1, FUV2, and NUV).
- Slit-Jaw Imager (SJI): reflected off the reflective area around the slit (″slit-jaw″), passing through or reflected off broadband filters on a filterwheel, then onto 1 CCD to produce an image of the scene around the slit (slit-jaw=SJI) in 6 different filters (2 for calibration, 4 for solar images).

The observational capabilities of IRIS include:

- High spatial resolution (0.4″) spectroscopic and (context) imaging data over a field of view of at least 120″, providing diagnostics from the photosphere to the corona, with an emphasis on the chromosphere and transition region.
- A high signal-to-noise ratio for two-second exposures for a few select bright lines covering chromosphere and transition region, which allows a velocity determination with 1km/s accuracy and 3 km/s spectral pixels.
- High-cadence spectral (20 second) and imaging (10 second) observations covering a small region of the Sun (5″×120″) for periods of up to eight hours continuously.
- Eclipse-free observations for up to eight months per year with an average data rate of 0.7 Mbit/s.

These capabilities enable IRIS to observe the thermal evolution of plasma from photospheric to coronal temperatures at the spatio-temporal resolution required

for the highly dynamic interface region. The spectral, temporal, and spatial resolution and spectral coverage and effective areas of IRIS constitute significant advances over previous instrumentation.

2.3 Solar Dynamics Observatory

As the first mission to be put in motion under NASAs Living With a Star (LWS) Program, Solar Dynamics Observatory (SDO, Pesnell *et al.* (2012), Figure 2.5) was launched from Cape Canaveral on 11 February 2010. It was put in a geosynchronous orbit with an inclination of 28°. SDO was initially conceived as a five year mission to study the Sun and its impact on space weather. Its main scientific goal is to study the solar magnetic field leading to predictability of solar activity. To realise this, SDO has three instruments, namely: Atmospheric Imaging Assembly (AIA), Helioseismic and Magnetic Imager (HMI) and Extreme Ultraviolet Variability Experiment (EVE). AIA and HMI data are used in this research and are described below.

2.3.1 Atmospheric Imaging Assembly

With four telescopes, Atmospheric Imaging Assembly (AIA, Lemen *et al.* (2012)) images the Sun in ten different wavelengths (ranging from 4500 Å to 94 Å) nearly simultaneously. The AIA filters are chosen to cover a large thermal range from the photosphere to the corona. The seven EUV band-passes help to monitor the coronal response to changes in the photospheric magnetic field. Using these, for the first time, coronal plasma can be observed at high cadence with near arcsec resolution. The f/20 telescopes have a Cassegrain mount. Each telescope has a back illuminated 4096 4096 CCD detector which provides a $41 \times 41\, arcmin^2$

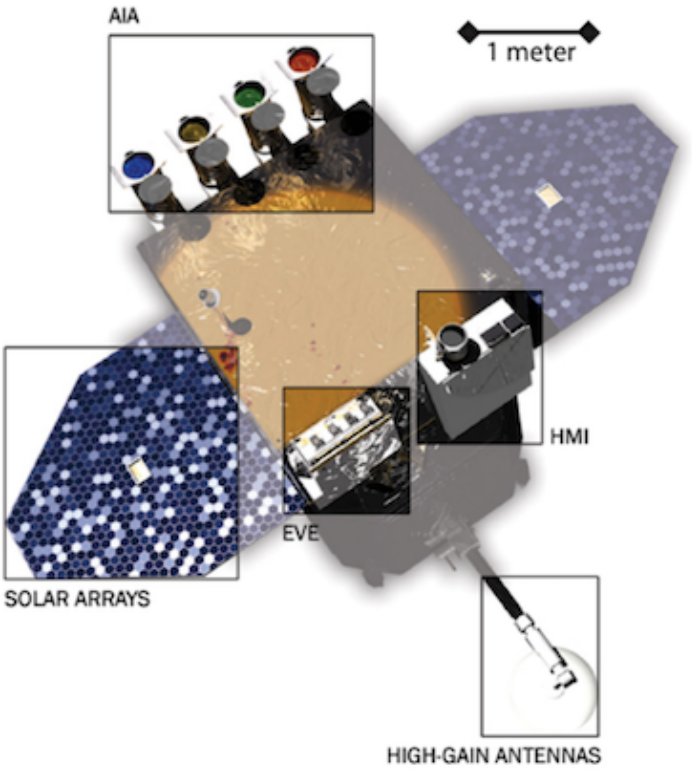

FIGURE 2.5: SDO spacecraft with all the instruments on-board labelled. *Image credit:* NASA SDO mission

FOV. With a resolution of 1.5″, AIA covers the whole solar disk at a cadence of 10 seconds in each wavelength passband.

2.3.2 Helioseismic and Magnetic Imager

Helioseismic and Magnetic Imager (HMI, Schou *et al.* (2012)) is capable of mapping the magnetic and velocity field on the photosphere. The instrument uses the Fe I 6173 Åline to measure Stokes parameters from Zeeman splitting and Doppler-shifts to create full disk longitudinal (LOS), vector magnetograms and Dopplergrams, respectively. LOS magnetograms and Dopplergrams are taken every 45 seconds with 1″ resolution while vector magnetograms have 12 minute cadence. HMI is the first instrument to produce high cadence measurements of strength

and velocity of the surface magnetic field. The fundamental subject is to understand the origin of the solar magnetic fields. To this effect HMI was perceived to help in the understanding of the fluid dynamics within the Sun and their coronal linkage.

Different observations, primarily from IRIS and Hinode, are used in this thesis to study various small-scale features in solar chromosphere and transition region. The techniques employed for data-reduction and analysis are explained during the course of the particular chapters. Table 2.1 mentions specific instruments used to study small-scale features and events in the respective chapters.

TABLE 2.1: Instruments used to study the small-scale features.

Chapter	Primary Instrument	Spatial resolution (arcsec pixel^{-1})	Cadence (s)	Feature of Interest
3	Hinode/SOT	0.109–0.32	300	polar network bright-points
4	IRIS/SJI	0.166	10	transition region network jets
5	IRIS/SG	0.166–0.35	31.6–130	two-component emission lines
6	IRIS (SJI & SG)	0.166	3.3–13	high-frequency oscillations

Chapter 3

Association of calcium network bright points with underneath photospheric magnetic patches[†]

3.1 Introduction

The chromospheric network is a web-like pattern most easily seen as emission feature in the red line of hydrogen (Hα) and the violet lines of calcium (Ca II K and Ca II H) images of Sun. This pattern or network is believed to be coincident with the boundaries of large-scale convective cells, known as the supergranules, each about 20-60 Mm in diameter (Rieutord and Rincon 2010). Simon and Leighton (1964) found a one-to-one correlation in the position of supergranules and bright network seen on Ca II K line spectroheliograms (also see Parker (1978) and Sheeley *et al.* (2011)). The supergranular convective flow across photosphere, pushes the

[†]Results of this work are accepted for publication in the Solar Physics.

magnetic elements towards the supergranules boundaries, so a network of magnetic field is formed. These elements are also buffeted by exploding granules and sometimes get annihilated or grow in size. These magnetic field clumps with several hundreds of Gauss at the photospheric level leads to enhanced heating in the solar atmosphere, with a consequent increased brightening at certain wavelengths in chromospheric and coronal heights.

Frazier (1970) has shown that the downflows at the vertices, where several supergranular cells meet are much more prominent for the concentration of magnetic flux than the rest of cell boundaries. At these points the magnetic field appears comparatively enhanced, resulting in coinciding network bright points recognisable in Ca II lines. These bright points are brighter than rest of the network structure and proposed to be associated with strong ($\sim$1000 G) magnetic fields, probably in the form of magnetic flux tubes emerging from below the photosphere. Figure 3.1 shows an example of Ca II H observation obtained from Solar Optical Telescope (SOT) (Tsuneta *et al.* 2008b) aboard *HINODE* (Kosugi *et al.* 2007) which clearly marks the network bright points, and network and internetwork as distinguished features of solar chromosphere.

The nature of the network and its heating have been modeled by many authors (*e.g.* Gabriel (1976); Schrijver (2001); Wedemeyer-Böhm *et al.* (2009)). For instance, in the model by Gabriel (1976), heating occurs along the field lines by magnetohydrodynamic (MHD) waves. Some oscillations may arise through the buffeting of narrow flux tubes at chromospheric altitudes by solar granulation, which leads to the propagation of MHD waves, causing the heating of chromospheric network and upper atmosphere. The heating is greatest where the field lines are most concentrated, at the common boundaries of many super-granules, in particular, network bright points. A different scenario involving magnetic dipole evolutions have also been proposed by many authors (*e.g.* Harvey and Martin (1973); Harvey (1985); Webb *et al.* (1993)) for explaining the observed enhanced

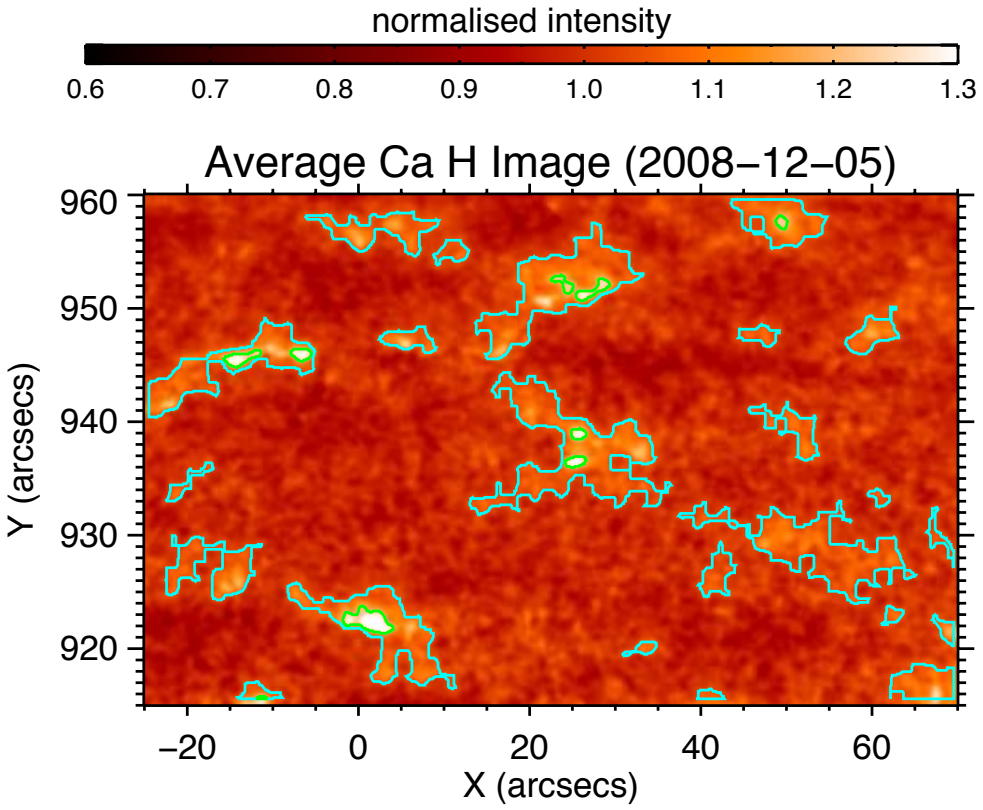

FIGURE 3.1: Representative example of observations from SOT which shows internetwork, network and network bright points. The blue contours mark the locations of the bright network where the surrounding darker areas are called internetwork. The brighter locations present within the bright network are termed as network bright points which are marked by green contours.

brightening in the different layers of the solar atmosphere. In this process, the change in magnetic flux due to cancellation, emergence, fragmentation, and coalescence occurring at the locations of supergranular network junctions leads to the excess chromospheric and coronal brightenings (Egamberdiev 1983; Habbal *et al.* 1990).

Network bright points observed in polar regions of Sun are referred as polar network bright points. They populate higher heliographic latitudes above 60 ° or 70 °. Using high-resolution spectro-polarimetric observations with SOT, it is found that the polar region of Sun has isolated patches of the concentrated magnetic field with strengths exceeding 1 kG of typival life-times of 5–15 hrs (see Tsuneta *et al.* (2008a) and Ito *et al.* (2010) for details). Moreover, Tsuneta *et al.* (2008a) and

Kaithakkal *et al.* (2013) have reported that the kilogauss patches coincide in position with polar faculae at the photosphere. We expect the spatial intermittency of the magnetic field to persist even at the chromospheric level, *i.e.* with polar network bright points. In this work, we investigate the association between the network bright points and magnetic patches using automated techniques. For this purpose, we have used SOT observations specifically devoted to observe polar regions of the Sun. In particular, we have used Ca II H passband images along with co-spatial and co-temporal level 2 spectro-polarimetric data observed by SOT. We have analyzed different datasets in polar regions of the Sun, details of which are given in section 3.2. Results are discussed in section 3.3 and conclusions drawn from the study are summarized in section 3.4.

3.2 Observations and Data Analysis

3.2.1 Details of Observations

We have analyzed six polar datasets in this study (see Table 3.1). To study low chromospheric features, the Ca II H bandpass of Broad-Band Filter Imager (BFI) of SOT, centered at 396.85 nm with a band-width of 0.3 nm is used. The SOT Ca II H data is calibrated by using the IDL routine of fg_prep.pro available through SOT library of *solarsoft*. For magnetic field estimation, we have used co-spatial and co-temporal level 2 data obtained by spectro-polarimeter(SP) of SOT. The SP creates high-precision Stokes polarimetric line profiles of the Fe I 6301.5 nm and 630.25 nm spectral lines. The primary product (Level 1) of the SP is Stokes IQUV spectra suitable for the derivation of vector magnetogram maps of the solar photosphere. The Level 2 data of the SP (provided at http://sot.lmsal.com/data/sot/level2d/) contains the results of full Milne-Eddington

inversion of the Level 1 data in form of 36 SP components which include inversion parameters and ancillary quantities. For every Ca II H data-set mentioned in Table 3.1, there exists a corresponding SP Level 2 data containing one set of 36 SP components. From the Level 2 data of SP, we mostly use maps of magnetic field strength as our interest mainly lies in studying the relationship between the chromospheric Ca II H intensity and the strength of magnetic field present at the corresponding locations in the photosphere. Considering that the typical lifetime of supergranular cells is approximately a day and we are interested in the long-term enhanced heating of chromosphere, we performed all the analysis over time-averaged Ca H images. Hence, we obtain a single average Ca H intensity map for each dataset mentioned in Table 3.1. The pixel sampling of the Ca II H images is $0.11''$ whereas that of the maps magnetic field strength is $0.32''$ hence the pixel resolution of the Ca II H images was degraded to $0.32''$ (spatial resolution of $\sim 0.65''$) in order to maintain the consistency between Ca II H intensity and magnetic filed strength maps throughout the study. It is important to note that the degradation of resolution appear to introduce smearing in the Ca H images.

TABLE 3.1: Details of Ca H observations from SOT.

Data-Set	**Observation Time**	**FOV**	**Pointing (Xc,Yc)**	**Target**
a	2007-11-08 13:04 to 13:58 UT	$60'' \times 40''$	$100'', 935''$	North Pole
b	2008-12-04 18:16 to 18:59 UT	$40'' \times 55''$	$45'', -933''$	South Pole
c	2008-12-05 10:01 to 10:59 UT	$95'' \times 45''$	$23'', 938''$	North Pole
d	2009-04-01 12:00 to 12:59 UT	$75'' \times 70''$	$-138'', -885''$	South Pole
e	2010-05-14 12:02 to 12:57 UT	$160'' \times 40''$	$20'', -900''$	South Pole
f	2012-03-18 13:00 to 13:59 UT	$150'' \times 50''$	$5'', -905''$	South Pole

3.2.2 Identification of Bright-Point Regions

Pixels with the intensity greater than a given threshold (as discussed below) in Ca II H intensity map are classified as belonging to network bright points. The procedure applied to every average Ca H image for selecting such pixels is as follows (refer Figure 3.1 and 3.2): for every μ, the mean and standard deviatio (σ) of the intensity over the corresponding pixels is calculated. The parameter μ is defined as the cosine of the angle between the surface normal and line of sight to the observer. It varies between 1 at disk center to 0 at the limb (Thompson 2006). For every μ, the pixels with intensity greater than 1.1σ of the respective mean are identified as network regions. Figure 3.2 shows the normalized intensity as a function of μ for the average Ca II H image of the data-set (c). The spikes in the plot are attributed to network bright points, while the smaller fluctuations about 1.0 are ascribed to network structure. The blue curve in Figure 3.2 indicates the threshold for network region selection. Figure 3.1 shows the average Ca H normalized intensity image for the data-set (c) which marks the identified network regions enclosed in the blue contours. From the selected network regions, the pixels with intensity more than 1.1 of average intensity of all the network regions selected in the image are marked as the locations of network bright points. In Figure 3.2 the green line shows such threshold for detection of bright point pixels which is well above the intensity fluctuations due to network and internetwork structures.

The detected bright point pixels are then clubbed into isolated bright point regions (using the IDL function *label_region*) with an area threshold of 50 pixels, *i.e.* the bright point region should have the total number of pixels to be more than 50 in order to be selected. As mentioned earlier the pixel resolution of the images is $\sim 0.32''$. Hence, the area-threshold of 50 pixels which roughly corresponds to $7\,pixels \times 7\,pixels$ area $\sim 2.2'' \times 2.2''$ area. Such detected regions are considered to represent the network bright point regions which are indicated by green contours

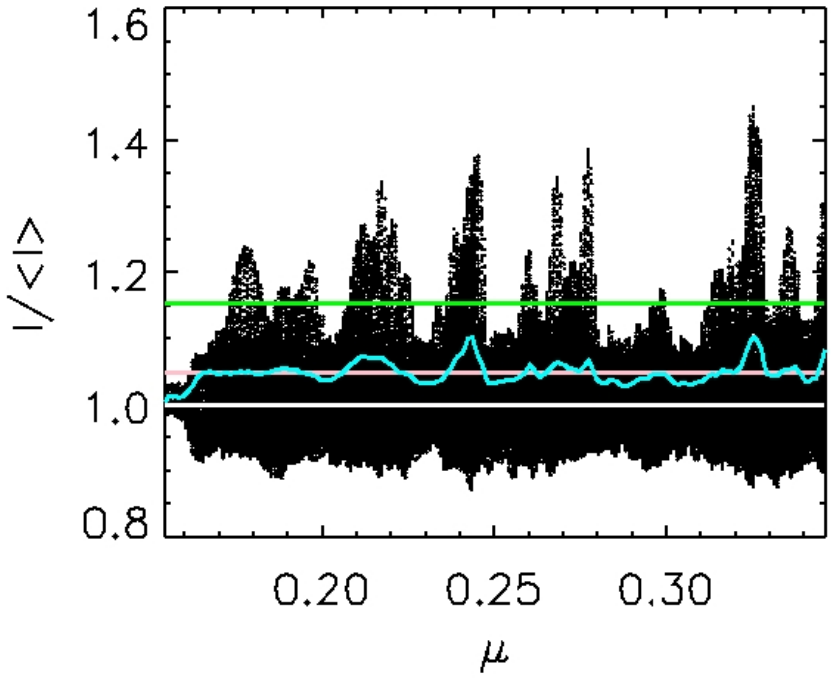

FIGURE 3.2: Normalised Intensity ($I/ < I >$) vs μ for all pixels of average Ca II H image of data-set (c) in Table 3.1. In this plot network bright points appear as intensity spikes. Blue curve indicates the threshold for identifying network regions, pink line marks the average of blue curve and green line indicates the threshold for selection of bright point pixels.

in the Figure 3.1. Every such identified network bright point region is then aligned with the corresponding region in the respective magnetogram. Figure 3.3 showcases various examples of co-aligned network bright points and magnetic patches where the network (blue) contours and the network bright-point (green) contours are plotted over normalized Ca H intensity and magnetic strength maps. Note that our method of identification of calcium network bright points is automated and thus is free from the involvement of human subjectivity. The limitation of our method lies in its inability to identify the bright points very close to the limb as noise becomes dominant because of low data-counts present near the limb.

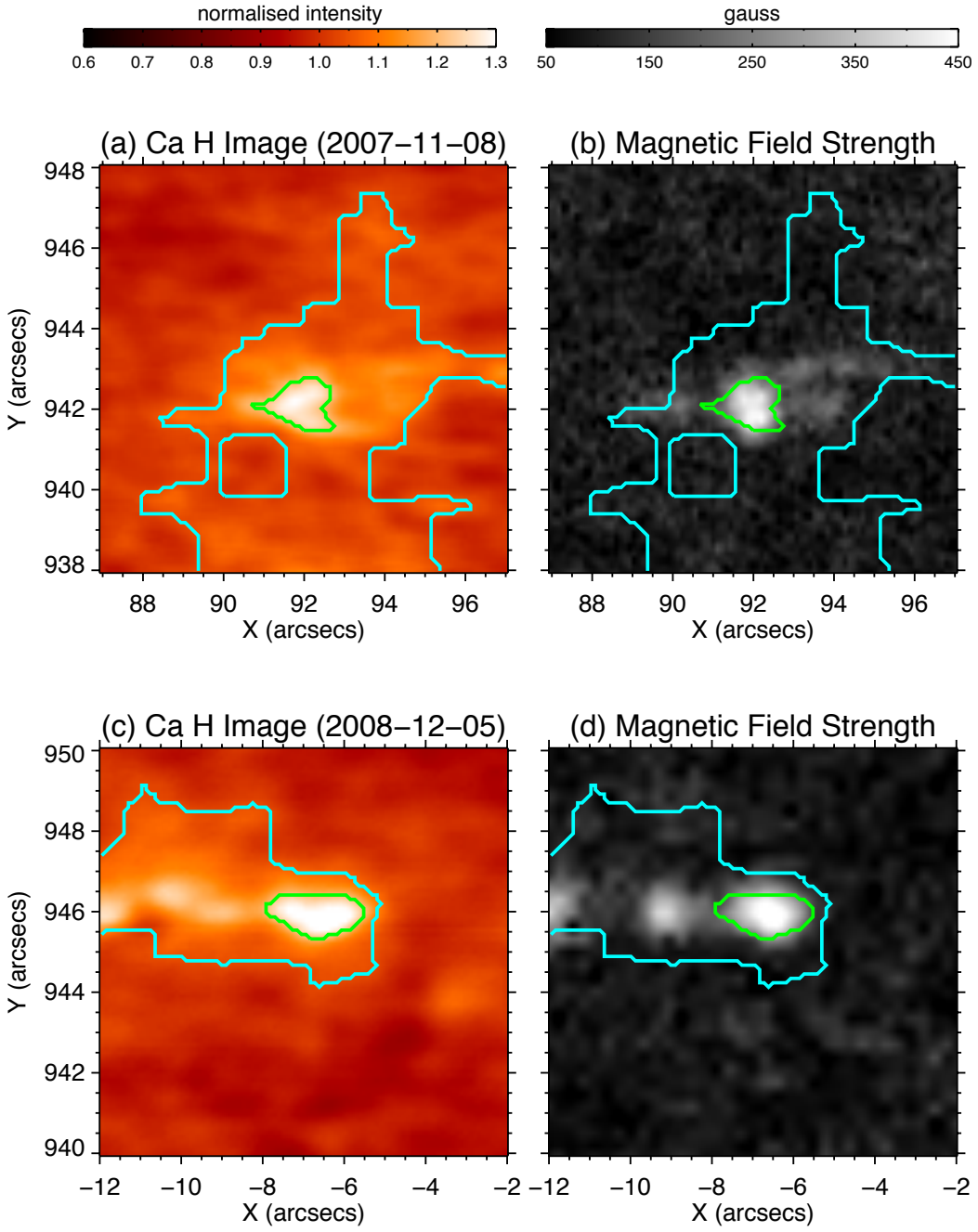

FIGURE 3.3: Representative examples showing association between bright points and magnetic patches: (a) & (b) Normalised SOT Ca H image of a sub-region of data-set (a) & corresponding magnetic field map; (c) & (d) same as (a) and (b) but for data-set (c). The blue contours enclose the network regions and green enclose the network bright-points.

3.3 Results and Discussions

We find that the network bright points, as seen in Ca H images are almost always associated with the magnetic patches as seen in the photosphere (as illustrated in Figure 3.3). Their sizes are $\sim 2'' - 5''$. The lower limit of $2''$ of size of the bright-points is dictated by the minimum area-threshold applied while detecting the bright-points (mentioned in section 3.2.2). As shown in a particular example in Figure 3.4, the Ca H bright-points seem to be co-spatial with the groups of G-band bright-points or faculae. Figure 3.1 & 3.3 clearly show that the percentage area covered by the network bright points (green contours) is considerably small. Table 3.2 shows the percentage area of bright points in each data-set studied, along with average magnetic field strength over the whole field of view and only within bright points. Though the percentage area occupied is low, the magnetic field strength concentrated under the network bright points is generally about 3.5 times that of the average field strength over the full FOV of SOT observations. This implies that the overall behaviour of the polar magnetic field should be governed by the magnetic fields underneath these locations on an average. Figure 3.5 shows that the value of the magnetic field strength can reach up to 600 Gauss within the bright point regions. The maximum field strength within the bright point, which happen to be at the centre of the bright point/magnetic patch, reaches upto 1 kG in many cases, as shown in Table 3.2. Tsuneta *et al.* (2008a) and Kaithakkal *et al.* (2013) have also reported the values of the order of a few kG in concentrated magnetic patches. More recently, Pastor Yabar *et al.* (2018) have also observed the presence of strong magnetic field elements of strength 600-800 Gauss in poles. In the past era, the low-resolution observations were unable to detect these small-scale locations of strong magnetic field strengths which is now possible with enhanced resolution data.

Along with considerable spatial association observed between network bright points and magnetic patches, we find that a good correlation exists between bright point

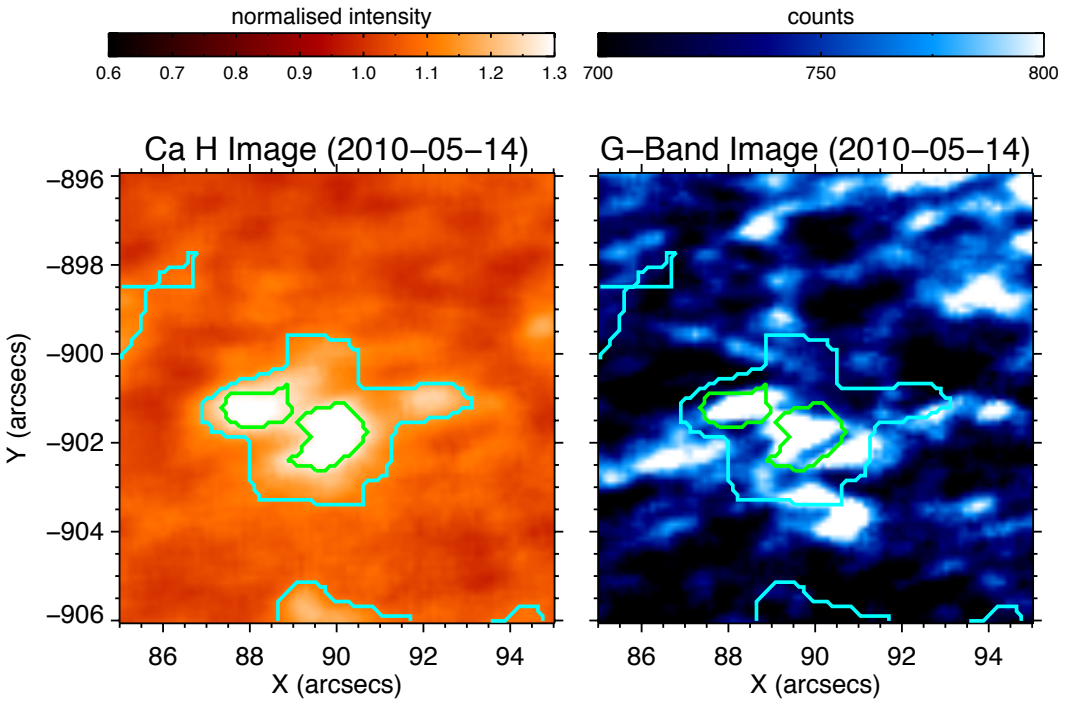

FIGURE 3.4: Ca H and G-band image of a sub-region of data-set (e), showing relationship between the Ca H bright-points with photospheric faculae. The green contours are representing the network bright points which happen to generally lie over the groups of G-band bright points.

intensity and magnetic field strength. Figure 3.5 shows the scatter plot of the normalised Ca H intenisty ($I / < I >$) and magnetic field strength ($| B |$) for all the bright points detected in the 6 data-sets. Note the high value of correlation coefficient (cc) of 0.93. We have attempted to calibrate the normalized Ca H intensity with the corresponding magnetic field strength of the bright points. In Figure 3.5, the straight solid line shows the best fit (based on the chi-square minimization) and corresponding slope and intercept is indicated by m and c along with the respective fitting errors in the estimates. For a network bright point with the value of $I / < I >$ that is greater than 1.14, the value of $| B |$ can be calculated by using this value of the slope (m=*2850* Gauss) and the intercept (c=*–3255* Gauss). For $I / < I >$ less than 1.14, the deduced relation will yield a negative value of $| B |$ which is unphysical. Considering the errors in the slope and intercept, the percentage error in the deduced magnetic field strength from this linear relation

turns out be 10%.

TABLE 3.2: Properties of network bright points.

Data-set	**% area covered by bright points**	**avg. | B | over full FOV**	**avg. | B | over all bright points**	**max. | B | within the bright points**
a	0.2	93 Gauss	320 Gauss	695 Gauss
b	0.2	92 Gauss	267 Gauss	634 Gauss
c	0.5	89 Gauss	292 Gauss	983 Gauss
d	0.6	94 Gauss	392 Gauss	934 Gauss
e	0.8	107 Gauss	500 Gauss	1210 Gauss
f	0.5	122 Gauss	322 Gauss	686 Gauss

It is worthwhile to mention that the magneto-hydrodynamic (MHD) models by Schrijver *et al.* (1989b); Solanki *et al.* (1991) and Schrijver (1993) have predicted the presence of power-law dependence of calcium intensity over the magnetic field strength as shown in equation 3.1 below:

$$I = I_0 + M|B|^a \tag{3.1}$$

where I denotes the observed calcium intensity, I_0 represents the *zero or basal* intensity, $|B|$ denotes magnetic field strength, M is a constant multiplier and a to be the power-law index. For instance, the flux tube model of Schrijver (1993) have proposed the value of the power-law index (a) to be ~ 0.4. Whereas, different observations (Schrijver *et al.* 1989a; Harvey and White 1999; Rezaei *et al.* 2007; Loukitcheva *et al.* 2009) have obtained different values of a to be ranging from 0.2 to 0.7. On the other hand, Skumanich *et al.* (1975) and Nindos and Zirin (1998) have observed the linear relation (*i.e. a= 1.0*), which yields similar result as obtained in the present study.

The linear relation between Ca II H intensity and magnetic field strength indicates that the network bright-points can be considered as individual flux-tubes (Schrijver *et al.* 1989a), well isolated from each other. The atmospheric heating over such flux-tubes is independent of the ambient magnetic topology and hence results in the linear relation between Ca II H (or K) intensity and field strength. In addition, as pointed out by Skumanich *et al.* (1975), the non-linear effects appear with the inclusion of weak field (< 50 gauss) and very strong field (> 1 kilogauss) locations. The linear trend obtained here could be an effect of selection of the features of interest. Hence, it is important to note that the linear relation obtained here is valid generally for the network bright points *i.e.* for the compact brighter locations ($\sim 2'' - 5''$) inside the bright network regions with the values of normalised calcium intensity to be more than 1.20 and thus magnetic field strengths to be greater than 200 Gauss (as depicted in Figure 3.5). Below this regime, which could map different class of features and structures, this linear relation may or may not hold good, *i.e.* the power-law index (a) in equation (1) could be different than 1.0 with completely different values of other constants. Moreover, for the active region plages, which posses similar magnetic field strengths, intensity values and sizes but are embedded in a completely different magnetic environment as compared to network bright points, the relation between calcium intensity and magnetic field strength could be different (see Harvey and White (1999) for details).

3.4 Conclusions

Recently, Tsuneta *et al.* (2008a) and Kaithakkal *et al.* (2013) have shown that the magnetic patches of strengths $\sim$1 kG coincide in position with polar faculae. In the present work, we have studied 6 polar region observations from SOT and established that such an association between enhanced brightness and magnetic field strength persists up to chomosphere in the polar regions of the Sun. We find that

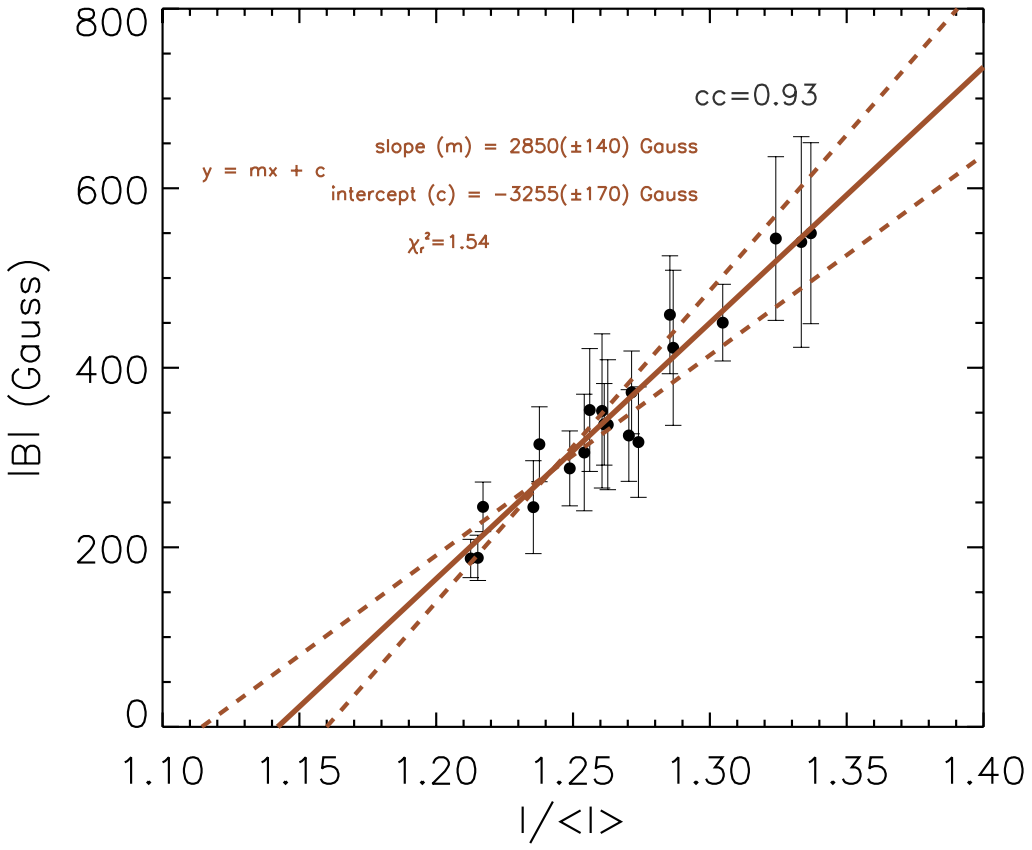

FIGURE 3.5: Scatter plot between normalised Ca H intensity ($I / < I >$) and magnetic field strength ($| B |$) for all the 20 bright points detected in the 6 data-sets. Every point in the plot represents the respective values averaged within each bright point region. cc indicates the correlation coefficient, m indicates the slope and c indicates the intercept.

the calcium network bright points mostly exists at the locations of concentrated magnetic field. We have observed a considerable spatial association between the network bright points and magnetic patches in all the data-sets. Moreover, a good correlation exists between normalized Ca H intensity and photospheric magnetic field strength of the network points and a linear relation is present between them. Though the percentage area covered by the network bright points is considerably small, they posses high magnetic field values and thus contribute to the global polar field majorly. These chromospheric Ca H bright points seems to be co-spatial with groups of G-band bright points in the photosphere. This clearly indicates that these different features are directly coupled with each other, though present

in different layers of the solar atmosphere, and happen to be manifestations of the magnetic field concentrations present in the lower photosphere.

Chapter 4

Statistical study of network jets observed in the solar transition region: A comparison between coronal holes and quiet sun regions[†]

4.1 Introduction

The solar chromosphere and transition region (TR) act as an interface between the relatively cool photosphere ($\sim 6 \times 10^3$ Kelvin) and hot corona ($\sim 10^6$ Kelvin), and hence play a key role in the formation and acceleration of solar wind. Numerous

[†]Results of this work are published in Narang *et al.* (2016).

All the animations that are referred to in this chapter are available at `https://doi.org/10.1007/s11207-016-0886-1`

investigations are being carried out to understand where the solar wind originates and how it is accelerated (for recent reviews see Cranmer (2009) and Hansteen and Velli (2012)). Dark regions in coronal images indicate coronal holes (CHs), which are the commonly accepted large-scale source regions of high-speed solar wind. On the other hand, the quiet sun (QS) regions (QS is a generic term for regions too bright to be coronal holes, but too dim to be regarded as magnetically 'active') are considered to be one possible large-scale source of the low-speed component of solar wind (Habbal *et al.* 2001; He *et al.* 2007; Tian *et al.* 2011c). However, identification of precise origin sites of the two different components of solar wind in the respective regions is still a challenging task as it requires high-resolution observations of the chromosphere and TR.

CHs are regions of low density plasma in the solar corona that have magnetic fields opening freely into interplanetary space. The existence of coronal holes was first recognized in the late 1950's, when M. Waldemeier (Waldmeier 1956) noticed long-lived regions of negligible intensity in images made with a visible light coronagraph. In coronal images, CHs appear dark in comparison to QS because they emit less in Ultraviolet and X-ray and are maintained at a lower temperature than the surrounding QS region. The different magnetic structures of CH and QS at coronal heights are responsible for their different appearance in coronal lines (Wiegelmann and Solanki 2004; Tian *et al.* 2008a). CHs are dominated by open magnetic field lines expanding super-radially in the heliosphere whereas, QS regions are dominated by closed magnetic loops of different sizes.

Although CHs emit significantly less at coronal temperatures than QS regions, one can hardly distinguish between the two in most of the chromospheric and lower TR lines. Typically, lines from ions formed around 10^4 Kelvin sample the chromosphere, which is characterized by a cell-like pattern of 'super-granular' surface flows. The super-granular network is the same in CHs and QS. As the temperature increases past 10^5 Kelvin in the thin and chaotic TR, CHs become distinguishable

as areas of lower density and temperature. Also in spectroscopic observations, line parameters in the two regions differ only for TR and coronal lines. For instance, Wang *et al.* (2013) used spectroscopic observations of the Solar Ultraviolet Measurements of Emitted Radiation instrument (SUMER, Wilhelm *et al.* (1995)) onboard the Solar and Heliospheric Observatory (SOHO) spacecraft to investigate the doppler shifts and non-thermal line widths of various lines spanning the solar atmosphere from the chromosphere to the TR. It was observed that most of the TR region lines in network regions are broader and more blue-shifted in CH than in QS. On the other hand, no such distinction between CH and QS was observed for the chromospheric lines. Such differences were found to be less prominent for inter-network regions.

High-resolution observations from the Interface Region Imaging Spectrograph (IRIS) (De Pontieu *et al.* 2014b) have revealed unprecedented levels of details in the less studied solar TR, the layer between chromosphere and corona. In a recent work by Tian *et al.* (2014), detection of prevalent small-scale, high-speed jets with TR temperatures from the network structures of CHs is reported. These network jets can be significantly observed in slit-jaw images (SJIs) of Mg II 2796 Å (10^4 Kelvin, chromosphere), C II 1330 Å (3×10^4 Kelvin, lower TR) and Si IV 1440 Å (8×10^4 Kelvin, TR) passbands of IRIS, though best visible in C II 1330 Å. They can also be identified in the clean spectra of Si IV lines and the most obvious signature of the network jets is the significant broadening of the line profiles. They originate from small-scale bright regions, often preceded by foot-point brightenings. Tian *et al.* (2014) concluded that the existence of network jets are consistent with the 'Magnetic Furnace Model' of solar wind (Axford and McKenzie 1992; Tu *et al.* 2005; Yang *et al.* 2013) and thus may serve as strong candidates for supply of mass and energy to the solar wind and corona. Tian *et al.* (2014) also suggest that some of these network jets may be the on-disk counterparts and TR manifestations of the chromospheric type-II spicules (see also Pereira *et al.* (2014); De Pontieu *et al.* (2014a); Rouppe van der Voort *et al.* (2015); Skogsrud *et al.* (2015)).

The network jets in CHs, as reported in Tian *et al.* (2014), have widths of $\leqslant$300 km with lifetimes of 20-80 seconds and lengths of 4-10 Mm. They calculated apparent speeds of the jets, which turned out be 80-250 km s^{-1} in CHs. We observe that the network jets appear not only in CHs but also in QS areas. In this work, we undertake a comparative study of various properties of these short-lived, small-scale network jets in CH and QS using IRIS SJIs in the 1330 Å passband.

TABLE 4.1: Details of sit-and-stare observations used in this study. For all the data-sets mentioned here, field of view is $119'' \times 119''$, exposure time is 4 seconds and cadence is 10 seconds.

Data-Set	Observation Time	Target	Pointing (X,Y)
A	2014-01-23	CH	$812'', 464''$
	08:48 to 09:39 UT		
B	2014-01-24	CH	$485'', 670''$
	09:11 to 10:06 UT		
C	2014-01-29	QS	$801'', 447''$
	01:23 to 02:21 UT		
D	2014-02-12	QS	$-781'', 582''$
	10:04 to 10:46 UT		

4.2 Observations and Data Analysis

4.2.1 Details of Observations

Four data-sets obtained with IRIS are used in this study: two of which are of CH and two of QS. Details of the observations are showcased in Table 4.1. Note that all four data-sets are high cadence sit-and-stare observations, which is essential to study the dynamics of the short-lived jets. In Figure 4.1, the observed regions on the solar disk are shown as rectangles outlined in the coronal images taken in

the 193 Å pass-band of the Atmospheric Imaging Assembly (AIA) (Lemen *et al.* 2012) on-board the Solar Dynamics Observatory (SDO). The calibrated level 2 data of IRIS is used in our study. Dark current subtraction, flat field correction and geometrical correction have all been taken into account in level 2 data (De Pontieu *et al.* 2014b). Tian *et al.* (2014) mentioned that the network jets are best visible in 1330 Å images. Hence, in this study we use SJIs in this passband only (see Figure 4.2).

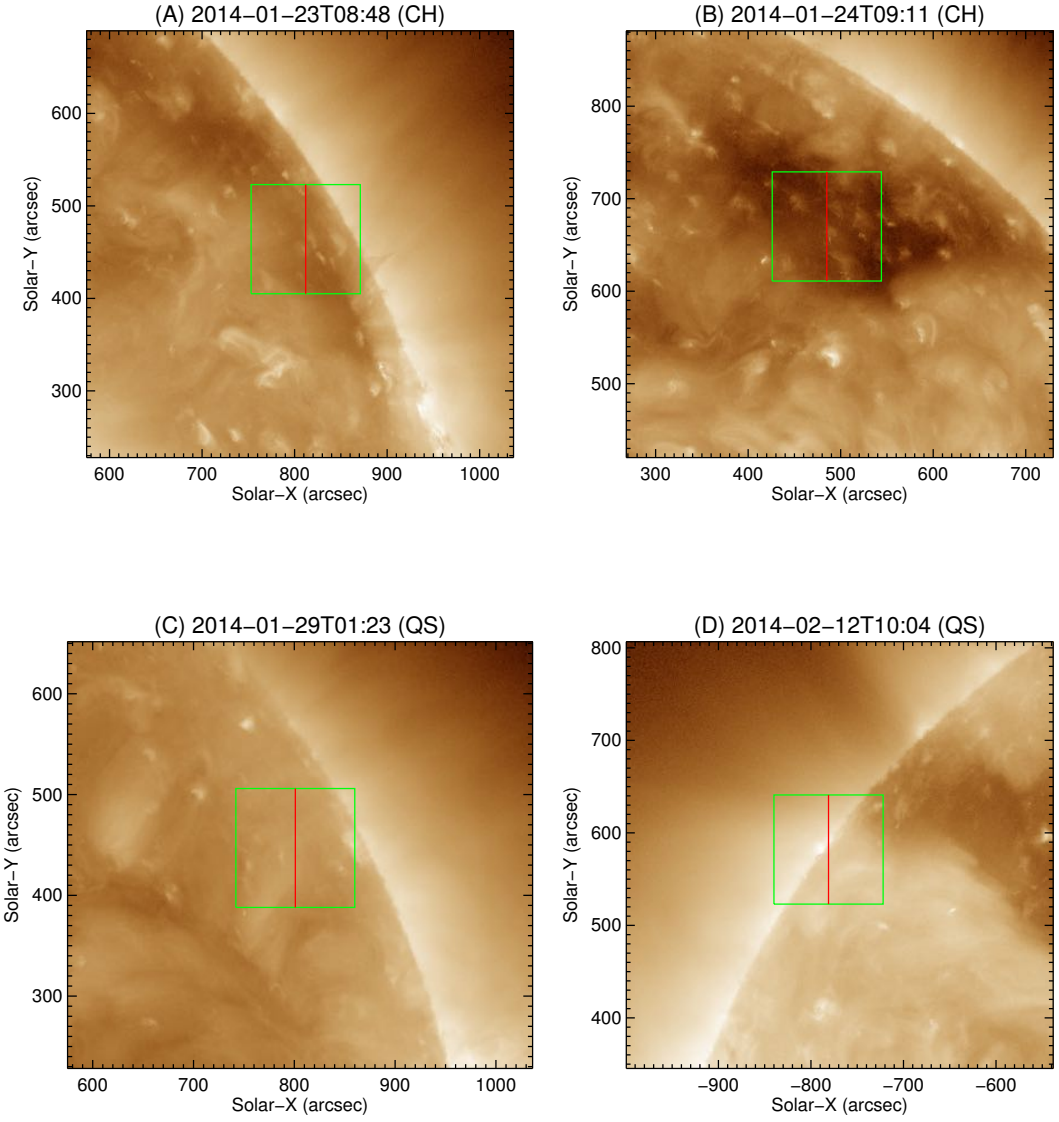

FIGURE 4.1: IRIS observation regions outlined in AIA 193 Å images. In each panel, the green rectangle outlines the FOV of the IRIS SJIs and the red line shows position of the slit. The details of the four observations shown here are provided in Table 4.1.

The 1330 Å passband of IRIS samples emission from the strong C II 1334/1335 Å lines formed in the lower TR ($\sim 3\times10^4$ Kelvin). Though, being a broad passband, it also includes UV continuum emission formed in the upper photosphere. For instance, the observed ubiquitous grain-like structures in SJIs are probably the UV emission from granules (magneto-convective cells on the solar photosphere) and acoustic or magneto-acoustic shocks (Carlsson and Stein (1997); Rutten *et al.* (1999); Martínez-Sykora *et al.* (2015), also refer to the supplementary materials of Tian *et al.* (2014) for a detailed discussion). We have explained in section 4.2.3 that it is important to choose close-to-limb observations to minimize projection effects. There are not many close-to-limb observation with a large field of view and high cadence in 1330 Å passband available. Moreover, the sensitivity of the IRIS Far-Ultravoilet SJI detector has been found to decrease significantly in the past four years. Hence the observations used, taken in January and February 2014, are the best for the comparative study of the very narrow network jets.

4.2.2 Unsharp Masking

As mentioned earlier, due to the presence of quickly evolving grain-like structures and background network emission, the visibility of the network jets is obstructed by a considerable amount. In addition, the jets mostly appear very close to each other in space. They are also observed to recur at the same locations very often in the whole image sequences. Thus, generally it is a bit difficult to isolate individual jets in SJIs. To make the jet structures appear sharper in the images, we have applied the unsharp-masking technique to the SJIs. The technique is explained as follows: For every image in the sequence, a $1'' \times 1''$ (6×6 pixels) boxcar smoothed version of that image is subtracted from the original image. This residual is then added back to the original image. The resultant image is referred to as unsharp masked image. This technique is also applied by Tian *et al.* (2014) to enhance the fine features. Figure 4.2 shows snapshots of the unsharp masked

images in the four observations. Note that, due to the similar spatial and time scales, the bright grain-like features are still present in the unsharp masked images.

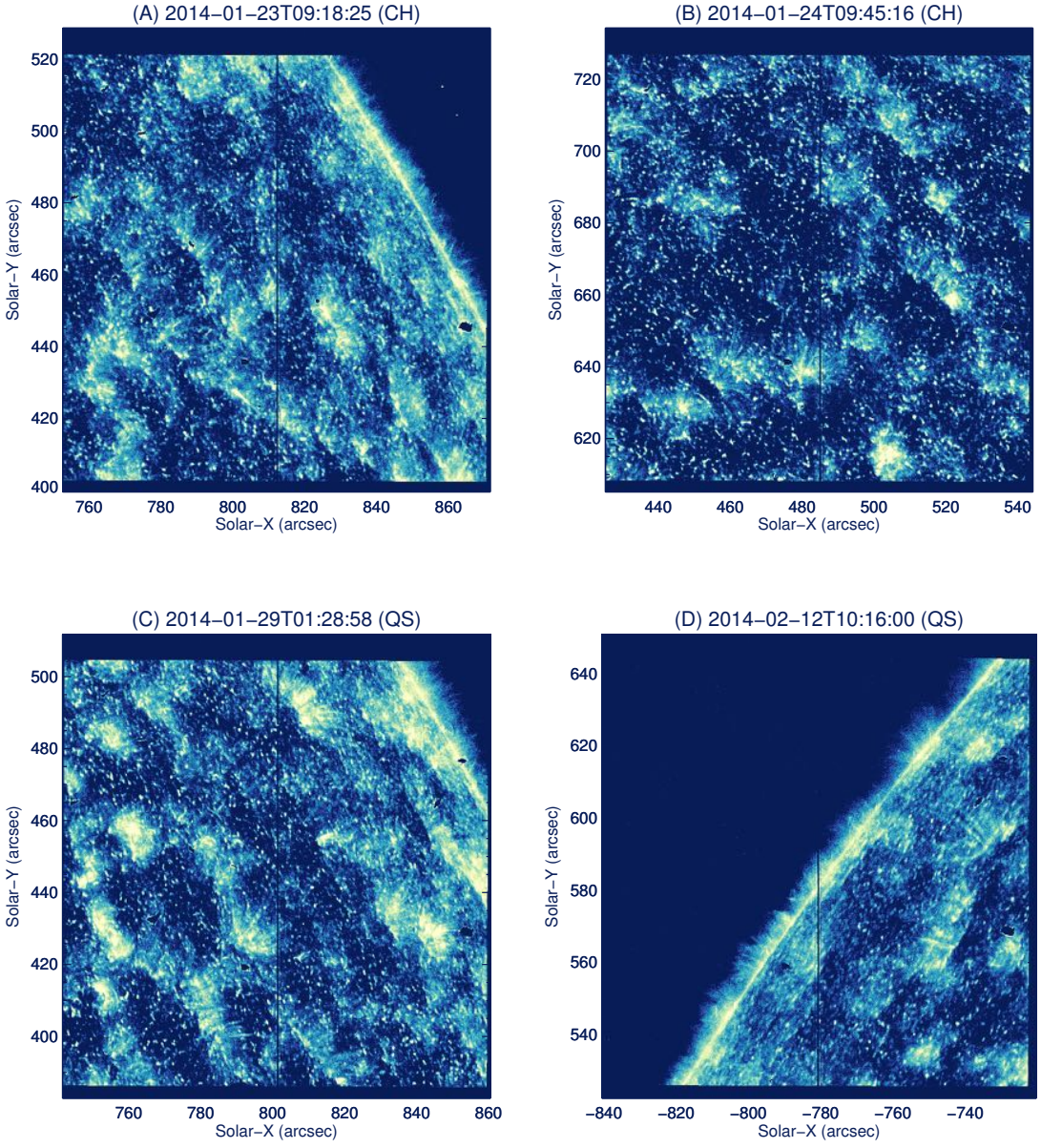

FIGURE 4.2: One of the unsharp-masked SJIs in the image sequence of each data-set used (refer to Table 4.1 and Figure 4.1). Movie of full FOV of the whole image sequence of the original and processed images of data-set (A) can be accessed at `https://doi.org/10.1007/s11207-016-0886-1`. Also see supplementary material of Narang *et al.* (2016) (`https://doi.org/10.1007/s11207-016-0886-1`) for the small FOV movies (zoomed) of the data-sets (B) and (C) showing the dynamics of the jets more clearly.

4.2.3 Space-time Plots

The technique of space-time (S-T) plots is widely used to derive the apparent speeds of moving features. The observed regions are large in size and hence we can identify many network jets in each of the observations shown in Figure 4.2. It should be noted that all four observed regions are close to the limb and thus the line of sight component of the jet velocities should be small. Hence, the value of apparent speeds derived from S-T plots must be close to the real velocities of the jets.

We have visually identified 31 jets in data-set (A), 36 in (B) (making a total of 67 jets in CHs) and 52 jets in data-set (C) and 8 in (D) (making a total of 60 jets in QS regions); with relatively strong emission in the 1330 Å image sequences. The selection of jets is made in such a way that every such jet is well isolated from others in space and time. A lot of care has been taken so that the selected jets are less affected by the bright grain-like structures and thus show clear signatures in the S-T plots. It is important to emphasise here that we are able to measure only the relatively strong jets which is only small fraction (roughly ∼20-30%) of the network jets present in the data. Also note that the data-set D has only 8 jets that can be reliably traced because the duration of this data-set is less (see Table 4.1) and, most important, there is so much off-limb in the field of view in comparison to other data-sets (see Figure 4.2 (D)).

For each jet identified, we first draw a line (curved or straight) along the direction of propagation of the jet (see example in Figure 4.3 (A) and (C)). The intensity along this line is plotted and then stacked with time (Figure 4.3 (B) and (D)). The lifetime and maximum length of the jet can be obtained directly from the S-T map.The measurements done here are solely based on visual inspection. Due to weak emission of the jets and complications by the network grains, it is very difficult to use any automatic method. The minimum lifetime observed is 20 seconds,

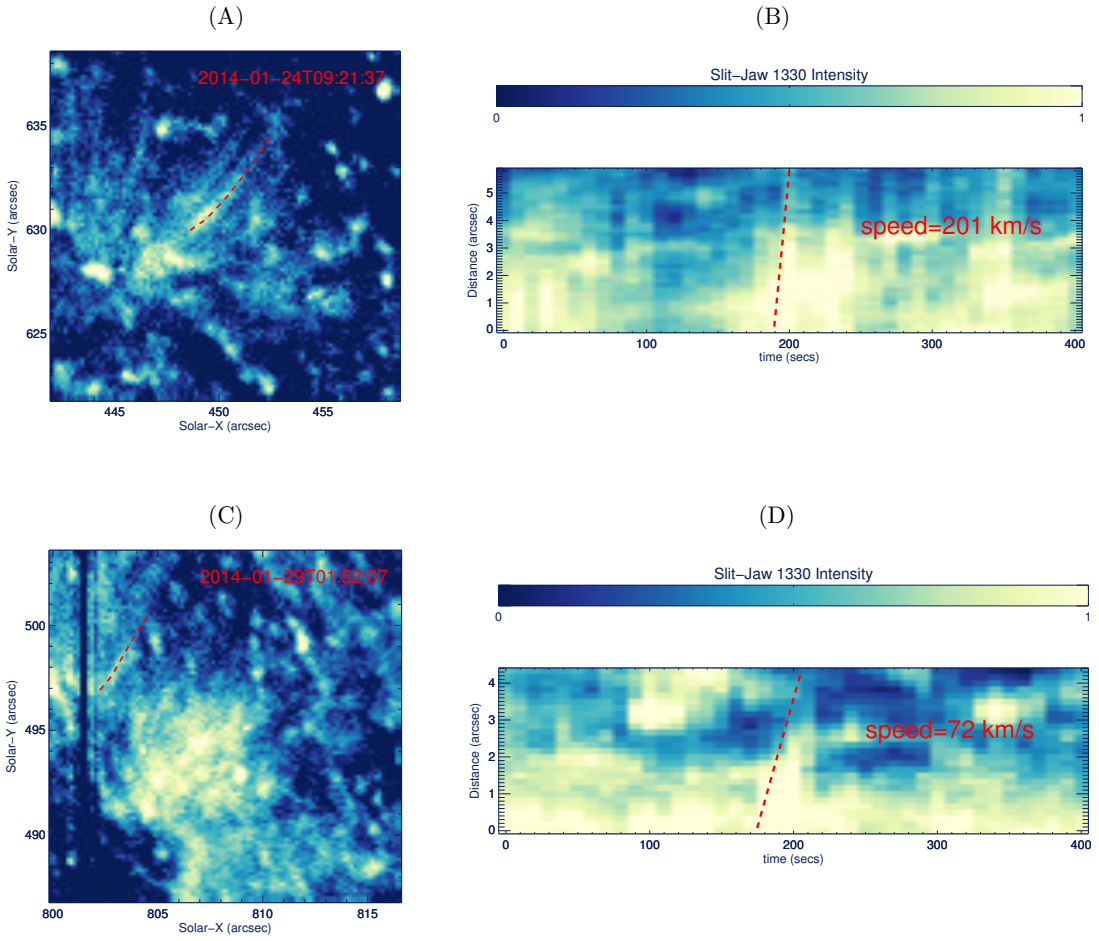

FIGURE 4.3: (A) A small FOV of one of the unsharp-masked images of dataset-B (refer to Figure 4.2). The dashed line indicates the path of a jet. (B) S-T map for the jet marked in (A). (C) Same as (A) but for dataset-C. (D) S-T map for the jet marked in (C).

although it may be possible that many jets have lifetimes shorter than 20 seconds as the observations are limited by a cadence of 10 seconds. The apparent speed can be calculated as the slope of the inclined strip in the S-T plot. For example, the apparent speed of the jet marked in Figure 4.3 (A) and (B) is calculated to be 201 km/s and that in Figure 4.3 (C) and (D) is calculated to be 72 km/s. Total of four data-sets are analyzed in the present work, independently by myself and the second author on the paper published in Solar Physics (Narang *et al.* 2016). Results obtained by them are generally consistent. It is important to note that the uncertainty in the measurement of speed is dictated by the spatial resolution and time cadence of the data. The spatial resolution of IRIS SJIs is ∼250 km and

cadence of all the data-sets used is 10 seconds, hence the minimum uncertainty in the calculation of speeds of the jets turns out to be ∼25 km/s.

4.2.4 Foot-point Brightness

It is already mentioned that the network jets are mostly preceded by foot-point brightenings. The increase in brightness near the foot-points of the jets is generally observed before the appearance of the jets and/or during the initial phases of the life-time of the jets. The typical life-time of such brightening is generally comparable to the life-time of the jet. As it is important to explore the impact of local heating on the dynamical properties of the jets, we calculated the increase in foot-point brightness for every jet. The foot-point of jet is defined as the location of origin of the jet. We choose a 2×2 pixel area around the foot-point of the jet. The intensity within this area is determined at the instant, closest to appearance of the jet, when the brightness at the foot-point is maximum, say *brightness*. The intensity at the same location is determined in two more frames in the image sequence, one before and one after the frame of maximum intensity at the foot-point. These two frames are selected such that there is no enhanced brightening at the location of the foot-point of the jet as compared to surrounding area. The average of the intensities at the location of the foot-point of these two frames is calculated, say *average*. This *average* is subtracted from the *brightness* (as termed above). The resultant is divided by the *average* and multiplied by 100 to get result in terms of a percentage. Note that by term intensity used above throughout, we mean the total data-counts in the 2×2 pixel area obtained from original SJIs.

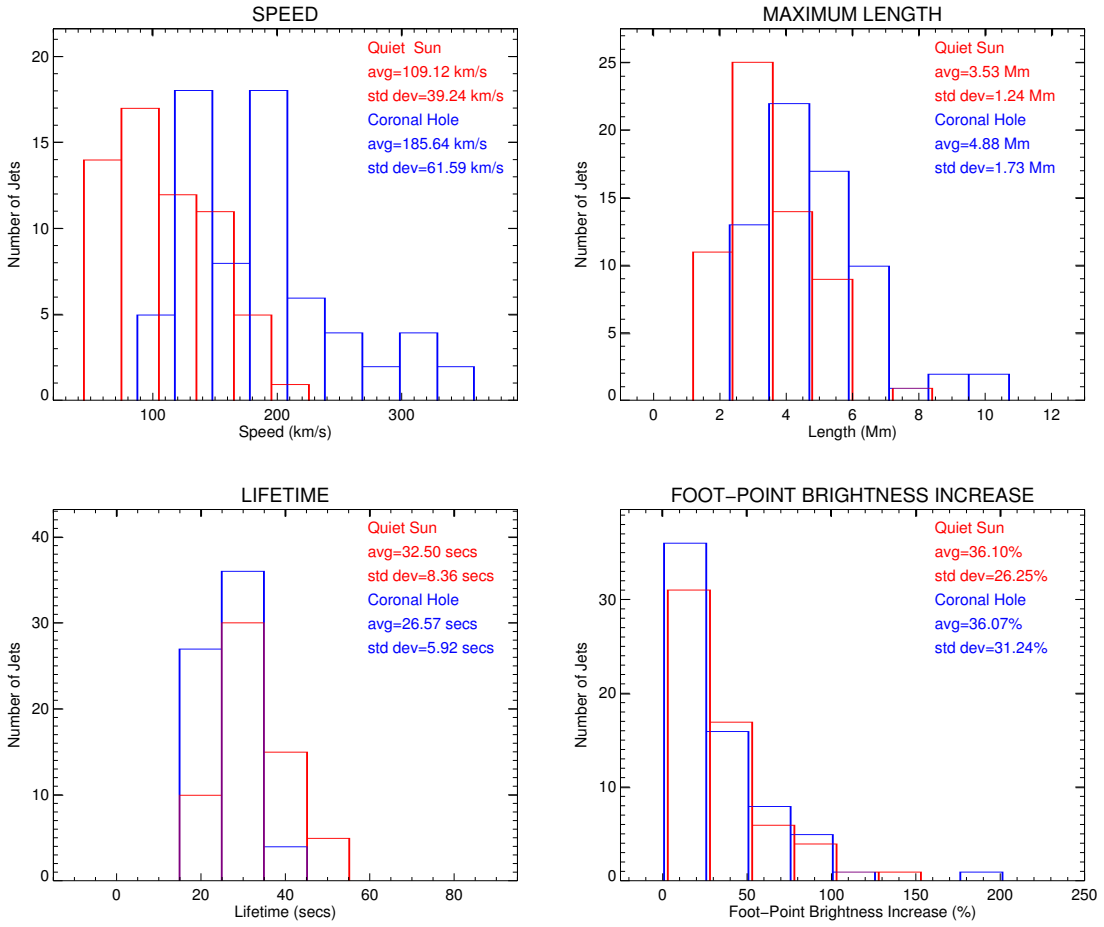

FIGURE 4.4: Distribution of different parameters of network jets showing comparison between CH and QS regions. The total sample number for CH distributions (indicated by blue colour) is 67 jets and that for QS distributions (indicated by red colour) is 60 jets.

4.3 Results and Discussions

We have analyzed different properties of the network jets (mainly apparent speed, length, lifetime and increase in foot-point brightness) to study their dynamics and for comparison between CH and QS jets. The comparison clearly shows that the average values of apparent speed and length of jets in CHs are significantly greater than those in QS regions as showcased in Figure 4.4. The QS results are marked in red and CH results are represented by blue histograms. Though, there does not exist any such demarcation for cases of lifetime and foot-point brightness

increase. The comparison of calculated average values (with standard deviation) of the above mentioned properties is summarized in Table 4.2.

TABLE 4.2: Average properties of network jets. The errors mentioned are standard deviations of the respective distribution.

	Coronal Hole	**Quiet Sun**
Speed (km s^{-1})	186 ± 62	109 ± 39
Length (Mm)	4.9 ± 1.7	3.5 ± 1.2
Lifetime (secs)	27 ± 6	33 ± 8
F-P Brightness Increase (%)	36 ± 31	36 ± 26

As CH jets appear to be faster and longer than QS jets, this may be a consequence of different magnetic configurations in the CH and QS areas. In CHs, open and expanding magnetic flux tubes at network boundaries must be assisting the small-scale network jets to propagate up to larger extents with higher speeds and, hence the jets are accelerated more efficiently in CHs than in QS regions. This result is consistent with a recent numerical simulations on chromospheric jets by Iijima and Yokoyama (2015). They have pointed out that these jets are projected farther outward with higher speeds when overlying coronal gas pressure is lower (similar to that in coronal hole) and shorter when the coronal gas pressure is higher (similar to that in quiet sun) which agrees with our observations. We should point out that in their simulation jets are generated by chromospheric shocks and the amplification of chromospheric shock wave will be different in CH and QS.

Our observed greater apparent speeds of these jets in CHs as compared to the QS also allows to explore the suggestions made by Tian *et al.* (2014) and Rouppe van der Voort *et al.* (2015) that some network jets are likely to be TR manifestations of rapid blueward excursions (RBEs). It has already been claimed (*e.g.* Rouppe van der Voort *et al.* (2009); Sekse *et al.* (2012); Pereira *et al.* (2014)) that the RBEs observed in profiles of different chromospheric lines are on-disk counter parts of solar spicules. In addition, it is also reported that the doppler velocity of RBEs

increases along their length in CHs when observed in the 8542 Å (Ca II) spectral line using the CRisp Imaging SpectroPolarimeter instrument (CRISP, Scharmer *et al.* (2008)) at the Swedish 1-m Solar Telescope (SST). However, no such trend was observed for QS RBEs (see Sekse *et al.* (2013) for detailed discussion). This correspondence between the increasing trend of doppler velocity of RBEs (observed in the chromosphere) and higher speeds of the network jets (observed in the TR) in CHs provide more evidence that the RBEs, or on-disk spicules may be the signatures of lower-temperature and less-accelerated parts or phases of the network jets.

The distribution and average value of foot-point brightness increase is almost the same in CH and QS. The similar magnitude probably suggests the same generation mechanism of the network jets in both the regions. In addition, we have studied the inter-relation between the jet properties in respective regions in Figure 4.5. We find that the apparent speed of the network jets is independent of increase in foot-point brightness, although it is very much dependent on length of the jets. As indicated in Figure 4.5, speed and length of the jets are highly correlated in both CH and QS regions with a correlation coefficient of 0.80 for CH and 0.74 for QS jets. On the other hand, brightness increase at foot-points appears to be independent of any of the dynamical properties of the jets. This again reflects that the basic mechanism (*e.g.* magnetic reconnection) responsible for generation of the network jets is of very similar nature in CH and QS. However, as the jets propagate in different ambient magnetic environments in the two regions, most of the dynamical properties get considerably effected.

The recurrence of these high speed network jets from the same location suggests that the oscillatory reconnection might be the possible mechanism for generation of the jets. It has already been demonstrated by Murray *et al.* (2009) and McLaughlin *et al.* (2012) that such an reconnection can trigger quasi-periodic upflows. It is also reported that the Lorentz-force driven models are able to produce, heat and

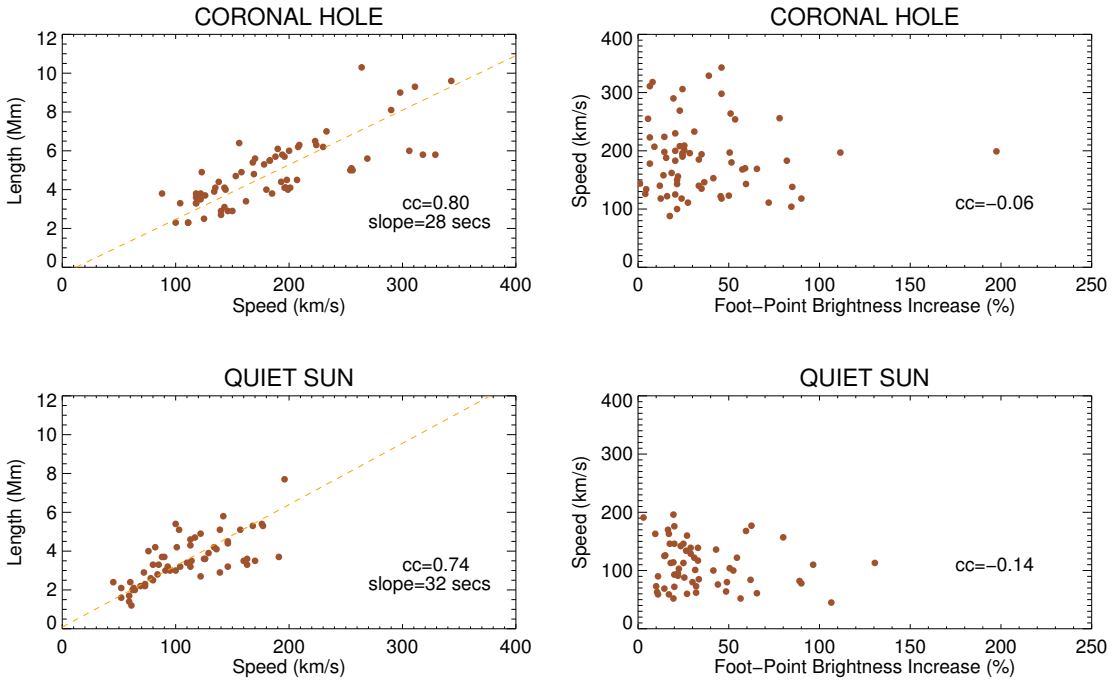

FIGURE 4.5: Scatter plots for different parameters of network jets. cc indicates correlation coefficient.

accelerate spicules (Martínez-Sykora *et al.* 2011b; Goodman 2014). The recent numerical simulation by Goodman (2014) even claims that the Lorentz-force driven jets can have speeds as high as 66-397 km s^{-1}, similar to observed in the present study. However, the pressure driven jets (*e.g.* Martínez-Sykora *et al.* (2011b); Judge *et al.* (2012)) are reported to gain speeds $\sim$ 60 km s^{-1} only. Thus, based on the above mentioned numerical simulation results along with our observations, it can be concluded that the evolution of magnetic field at small scales has a key role in the generation and acceleration of high-speed jets in the chromosphere and TR. It is important to note that the optically thin Si IV lines do not have enough S/N in the 4s-exposure data, so the spectral data can not be used in such observations. Without detailed analysis of the spectroscopic data, we can not exclude the possibility that some of the apparent motions may be reflection of the ionization front or even shock waves and are likely not real mass flows (see Tian *et al.* (2014) for a detailed discussion). Recent spectral analysis by Chen *et al.* (2019) shows the regions of enhancement of both wings or double peak behaviour of transition regions emission lines to be located at either the foot-points of network

jets or transient compact brightenings. On the other hand, the locations with enhancements only at the blue wing are mainly located on network jets, away from the foot-points. Additionally, Huang *et al.* (2017) observed that the chromospheric jet-like events in the wing of the Hα line can trigger enhancements in both or single wing of the transition region emission lines. In particular, they conjecture that the double peak behaviour observed for Si IV 1394 Å line arises mainly due to the additional absorption components from Fe II and Ni II lines, caused by the presence of chromospheric jet-like features.

We have already indicated that the mechanism generating of the network jets should be similar in the CH and QS. If the generation mechanism is magnetic reconnection in the chromosphere (e.g Shibata *et al.* (2007); Yurchyshyn *et al.* (2013); Deng *et al.* (2015); Ni *et al.* (2015)), it would indicate that there is no significant difference of magnetic structures in the chromospheric layers of CH and QS. In CH, it is probably small chromospheric loops that reconnect with open flux in the network. In case of QS, small chromospheric loops reconnect with the legs of the coronal loops. Higher up in the TR and corona, there are probably not many loops in the CH. While in QS, there are still a lot of TR and coronal loops present. Our observations provide direct imaging evidence to validate this proposed idea as we have found some small compact loop-like bright features to be present in QS (likely the TR loops reported by Hansteen *et al.* (2014)). An example of such a loop detected in our observations in QS is showcased in Figure 4.6. These bright loop-like regions have typical extents of $\sim 5''$ and are generally devoid of the network jets. In CH, no such features can be observed, suggesting that, at the layers of TR in a CH, there are basically only open field lines and almost no loops. This result is also consistent with the findings of Wiegelmann and Solanki (2004); Tian *et al.* (2008a) that loops reside only at very low layers in a CH. The difference in magnetic morphology in higher layers is likely responsible for the different propagation of the network jets in the two regions, leading to higher speed and longer distance in CHs. The fact that the observed QS compact loops

are generally devoid of the network jets actually suggests that the network jets occurred below the height of these TR loops, which means that the network jets are likely produced in the chromosphere.

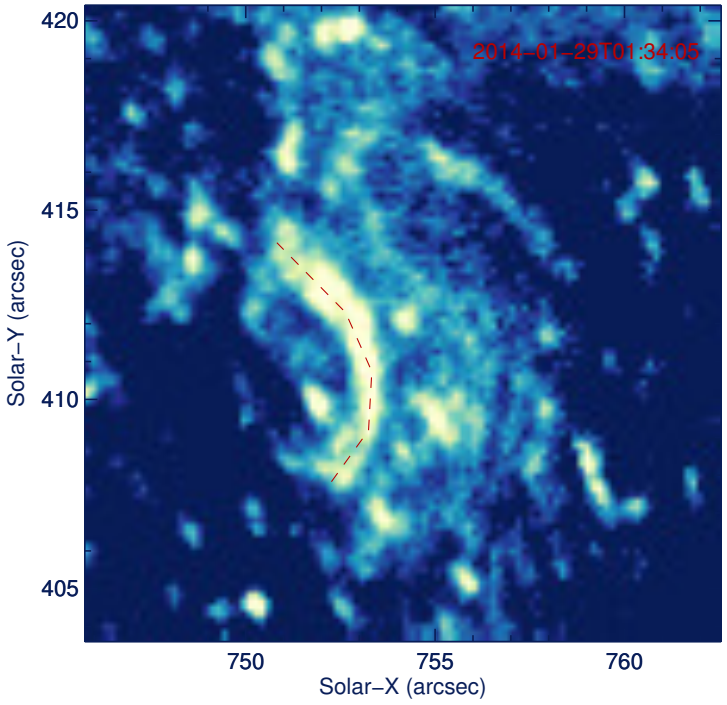

FIGURE 4.6: One example of compact bright loop observed in QS. The red curve marks the loop-like feature.

In addition to explanations involving magnetic reconnection, there are some other possible models that could account for the observed properties of the jets. Hollweg *et al.* (1982) proposed that magnetohydrodynamic waves could exert a time-averaged upward nonthermal pressure and thus "levitate" the cool chromosphere. This was suggested as a formation mechanism for large, Type I solar spicules (see also de Pontieu (1999); Kudoh and Shibata (1999); Matsumoto and Shibata (2010)). Cranmer and Woolsey (2015) recently extended this idea to smaller-scale turbulent Alfvénic motions in CH network regions, and found that nonlinear mode conversion into chromospheric shocks may provide intermittent upflows of the right order of magnitude. Such a model produces vertical excursions in the height of the transition region of order 1 to 6 Mm over timescales of 20 to 60 seconds, which gives rise to apparent jet-like velocities of 50 to 200 km s^{-1}. The

wave/turbulence model for jet formation is observationally distinguishable from a reconnection-based model, in that the former does not require magnetic field of both polarities to be present at the jet footpoint location.

The prevalence of the network jets and that the jets reach to higher layers ($\sim$ 5 Mm) in both the regions (CH and QS), implies that they may play an important role in supplying mass and energy to the corona and solar wind. At this stage, one must reconcile the implications on the origin of the solar wind (Tian *et al.* 2014) due to presence of these intermittent small-scale network jets in the TR. However, IRIS observations are unable to detect heating signatures of these network jets at coronal temperatures as IRIS is designed to study mainly the chromosphere and TR and over its spectral coverage, there is only one line present, Fe XII 1349 Å, which is formed at normal coronal temperatures but it is usually very weak or absent. The observations show only that the jets reach at least $\sim 10^5$ Kelvin, but presently we cannot account if they can be heated to coronal temperatures.

In the near future, we will try to track these jets to coronal structures. One way, for instance, would be to investigate the possible connection between these jets and the hot intermittent upflows along plume-like structures (McIntosh *et al.* 2010; Tian *et al.* 2011c; Pucci *et al.* 2014; Pant *et al.* 2015b) and the blue shift patches of lower coronal lines (Tian *et al.* 2008b, 2009; Fu *et al.* 2014). Moreover, one must also try to address the question of dissipation of energy by the network jets in the corona, *e.g.*, whether they trigger compressional waves or not (Gupta *et al.* 2012; Uritsky *et al.* 2013; Jiao *et al.* 2015; Pant *et al.* 2015b). This aspect can be studied in more details in order to further explore the difference in mechanisms between CH and QS for generating network jets and for processing the supplied mass and energy by these jets to the corona and solar wind. In this context, new instrumentations with similar spatial and spectral resolution as that of IRIS, along with wider wavelength coverage, that can provide co-spatial and co-temporal observations of the TR and corona, are also desirable. For instance, the Extreme Ultravoilet Imager (EUI)

and Spectral Imaging of the Coronal Environment (SPICE) instruments onboard the Solar Orbiter spacecraft (Müller *et al.* 2013), to be launched in October 2018, can provide more insight into the heating process of the network jets. This will serve as a great opportunity for a better understanding of the relationship between the TR network jets and coronal structures and outflows.

4.4 Conclusions

Our IRIS observations reveal the presence of network jets in QS as well as in CH. We have conducted some comparative analysis between CH and QS regions based on the properties of these jets. It must be noted that the results obtained are limited by the number of data-sets used for the study. As mentioned earlier, we have used only two observations in CH and two in QS regions. Hence, presently we are not sure if the results will change by using more observations. Our results from the current study are summarized as follows:

1. CH jets appear to be faster and longer than those in QS regions. This is most likely a consequence of different magnetic configurations of the two regions with open magnetic field lines dominant in CH and magnetic loops often present in QS. This proposed idea is well supported by our observations which clearly show some compact bright loops to be present in QS but generally absent in CH at TR heights.

2. Recently, RBEs are reported to show an increasing trend in the doppler velocity along their length in CH. The higher apparent speed of network jets in CH can provide evidence to support the proposed idea that TR network jets are the accelerated phase of RBEs in coronal holes.

3. The similar distribution and average value of increase in foot-point brightness indicates towards the same generation mechanism of these jets in both regions. Moreover, we find a good correlation between apparent speed and length of the jets. On the other hand, the foot-brightness increase seems to be independent of any of the dynamical properties of the jets.

4. As these jets reach up to higher layers (length of ~ 5 Mm), they can serve as reasonable candidates for supplying mass and energy to the corona and solar wind. However, it is important to note that IRIS observations are unable to detect the signatures of these jets beyond $\sim 10^5$ Kelvin.

Chapter 5

IRIS view on two-component structure of the transition region emission lines[†]

5.1 Introduction

The solar TR, the interface between chromosphere and corona, is the ideal region to study the mass and energy transport from photosphere to corona responsible for coronal heating. Imaging instruments allow us to observe the evolution of different structures in the solar atmosphere. However, they can only provide information of the apparent motions in the observational plane. On the other hand, spectroscopic data gives details about the line profiles and thus enables us to investigate

[†]All the animations that are referred to in this chapter are available at `https://www.dropbox.com/sh/6x39aztaknff6c4/AAAB5IEul7ABR_mP_0deiVe0a?dl=0`.

the thermal and dynamic structure of the observed plasma. For a detailed understanding of different physical processes of highly dynamic solar TR, joint imaging and spectral observations with remarkable temporal, spatial and spectral resolution is required, as achieved by IRIS (*Interface Region Imaging Spectrograph*, De Pontieu *et al.* (2014b)).

The profiles of optically thin emission lines originating in the solar TR serve as a sensitive tool to understand the structure and dynamics of the lowermost corona and its connection to the chromosphere and photospheric magnetic activity. Asymmetries in the TR emission lines have been observed since the late 1970's. Kjeldseth Moe and Nicolas (1977) were the first to observe significant deviations of UV emission line profiles from single Gaussian shape by using data from EUV spectrograph on Skylab. They mentioned the requirement of a secondary emission component in order to explain the peculiar line profiles. Almost a decade later, Dere and Mason (1993) analysed rocket flight data of *High Resolution Telescope and Spectrograph* (HRTS) where the secondary component was speculated to be the signature of unresolved explosive events. Peter (2000, 2001) performed an extensive study on asymmetries of TR emission lines using data from SUMER (*Solar Ultraviolet Measurements of Emitted Radiation*) spectrograph (Wilhelm *et al.* 1995) on board SoHO (*Solar and Heliospheric Observatory*). Both studies emphasised on the presence of a secondary component in addition to line core and source of the two spectral components were interpreted to be related to different physical structures of TR. In recent past, different observations from EIS (*Extreme-ultraviolet Imaging Spectrometer*, Culhane *et al.* (2007)), on board *Hinode*, have also revealed the presence of asymmetries in TR and coronal line profiles (*e.g.,* De Pontieu *et al.* 2009; De Pontieu and McIntosh 2010; McIntosh and De Pontieu 2009b,a; Peter 2010; Martínez-Sykora *et al.* 2011a; Tian *et al.* 2011a,b).

De Pontieu *et al.* (2009) developed a novel technique called *Red(R)-Blue(B) asymmetry analysis* to quantify the asymmetries in the observed line profiles. De Pontieu and McIntosh (2010) and Tian *et al.* (2011a) used the velocity derived from the *R-B asymmetry analysis* as an initial guess for the secondary component to perform double Gaussian fit to observed coronal spectra. Martínez-Sykora *et al.* (2011a) illustrated in great detail that the *R-B* asymmetry profiles can be used to perform reliable double Gaussian fits to emission lines. Tian *et al.* (2011b) modified the technique of *R-B* asymmetry analysis to resolve the second emission component from non-Gaussian line profiles and concluded that the modified technique has a better ability to accurately quantify the properties of the secondary component as compared to the original one. Very recently, the *R-B* asymmetry analysis technique is used to estimate asymmetries in some TR line profiles for a few particular cases and events observed by IRIS (*e.g.,* Tian *et al.* 2014; Huang *et al.* 2014, 2017; Samanta *et al.* 2015; Hou *et al.* 2016). These non-Gaussian line profiles suggest towards the presence of at least two emission components: a primary spectral component accounting for background emission and a secondary component associated with high-speed flows. The latter has been proposed to play a vital role in chromosphere-corona mass and energy cycle. Wang *et al.* (2013) indicated towards a different scenario in which non-Gaussian spectral line was assumed to be composed of three components: a primary component with two secondary components, one to account for up-flow and another one for down-flow.

In the present study, we explore the possibility of *R-B* guided double Gaussian fit to be able to resolve the asymmetries in Si IV (1403 Å) TR line observed with IRIS. Using simultaneous LOS magnetograms from HMI (*Helioseismic and Magnetic Imager*, Schou *et al.* (2012)) on board *Solar Dynamics Observatory* (SDO) and slit-jaw images (SJIs) of chromosphere along with TR spectral data from IRIS, we showcase a detailed analysis of spectral properties of different components of line profile and their possible relation to corresponding features in SJIs and magnetograms. With IRIS, we now have a better opportunity to obtain direct

imaging observations of solar chromosphere and TR along with spectral data, which is absent in any other existing instruments. These special abilities of IRIS have enabled us to study the spectral properties of small-scale transients observed in chromosphere and TR in greater detail as presented here.

5.2 Observations and Data-Analysis

5.2.1 Details of Observations

The data presented in this study is acquired during an IRIS raster scan of a low latitude Coronal Hole (CH) from October 09, 2013 23:26 UT to 10 October, 2013 02:57 UT. This data has been used by (Tian *et al.* 2014) also but in that study they have presented single Gaussian fitting results only. In Figure 5.1 the observed region on the solar disk is shown as the rectangles outlined in the HMI magnetogram and the coronal image taken in 193 Å passband of the *Atmospheric Imaging Assembly* (AIA,Lemen *et al.* (2012)) on board SDO. Centered at $(511'', 296'')$, the spectroscopic data covers $141'' \times 174''$ region of the CH with the SJIs having a field of view (FOV) of $167'' \times 174''$. This 400 step very large dense raster scan has a step cadence of 31.6 seconds with the slit-width of $0.35''$ and pixel size along the solar-Y axis to be $0.1664''$. The SJIs are taken with a cadence of 130 seconds and have spatial resolution $\approx 0.33''$. Every observation in this data-set has an exposure time of 30 seconds which is adequate to have a good signal to noise ratio (S/N) in order to perform reliable Gaussian fittings. For spectral analysis, we are concentrating on the Si IV (1403 Å) line formed at $log_{10}T \approx 4.9K$ which is one of the prominent TR emission line observed with IRIS and is free from other line blends. From IRIS imaging data, we use SJIs in the C II 1330 Å passband which

samples emission from the upper chromosphere. For the corresponding photospheric magnetic field information, HMI LOS magnetograms with a cadence of 45 seconds and spatial resolution of 1.01″ are used.

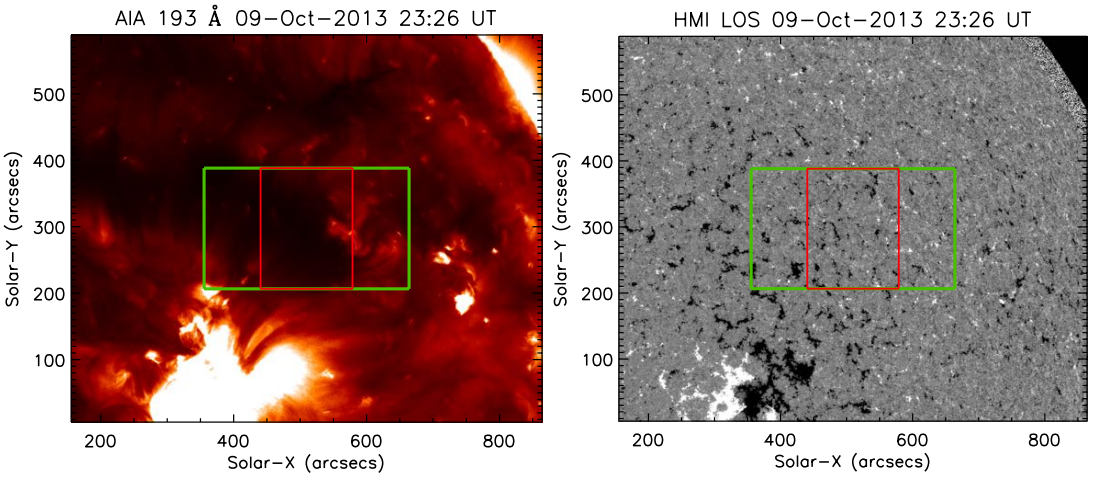

FIGURE 5.1: AIA 193Å image and HMI LOS magnetogram at the start time of the IRIS observations. The SJI FOV is marked by *green* rectangle and raster FOV by red rectangle.

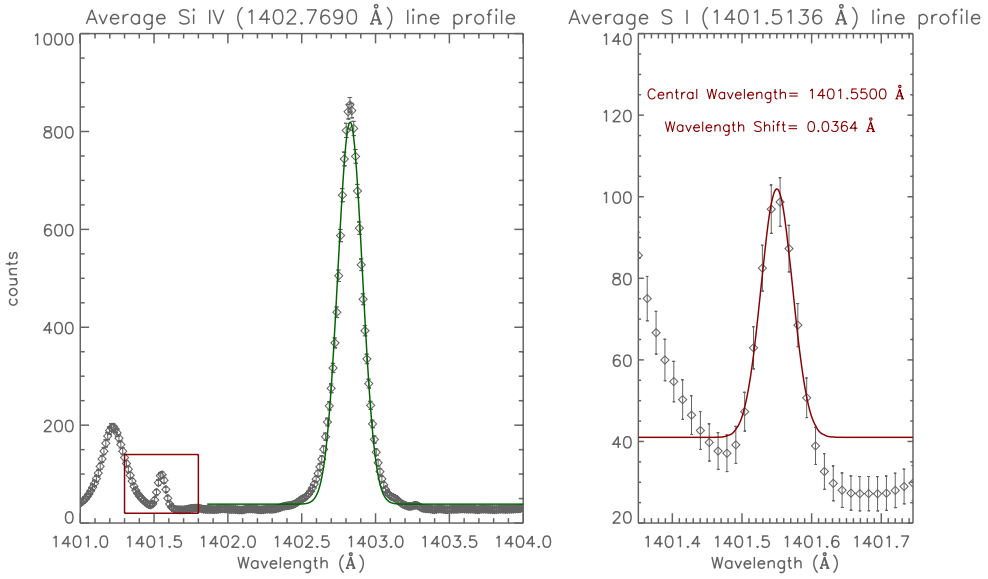

FIGURE 5.2: Average Si IV and S I line profiles. The right panel is enlarged view of the *red* rectangle indicated in the panel on left. The diamonds (with errors bars) marks the observed (averaged over the field of view) line profiles. The over-plotted solid lines show single Gaussian fits to the line profiles.

The IRIS 1330 Å SJIs and HMI LOS magnetograms, both have a strong continuum contribution, which has enabled us to have a straightforward alignment between IRIS and HMI observations. The standard solar soft routines of *hmi_prep.pro* and *drot.pro* is applied to HMI data-set before the co-alignment. The calibrated level 2 data of IRIS is used in the study. Dark current subtraction, flat-field correction, and geometrical correction have been taken into account in the level 2 data. Before applying any fitting procedure, the spectral data is despiked first in order to remove abrupt bright spikes which could be present due to some random noise and may lead to spurious Gaussian fitting. At first, a single Gaussian fit is performed on the average (over all the pixels in the raster scan) profile of the photospheric S I 1401.5136 Å line for absolute calibration of wavelength. Figure 5.2 shows the average profiles of Si IV 1402.7690 Å (or simply 1403 Å) and S I 1401.5136 Å line and clearly demonstrates the requirement of shifting wavelength axis by 0.0364 Å to have absolute wavelength calibration. The most important step of data-analysis includes performing a single Gaussian fit and R-B asymmetry guided double Gaussian fit at all spectral locations in the raster scan, which is discussed in details in next subsection. Before applying the fitting routines, we have performed running addition of 3 pixels in solar-X direction, 6 pixels in solar-Y direction and 3 pixels in wavelength axis in the spectroscopic data which has improved S/N in order to have reliable single and double Gaussian fits.

5.2.2 R-B Guided Double Gaussian Fitting

The technique of Red-Blue (RB) asymmetry analysis was first introduced in 2009 to quantify the magnitude and velocity of the secondary emission component in some asymmetric coronal line profiles. It is based on a comparison of the two wings of the line profile in the same velocity ranges. The blue wing emission integrated over a narrow spectral range is subtracted from that over the same range in the red wing. The range of integration is then sequentially stepped outward from

the line centroid to build an RB asymmetry profile (or simply RB profile). The magnitude and velocity of the secondary emission component can then be inferred from this RB profile. Initially, the line centroid which separates the blue and red wings was simply taken as the centroid derived from a single Gaussian fit to the line profile (see De Pontieu *et al.* (2009) and Martínez-Sykora *et al.* (2011a) for details). Later on, Tian *et al.* (2011b) demonstrated that using the spectral position corresponding to the peak intensity of the observed line profile as the centroid can resolve the secondary component more accurately.

Here we apply the RB asymmetry technique, as indicated by Tian *et al.* (2011b), to every Si 1403 Å line profile in the raster scan (except for the ones where S/N is very low). We first apply a single Gaussian fit to the line profiles (few representative examples are shown in Figure 5.3). It can be clearly observed that the single Gaussian fits significantly deviates from the highly asymmetric line profiles. To determine the spectral position corresponding to the peak intensity, now we only fit the central 18 pixels around the peak with a single Gaussian. This Gaussian center is then taken as the centroid of the line profile in order to generate the R-B profile. The spectral (velocity) bin size is chosen to be 10 km/s. The calculated RB profile is then normalized to the peak intensity value of the observed profile. A negative/positive R-B value indicates an enhancement of the blue/red wing in the velocity interval.

For performing double Gaussian fit, the peak intensity, velocity, and width derived from a single Gaussian fit are directly used as the initial guess for the primary Gaussian component. The single Gaussian background itself is used as the initial value of the double Gaussian background. For asymmetric line profiles (where the unsigned value of average R-B profile is greater than 0.02), the peak intensity and velocity obtained through the RB analysis are used as the initial values for the spectral parameters of the secondary Gaussian component. The value of the width of the secondary component is initially set same as the primary component.

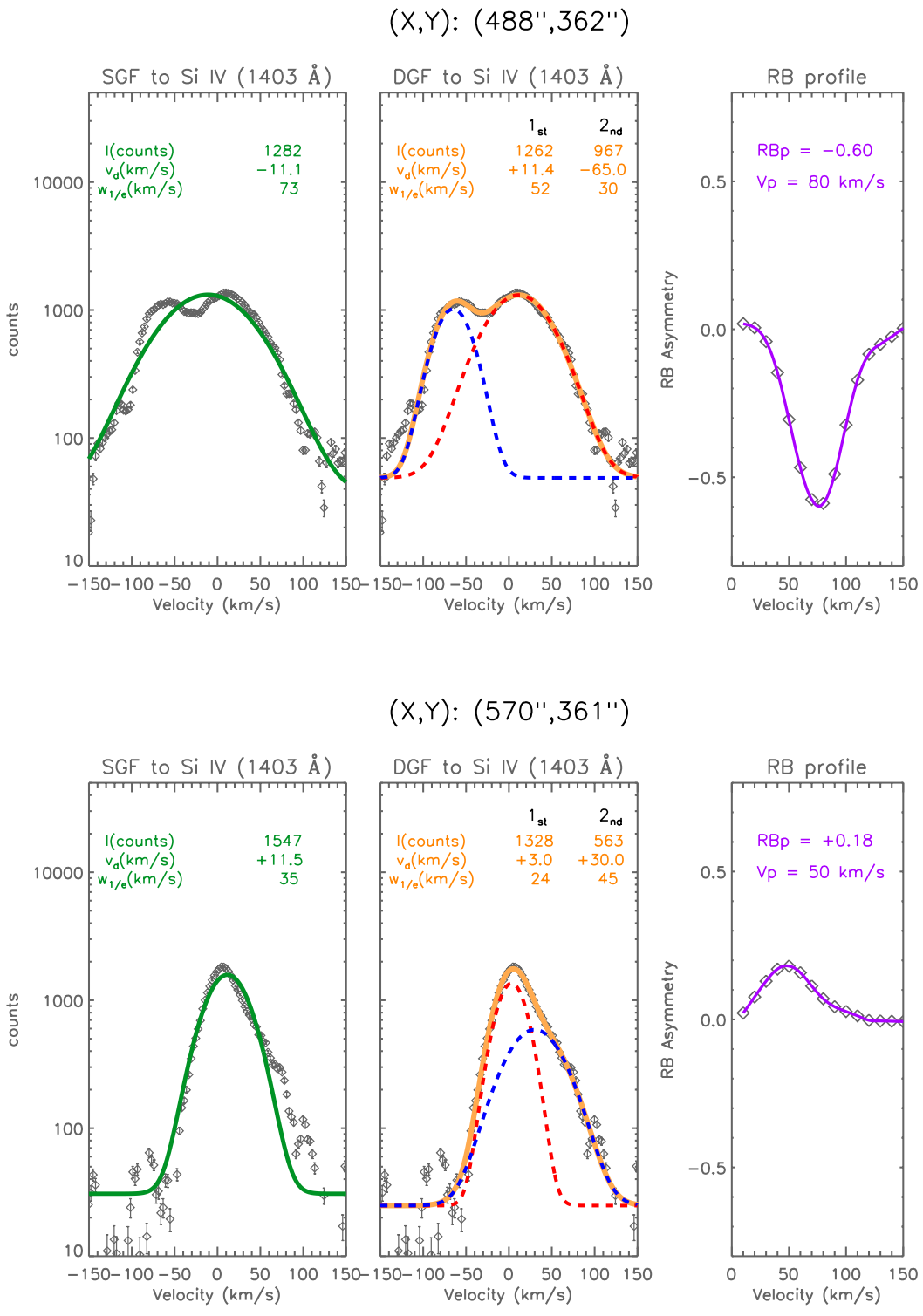

FIGURE 5.3: Representative examples of single Gaussian fits (left panels), RB asymmetry profiles (right panels) and double Gaussian fits (middle panels). Peak intensity (I), Doppler velocity (v_d) and Doppler width ($w_{1/e}$) of single Gaussian and both components of double Gaussian fits are listed in respective panels. The peak values of RB profiles (RB_p) occurring at the velocity (V_p) are also indicated.

For symmetric line profiles (where the unsigned value of average R-B profile is less than 0.02), the initial guess for the secondary component is considered to be same as that for the primary component. During the iterations, the peak intensity of primary component and background intensity is allowed to vary from 0.5 to 1.5 times of the corresponding initial values. The allowable range for the peak intensity of the secondary component is set to be 0.3 to 6.0 times of its initial guess value. The velocity is allowed to move to the blue or red of the initial position by 12 spectral pixels ($\approx 30\,km/s$) for the primary component and 21 pixels for the secondary component($\approx 55\,km/s$). The range for the width of primary component to be from 0.2 to 1.2 times of its initial guess and that for the secondary component is from 0.4 to 8.0 times. The algorithm undertakes a global minimization of the difference between the observed and fitted spectrum.

5.3 Results and Discussions

5.3.1 Single vs. Double Gaussian Fits

The comparison between single and double Gaussian fits is achieved through reduced chi-square (χ^2_r) statistics (Bevington and Robinson 1992). In Figure 5.4 the distribution of the χ^2_r of the whole data-set for the single and double Gaussian fits are shown. Figure 5.4 clearly demonstrates the need for a double Gaussian fit in a substantial fraction of the observed data. The high values of χ^2_r obtained here do not necessarily mean the very bad quality of the fits. This could possibly be due to underestimation of errors in the data, which increases the values of χ^2_r systematically for both the fitting models. Despite this problem, one can at least compare the χ^2_r distributions of the two fits. It is obvious from Figure 5.4 that in general, the double Gaussian fits are superior to the single Gaussian fits. The distribution for the double Gaussian fitting model shows a significant improvement

in the values of χ_r^2 at most of the locations in the data-set. This is reflected in the lower value of *mode* for the double Gaussian distribution (14) as compared to that for single Gaussian (19). The single Gaussian fit fails to be a good representation of the data since it cannot account for the excess emission in the wings (see examples in Figure 5.3 and Figure 5.6).

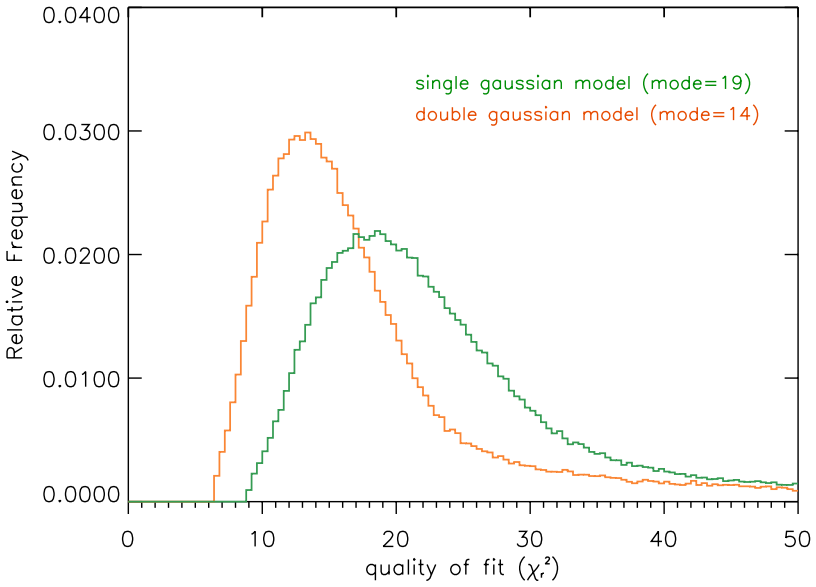

FIGURE 5.4: Distribution of χ_r^2 for all single Gaussian and double Gaussian fits with latter being superior.

χ_r^2 statistics also enables to distinguish between regions where a second component is present and where one component is sufficient to describe the data. In this study the following criterion is used to decide whether a double Gaussian fit is required and reliable: χ_r^2 of the double Gaussian fit has to be less than 0.8 of the single Gaussian fit, i.e. the detection of the second component must significantly improve the value of χ_r^2. The locations which fulfil the criteria are termed as "double Gaussian preferred" locations and others to be "single Gaussian preferred" locations. The results of the fits are shown in Figure 5.5. The left panels show the parameters for single Gaussian fitting, middle panels for primary/core (1st) component and the right one for the secondary (2nd) component. In the parameter maps for the double Gaussian fits, the locations where single Gaussian fit is preferred over double Gaussian fit are masked by colour *grey*. In the present

data-set, almost 42% locations prefer double Gaussian fit. The contours in the images outline the locations of the bright network as obtained from the intensity map of single Gaussian fits.

It is clearly evident from Figure 5.5 that double Gaussian fit is preferred mostly in the bright network elements and ambient locations (collectively termed as network regions). Peter (2000, 2001) obtained similar results and mentioned that in the inter-network a simple single Gaussian fit is sufficient to describe the data adequately. But almost everywhere in the network a two Gaussian fit is needed. In Figure 5.6 four example spectra, two for network regions (double Gaussian preferred, Figure 5.6 (a) and (b)) and two for inter-network regions (single Gaussian preferred, Figure 5.6 (c) and (d)), are shown with their respective spatial locations in the SJIs. In the network, the asymmetric line profiles are clearly evident and a double Gaussian fit is excellent. The conclusion from the above discussion is that the double Gaussian fits are required mostly in the network regions, while the single Gaussian fits seem to be sufficient in most parts of the inter-network.

5.3.2 Distribution of Fit Parameters

The single Gaussian fit parameters (left panels of Figure 5.5) clearly outline the well-known network-internetwork structure of chromosphere and transition region. The line is broader and shifted towards the red over the network regions, while the shifts are small in the inter-network. For double Gaussian fit parameters, it is difficult to draw conclusions by observing the parameters maps with eyes as 58% locations are blended in *grey* as they prefer single Gaussian fit. Therefore the distributions of peak intensity, Doppler velocity and width will now be studied quantitatively. For this purpose histograms of respective fit parameters are analysed and a comparison is made between single and double Gaussian fits. The histograms are shown in Figure 5.7 with the respective mean values listed.

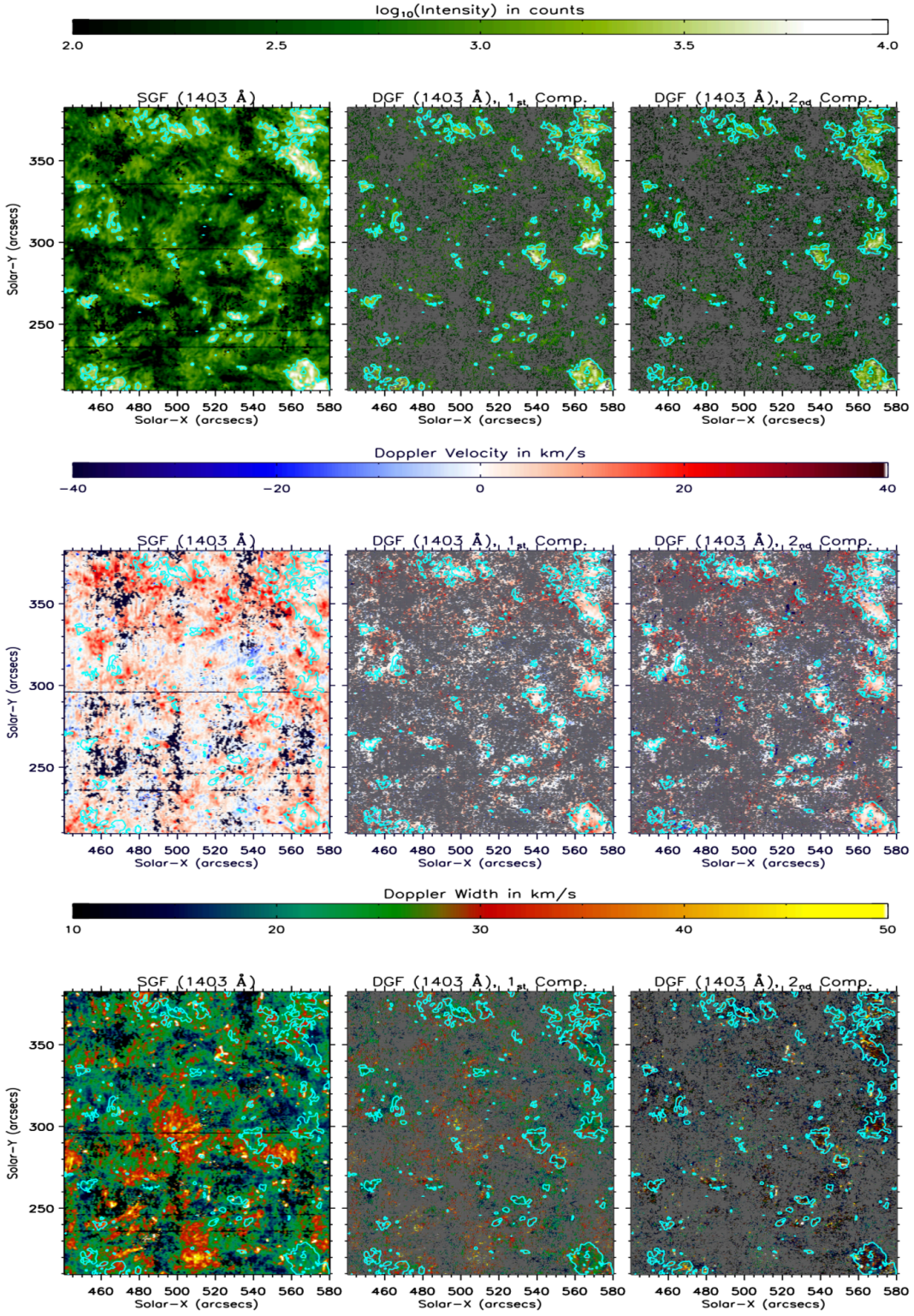

FIGURE 5.5: Spectral parameter maps for single Gaussian fits (SGF, left panels) and both components of double Gaussian fits (DGF, middle and right panels). The locations of bright network elements are enclosed by *blue* contours obtained from peak intensity map of SGF. SGF preferred locations are blended in *grey* in maps of DGF. The top row shows peak intensity, middle row Doppler velocity, and bottom row shows Doppler width.

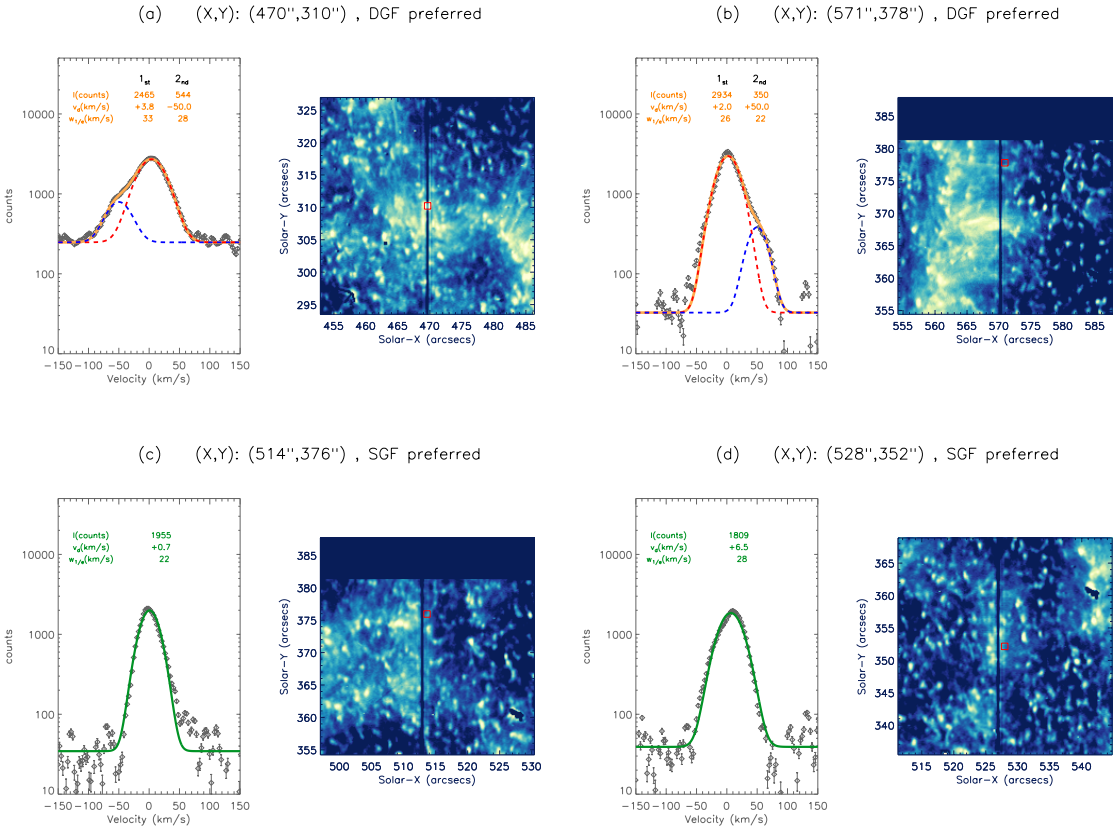

FIGURE 5.6: Sample spectra: (a) and (b): DGF preferred cases; (c) and (d):SGF preferred cases. Tiny *red* box in SJIs marks the location of the respective spectral profile.

As shown in Figure 5.7 (a), the primary components, in general, are brighter by a factor of about 2 compared to the secondary components. On average the secondary component contributes about 34% to the total intensity of the line profile (*i.e.* second : core $\sim 1:2$). The histograms for Doppler shifts are displayed in Figure 5.7 (b). The single Gaussian fits and core component of double Gaussian fits shows the well-known red-shifts. In contrast, the distribution of secondary component is comparatively less weighted towards the red. While only 18% of the single Gaussian fits and 23% of the core component of the double Gaussian fits show blue-shifts, more than 27% of the secondary components are blue-shifted. A close inspection of the distribution of Doppler velocity for secondary component reveals the presence of excess bumps located at $\sim \pm 25\ km/s$. This indicates the presence of high-speed and small-scale flows in TR (TR transient flows). The relation of

TR transient flows with the locations with high Doppler velocities is discussed in detail in sub-section 5.3.3. The histograms of non-thermal velocity/width of the Gaussian components are plotted in Figure 5.7 (c). Though on average primary components are broader than secondary components, the distribution of secondary component spans a wider range than that of the primary component. The peak of secondary component distribution at $\sim$ 15 km/s again reflects the presence of small-scale sudden flows or TR transient flows (which will be discussed in the next sub-section).

5.3.3 TR Transient Flows

It is indicated in the previous sub-section that the distributions (one-dimensional histograms) of Doppler shifts and widths of secondary component reflect the presence of TR transients flows (or simply TR transients). The significance of these transients is analysed further with the aid of two-dimensional histograms which can provide inter-relation between the spectral properties. Figure 5.8 showcases different two-dimensional histograms for secondary component of double Gaussian fits. Three distinguished populations of features can be very clearly observed from all the plots in the figure. The central population in Figure 5.8 (a) represents the locations with small Doppler shifts of secondary component. The presence of two satellite populations with high Doppler shifts (> 20 km/s) again reveal the existence of high-speed flows as concluded from one-dimensional histograms of Doppler shifts in the previous section. From Figure 5.8 (b) it can be noticed that the satellite populations of the secondary component (populations of major interest here) show high Doppler shifts but do not posses high values of peak intensity. These locations of high Doppler speeds with moderate intensities can be proposed to be related to high-speed, small-scale and short-lived jets (or transients) present in TR. Figure 5.8 (c) allows one to relate the high shift locations with the line widths.

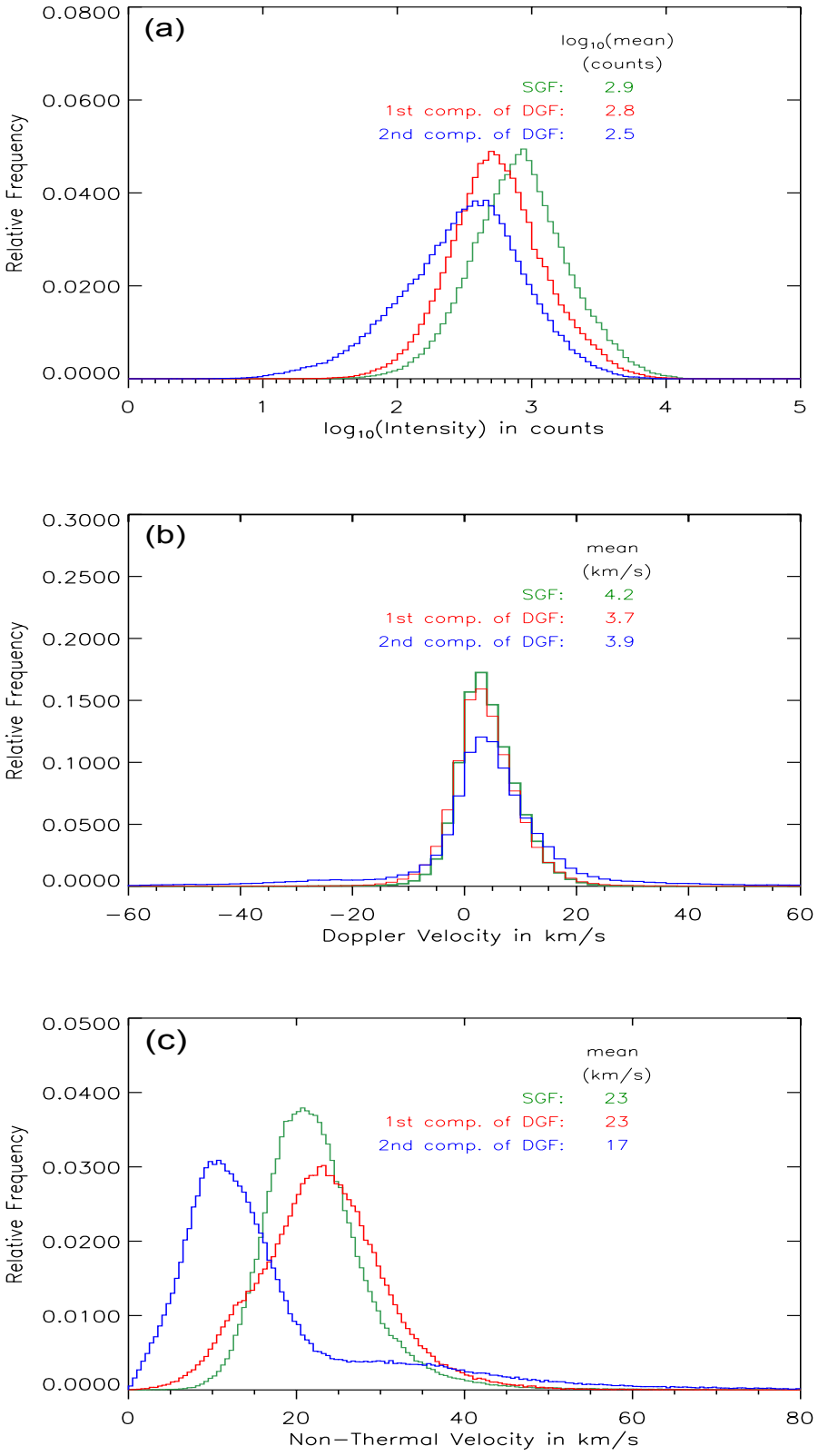

FIGURE 5.7: Distributions of peak intensity (a), Doppler velocity (b) and non-thermal velocity (c).

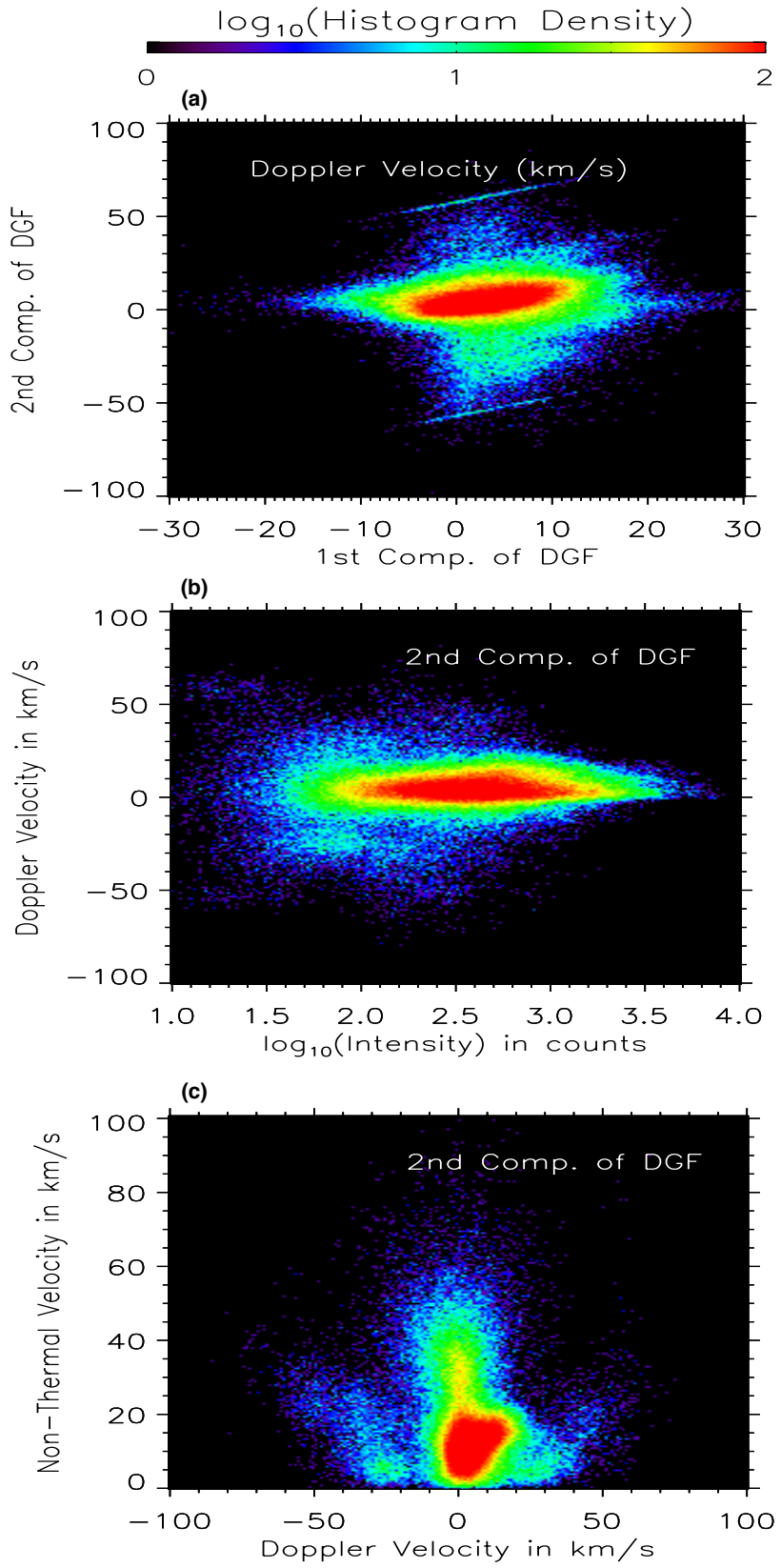

FIGURE 5.8: Two-dimensional histograms for different spectral properties of secondary components showing three distinct populations of features present in TR.

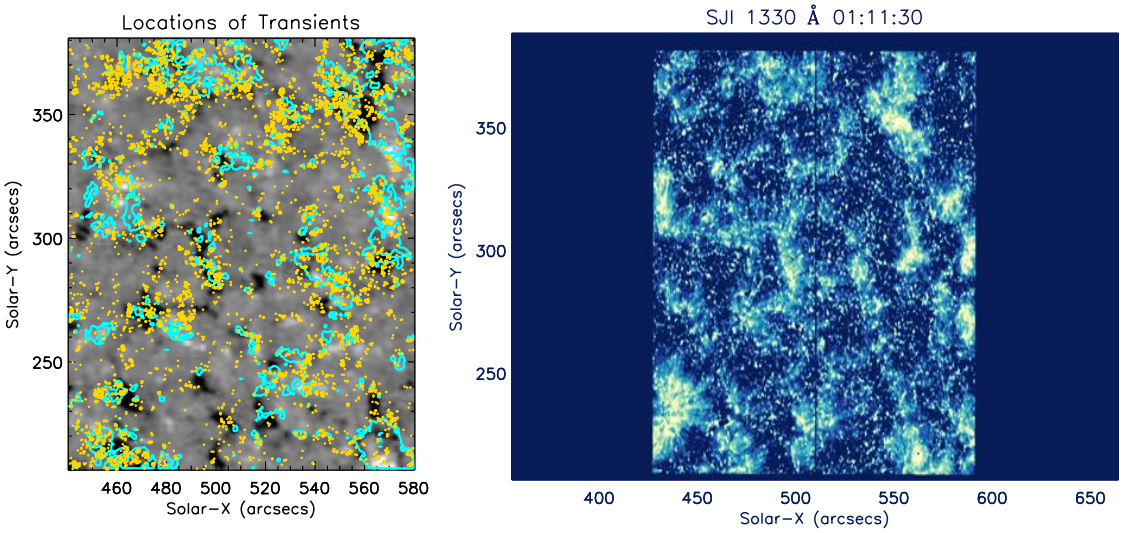

FIGURE 5.9: Locations of transient flows marked by *yellow* dots over time-averaged HMI LOS magnetogram. Blue contours enclose the network regions. A particular snapshot from the time series of 1330Å SJIs is also shown.

The three distinct populations observed in the two-dimensional histogram in Figure 5.8 (c) posses the following properties: 1) high blue shifts and non-thermal widths up to 40 km/s, 2) high red shifts and non-thermal widths up to 40 km/s, and 3) low Doppler shifts with a wide range of values of non-thermal widths (up to 80 km/s). The first two populations (satellite populations) mentioned above have moderate values of peak intensity (see Figure 5.8 (b)) and thus represent clear signatures of transient flows. The third (central) population is expected to be related with either bi-directional jets which increases mostly line-width (do not effect Doppler velocity much because of excess emission in both the wing simultaneously) or unresolved transverse/swaying motions and Alfvén waves or small-scale twists (unresolved torsional Alfvén waves, van Ballegooijen *et al.* (2011)) which cause broadening of line profiles. De Pontieu *et al.* (2015) showed that the non-equilibrium ionization of the network region plasma can also result in excess line broadening, perhaps by having a range of transients of different velocities along the line-of-sight.

From the above discussions of two-dimensional histograms in Figure 5.8 one can conclude that the locations of transient flows possess the following spectral properties: 1) the Doppler shifts of secondary component of double Gaussian fits are greater than 20 km/s, 2) the non-thermal widths of secondary components are less than 40 km/s, and 3) the values of peak intensity for the secondary components are less than 1000 counts (see double Gaussian preferred examples in Figure 5.6). The relation of the magnetic fields with the locations satisfying all the three above mentioned properties can be studied from Figure 5.9. In this figure, the contours (in *blue*) of peak intensity for single Gaussian fits are plotted over HMI LOS magnetograms averaged over the duration of the IRIS observation. The *yellow* points marks the locations which satisfy the three above mentioned spectral properties of transient flows. It is clearly reflected from Figure 5.9 that the TR transients predominantly occur near the boundaries of the network regions. On comparison with SJIs (also see the animations provided at `https://www.dropbox.com/sh/6x39aztaknff6c4/AAAB5IEul7ABR_mP_0deiVe0a?dl=0`), these locations can be seen to be associated with the complex jet structures and thus can be claimed as signatures of the type-II spicules (de Pontieu *et al.* 2007; Pereira *et al.* 2014) and network jets (Tian *et al.* 2014; Narang *et al.* 2016). Huang *et al.* (2014) showed that such locations can also be considered as the direct manifestations of the transition region Explosive Events (EEs, Innes *et al.* (1997a,b)). As concluded in Doyle *et al.* (2013), the secondary components of the transition region emission lines may also be related to the transient ionization effects during the dynamic-bursty events (reconnection-type events). The animations (`https://www.dropbox.com/sh/6x39aztaknff6c4/AAAB5IEul7ABR_mP_0deiVe0a?dl=0`) show that the intermediate regions between the very bright network and dark inter-network have quickly evolving small-scale magnetic elements of not too high magnetic strengths and thus have moderate values of intensity. This indicates that the small-scale and quickly evolving magnetic fields present near the edges of the network regions play a crucial role in the generation of the TR transient flows.

5.4 Conclusions

The unique capability of IRIS to provide high-resolution spectroscopic data with simultaneous images with unbeatable cadence is being extensively deployed in the present study. The previous instruments to observe chromosphere and TR were unable to achieve such a high spectral, spatial and temporal resolution. The spectral data studied in this work covers a large area of $141'' \times 174''$ and thus the spectral properties of Si IV (1403 Å) TR line are investigated with statistical significance. The technique of R-B asymmetry analysis is successfully employed on automated terms in order to resolve the asymmetric TR line profiles into two components and perform double Gaussian fits. The comparison of χ^2_r between single Gaussian fit and double Gaussian fit model reveals that the double Gaussian model is a better representation of the data and is preferred over the single Gaussian model in the network regions. From the one-dimensional histograms of the fit parameters, it is observed that on an average the secondary component of double Gaussian fits contributes about 34% to the total intensity of the line profile. The Doppler velocity distribution for secondary component shows the excess populations clustering near $\pm$ 25 km/s which are indicated to be related to TR transient flows by analyzing two-dimensional histograms.

With the aid of different two-dimensional histograms the spectral properties and specific locations of the transients are obtained. These locations predominantly happen to be at the boundaries of the network regions which can be clearly observed to be associated with spicules and network jets in the movies of the SJIs. A close inspection of HMI magnetogram image sequence shows that the intermediate regions between bright network and dark internetwork (*i.e* network boundaries) posses quickly evolving small-scale magnetic fields which are claimed to be responsible for generation of TR transient flows. It can be concluded from the present work that the secondary component of double Gaussian fits indeed reveals the presence of transients in chromosphere and TR. Hence, double Gaussian model

fitting to the spectral profiles is necessary to study small-scale short lived transients in details. This is important to obtain a better knowledge of TR structure and dynamics for the study of the mass and energy transport from the photosphere to corona responsible for coronal heating.

Chapter 6

High-frequency dynamics of an active region moss as observed by IRIS[†]

6.1 Introduction

Understanding the processes responsible for the heating of the upper atmosphere is the central problem in solar physics. Though highly debated (see reviews, Klimchuk (2006); Reale (2010); Parnell and De Moortel (2012)), two widely accepted mechanisms for converting magnetic energy into thermal energy are, impulsive heating by nano-flares (Parker (1988)) and wave heating by dissipation of waves. The heating processes are generally proposed to occur on small spatial and temporal scales, which were difficult to access completely with the typical resolution of

[†]Results of this work are under review in the Frontiers in Astronomy and Space Sciences.

All the animations that are referred to in this chapter are available at `https://www.dropbox.com/sh/i09ud4qvn28vmo3/AABYOVCqZv22Oak5iUbsyPuwa?dl=0`.

the previous instrumentations. In very recent past, with the advent of instruments with better temporal resolutions, various high-frequency oscillations of sub-minute periodicities have been reported to be present from chromosphere (Gupta and Tripathi 2015; Shetye *et al.* 2016; Jafarzadeh *et al.* 2017; Ishikawa *et al.* 2017) up to corona (Testa *et al.* 2013; Morton and McLaughlin 2013, 2014; Pant *et al.* 2015a; Samanta *et al.* 2016)) at sub-arcsec spatial scales. The quasi-periodic variations in the various observables of the solar atmosphere with the periods less than that of *p-modes* (~ 5 min) are generally referred as "High-Frequency Oscillations". The small-scale quasi-periodic flows resulting from oscillatory magnetic reconnection as well as the presence of various Magnetohydrodynamic (MHD) waves produce such observed perturbations in imaging and spectroscopic observables. These periodic/quasi-periodic perturbations/oscillations observed at such finer scales in space and time can thus be regarded as the manifestations of the reoccurring dynamic heating processes present at similar spatial (sub-arcsec) and temporal (sub-minute) scales.

Various MHD waves could be present simultaneously along with quasi-periodic flows or their presence could entirely be non-concurrent. The plausible mechanism/s for their origin might also be directly coupled in some cases or completely independent in others. For instances, Gupta and Tripathi (2015) detected short-period variability (30–90 s) within explosive events observed in TR by IRIS (De Pontieu *et al.* 2014b)) and related them to repetitive magnetic reconnection events. On the other hand, Jafarzadeh *et al.* (2017) observed high-frequency of periods 30–50 s in Ca II H bright-points in chromosphere using the SUNRISE Filter Imager (SuFI; Gandorfer *et al.* (2011)). They found the evidence of both compressible (sausage mode) and incompressible (kink mode) waves to be present in the magnetic bright-points. Shetye *et al.* (2016) reported transverse oscillations and intensity variations ($\sim$ 20–60 s) in chromospheric spicular structures using CRisp Imaging SpectroPolarimeter (CRISP; Scharmer *et al.* (2008)) on the Swedish 1-m

Solar Telescope. They argued the high-frequency helical kink motions to be responsible for transverse oscillations and compressive sausage modes to result in intensity variations. They further found the evidence of mode coupling between compressive sausage and non-compressive kink modes. They speculated that the presence of other spicules and flows possibly act as the external drivers for the mode-coupling.

By using the total solar eclipse observations of 11 July 2010 (Singh *et al.* 2011)), Samanta *et al.* (2016) detected significant oscillations with periods ∼6–20 s in coronal structures. They attributed these high-frequency oscillations as mixture of different MHD waves and quasi-periodic flows. Using High-resolution Coronal Imager (Hi-C; Kobayashi *et al.* (2014)) data, Testa *et al.* (2013) observed the variability on time-scales of 15–30 s to be present in the moss regions as observed in upper TR, which they found to be mostly located at the foot-points of coronal loops. They regarded such oscillations as the signatures of heating events associated with reconnection occurring in overlying hot coronal loops, *i.e.*, impulsive nano-flares. More recently, from the Chromospheric Lyα SpectroPolarimeter (CLASP Kano *et al.* (2012)) observations, Ishikawa *et al.* (2017) also reported short temporal variations in solar chromosphere and TR emission of an active region with periodicities of ∼10–30 s. They attributed these intensity variations to waves or jets from the lower layers instead of nano-flares. Morton and McLaughlin (2013, 2014) analysed the same active region moss observations of Hi-C as by Testa *et al.* (2013) and observed the presence of transverse oscillations with periodicities of 50–70 s. Pant *et al.* (2015a) also studied the same Hi-C observations and detected quasi-periodic flows as well as transverse oscillations with short periodicities (30–60 s) in braided structures of the moss. They indicated towards the coupling between the sources of transverse oscillations and quasi-periodic flows, *i.e.*, magnetic reconnection such that they could be possibly driving each other.

In the present work, we concentrate on the high-frequency (∼1–2 minute) dynamics of an active region (AR 2376) moss as observed by IRIS. IRIS have provided an unprecedented view of solar chromosphere and transition region with high temporal, spatial and spectral resolution. The joint imaging and spectroscopic observations of IRIS at high cadence provide us a unique opportunity to have a detailed analysis of different characteristics and mechanisms involved in the generation of high-frequency oscillations in TR moss regions.

6.2 Details of the Observation

IRIS observation of an active region (AR 2376) moss observed on 2015-07-05 from 05:16:15 UT to 07:16:23 UT is considered for the present analysis. Figure 6.1 shows the observation region on the solar disk, as outlined in the image taken in 193 Å pass-band of AIA (Atmospheric Imaging Assembly, Lemen *et al.* (2012)) and slit-jaw image (SJI) in 1400 Å at a particular instance as observed by IRIS. The bottom panel shows a typical light-curve at a particular location A (marked in the full FOV above) in the moss region in SJ 1400 Å intensity. The nature of the variation of intensity clearly reveals the presence of small amplitude quasi periodic oscillations along with bursty comparatively larger amplitude oscillations.

Centred at $146'', 207''$, the imaging data (slit-jaw images or SJIs) have a field of view (FOV) of $119'' \times 119''$. The SJIs are taken with a cadence of 13 seconds and have spatial resolution $\approx 0.33''$. The simultaneous large sit-and stare spectroscopic data has a cadence of 3.3 seconds with the slit-width of $0.35''$ and pixel size along the solar-Y axis to be $0.1664''$ with slit length of $119''$. Every observation in this data-set has an exposure time of 3 seconds. The high cadence of these data-sets provides us a unique observation which is good enough to capture the high-frequency dynamics with high significance level.

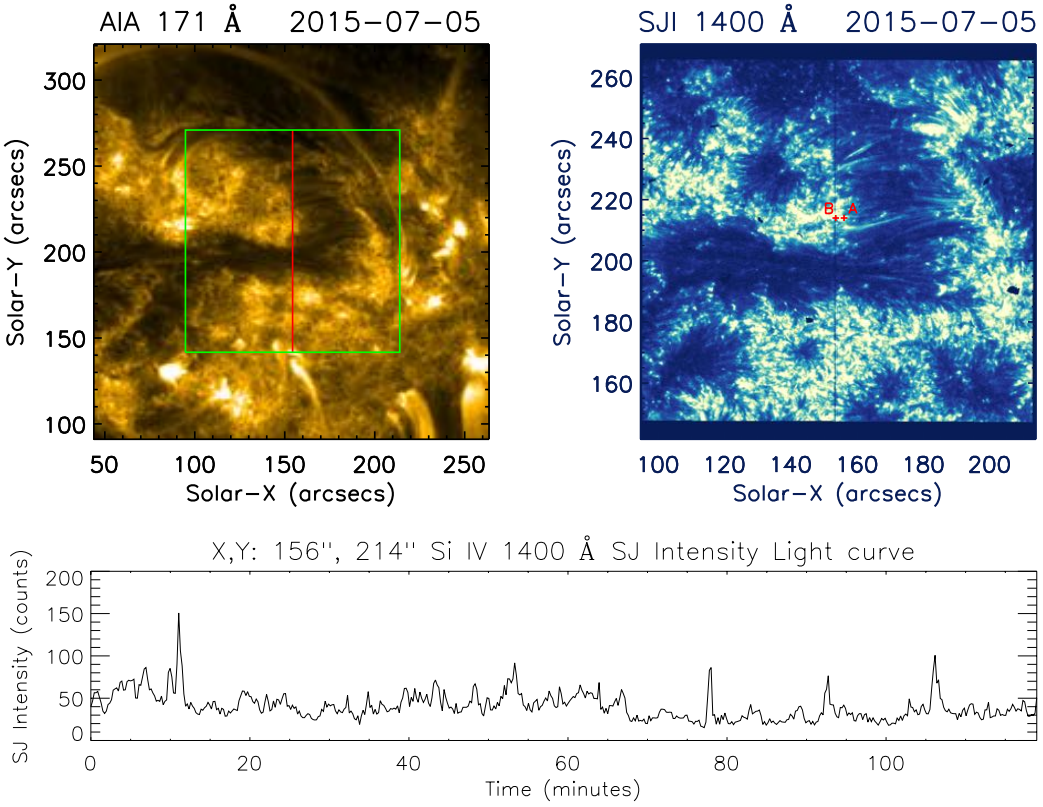

FIGURE 6.1: AIA 193 Å image marking the observed region by IRIS and SJI at a particular instance as observed by IRIS in the Si IV 1400 Å passband. The bottom panel shows the SJ intesity light curve at location A marked in SJI FOV for the complete duration of the observation.

From IRIS imaging data, we use SJIs in the Si IV 1400 Å passband which samples emission from the transition region (TR). For spectral analysis, we are concentrating on the Si IV (1403 Å) line formed at $log_{10}T \approx 4.9K$ which is one of the prominent TR emission line observed with IRIS and is free from other line blends. For density diagnostics, we use O IV (1401 Å) TR line along with Si IV (1403 Å) (Keenan *et al.* 2002; Young *et al.* 2018).

The calibrated level 2 data of IRIS is used in the study. Dark current subtraction, flat-field correction, and geometrical correction have been taken into account in the level 2 data. We employ wavelet analysis (Torrence and Compo 1998) and empirical mode decomposition (EMD; Huang *et al.* (1998)) techniques in order to detect and characterize the high-frequency oscillations in slit-jaw (SJ) intensity

(section 6.3.1) and different spectral properties *i.e.*, total intensity, peak intensity, Doppler velocity, and Doppler width (sections 6.3.2).

6.3 Data-Analysis and Results

6.3.1 Imaging Analysis from Si IV 1400 Å SJIs

Wavelet analysis is performed at each pixel location of SJ FOV to obtain the period of SJ intensity variability over the observed moss region. Figure 6.2 (a) shows a representative wavelet results corresponding to a pixel location marked as A in SJ FOV (Figure 6.1) for a duration of 20 minutes. As shown in Figure 6.1, a typical light curve for the entire duration possesses some instances of an abrupt increase in SJ intensity. Such intensity spikes are observed to be mostly random and non-repetitive in nature. On the other hand, the smaller amplitude intensity fluctuations are repetitive, hence in Figure 6.2 a, time-interval without the intensity spikes is shown for illustration. The top panel in Figure 6.2 (a) shows the variation of SJ intensity with time. The middle-panel shows the background (trend) subtracted intensity which is further used to obtain wavelet power spectrum (lower panels). Background (trend) is obtained by taking the 10-point running average of the intensity variation. The bottom left panels display a wavelet power spectrum (color inverted) with 99% significance levels and the bottom right panels display a global wavelet power spectrum (wavelet power spectrum summed over time) with 99% global significance.

The power spectra obtained reveals the presence of short-period variability in SJ intensity light-curve, with a distinct power peak at period of 1.6 min. It is important to note that even without considering the background trend, we obtain a power peak at the same period in wavelet spectra but with low significance level.

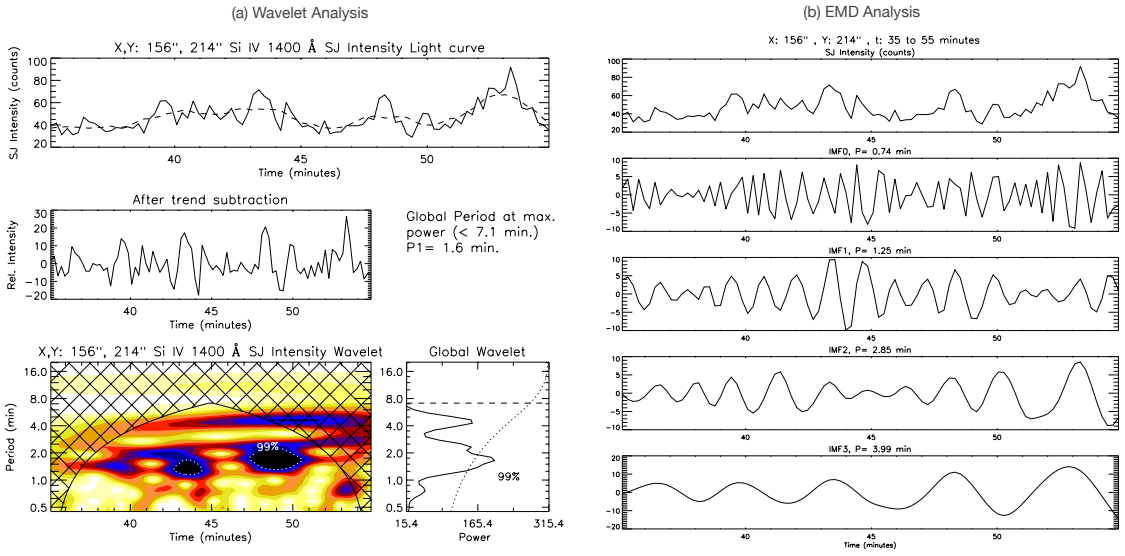

FIGURE 6.2: (a) Wavelet analysis, and (b) EMD analysis result for the Si IV 1400 Å SJ intensity variation with time from 35 to 55 minutes of the observation at location A. The details about the different panels are explained in the text (section 6.3.1).

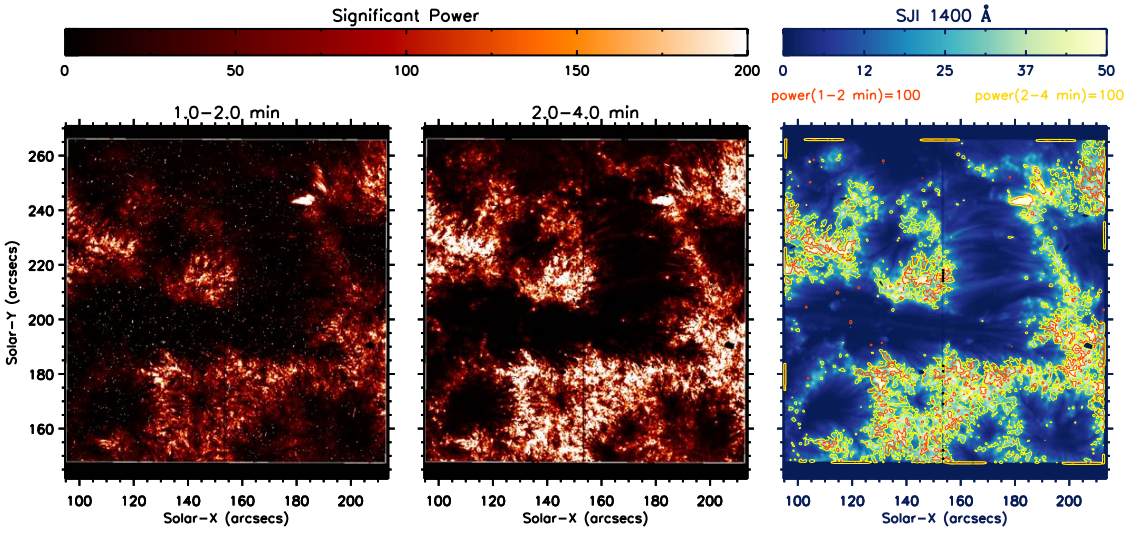

FIGURE 6.3: Power maps showing the significant power obtained from the Si IV 1400 Å SJ intensity variation in the period range of 1 to 2 minutes and 2 to 4 minutes. The rightmost panel shows average SJ intensity image with contours of significant power in 1-2 minutes periods in red and 2-4 minutes in yellow, delineating the bright regions of the moss.

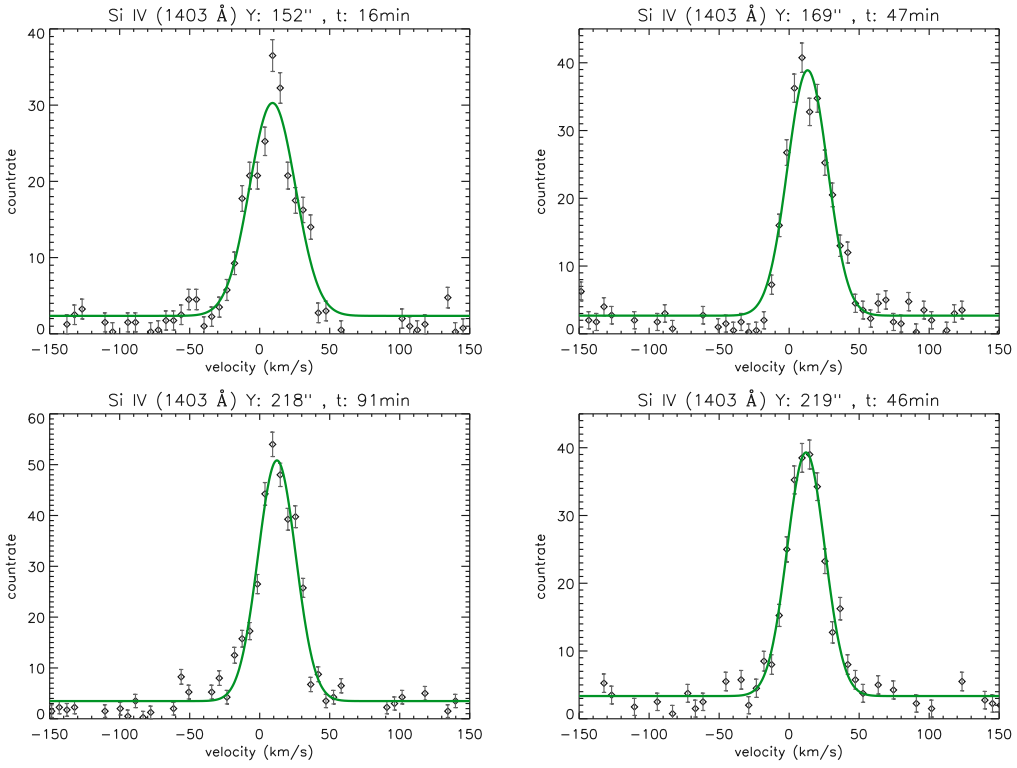

FIGURE 6.4: Typical spectral line profiles of Si IV 1403 Å emission line at various locations along the slit and at different instances of the observation.

Empirical mode decomposition (EMD) is also employed at few locations of SJ FOV. Figure 6.2 (b) shows the different intrinsic mode functions (IMFs) obtained from EMD for the same SJ light-curve as shown in Figure 6.2 (a). Here only first four IMFs are shown as the further IMFs contain the larger background trends. The dominant period (P) mentioned in the figure for each IMF is calculated using fast-Fourier transform (FFT). The period of first four IMFs for the particular example shown in Figure 6.2 (b) are 0.74 min, 1.25 min, 2.85 min and 3.99 min. The EMD analysis reinforces the detection of the presence of short periodicities (1–2 min) in the moss region as obtained by wavelet analysis. The presence of periodicities < 1 min can also be noted form the Figure 6.2, though these are below the significance level of 99% as shown in wavelet power spectra. Such oscillations have very small amplitudes, are present even for shorter-duration and could be damping fast. Hence, these oscillations with periods < 1 min may carry smaller amount of energy and may not be so important as that with periods > 1 min

which may be distributed over larger spatial and temporal extents. To verify this we now focus on distribution of power as calculated from wavelet method. We obtain the power maps of SJ intensity over the full FOV in 1–2 min and 2–4 min period intervals (Figure 6.3). On comparison of power maps with the SJ images (Figure 6.3) and AIA images (Figure 6.1), it can be observed that the significant power of high-frequency (1–2 min) as well as low-frequency (2–4 min) oscillations generally present only in bright regions of the moss. Figure 6.3 also shows the time-average SJI with the contours of significant power > 100 of 1–2 min variability in red and 2–4 min in yellow. The finer and smaller spatial extents of the contours at various locations over the field of view suggest that these oscillations posses high power in the localized regions within the bright moss. Moreover, the comparison of power between short (1–2 min) and long (2–4 min) periodicities, as showcased in Figure 6.3, reveals that the power in 1–2 min variability is, in general, less than that in 2–4 min.

6.3.2 Spectral Analysis from Si IV 1403 Å emission line

To characterize different periodicities present in the Si IV 1403 Å emission line, wavelet analysis is performed over the spectral parameters as obtained by fitting the single Gaussian fits to the Si IV 1403 Å line-profiles. Figure 6.4 shows few examples of the observed line-profiles with the single Gaussian fit for the illustration. Figure 6.5 (a) shows the wavelet maps of total intensity variation for a duration of 20 minutes at a particular location along the slit (marked as B in the SJ FOV in Figure 6.1). Total intensity signifies the summed intensity over the spectral profile range and is proportional to the product of peak intensity and Doppler width. Figure 6.6 (a) shows the wavelet maps of Doppler velocity at same location B and same time-interval as shown for total intensity in Figure 6.5. Note that the location B is in the very close neighbourhood of location A. Moreover, the same time-interval is shown in Figures 6.2, 6.5 and 6.6 for better illustration. Figure 6.7 shows the

variation of peak intensity, Doppler width, total intensity and Doppler velocity of Si IV 1403 Å line at location B along with the spectral line-profile at a particular instance. The animation of the figure is available at `https://www.dropbox.com/sh/i09ud4qvn28vmo3/AABYOVCqZv22Oak5iUbsyPuwa?dl=0` which shows the evolution of the spectral profile with time.

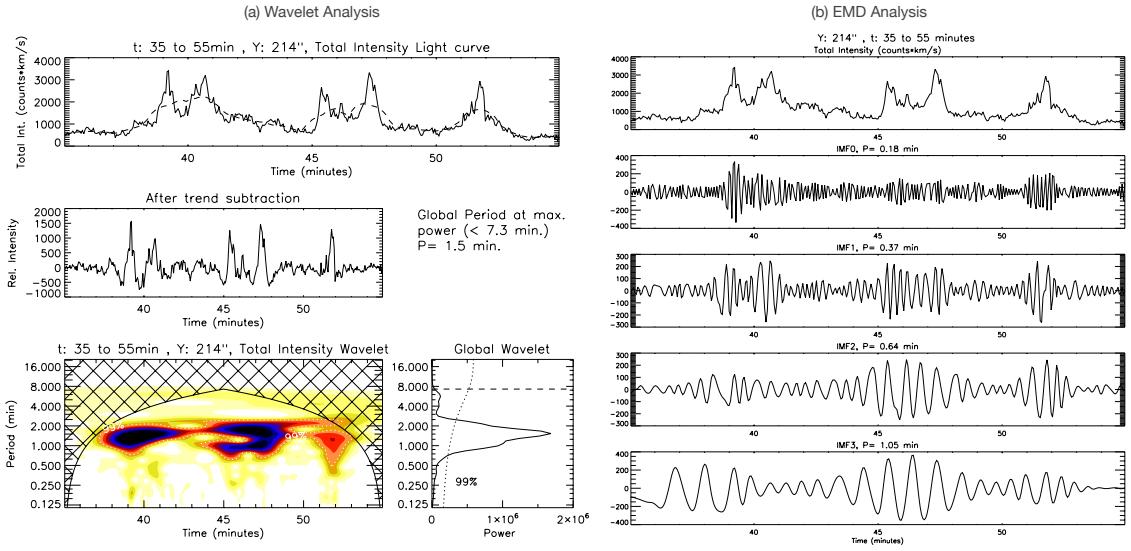

FIGURE 6.5: (a) Wavelet analysis, and (b) EMD analysis result for the Si IV 1403 Å total intensity variation with time from 35 to 55 minutes of the observation at location B along the slit.

The background trends for the spectral parameter light curves (Figures 6.5 and 6.6) are obtained by considering the 25-point running average of the light-curves. The dominant power peaks are observed to be present 1.5 min for total intensity, 1.7 min for peak intensity, 1.5 min for Doppler velocity, and 1.4 min for Doppler width in the respective power spectra. Here again, the presence periodicities of < 1 min can be seen in the wavelet. It can be clearly observed that such oscillations are present for very short durations and thus of not much significance over the longer durations. Also, such short periodicities could be due to the presence of noise which is picked up by wavelet at higher-frequencies. We produce power maps, shown in

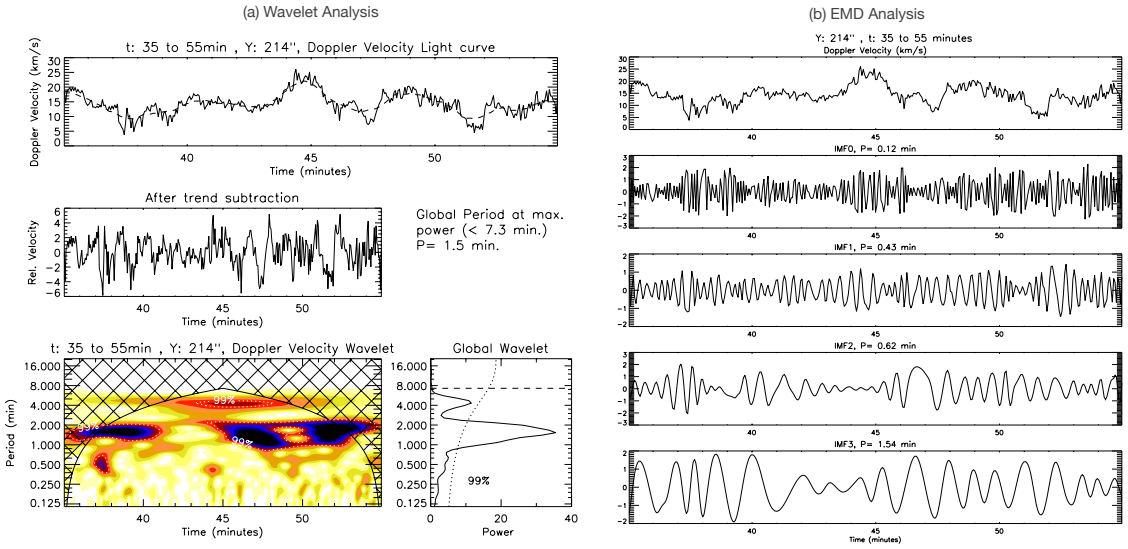

FIGURE 6.6: Same as figure 6.5 but for Doppler velocity

Figure 6.8 of the spectral parameters to study the distribution of power. The power maps clearly showcase the significant power along the slit, predominantly present in the period range of 0.83 to 2.36 min corresponding to pixel locations of moss regions (wherever the slit crosses the moss). This confirms the presence of short-period oscillations in Si IV 1403 Å spectra along with the Si IV 1400 Å SJ intensity (described in Section 6.3.1) in various locations of the moss region.

EMD technique is applied over the spectral variations in order to segregate the different periodicities present in their light curves. Figure 6.5 (b) and 6.6 (b) respectively shows the first four IMFs and their periods (P) of total intensity and Doppler velocity variation for a duration of 20 minutes at the location B, same location and time-interval as shown in Figure. The first four IMFs (IMF0, IMF1, IMF2, and IMF3) are observed to contain the short-period variabilities (0.2–2 min). The successive IMFs are observed to have periodicities of more than 2 min and hence of no interest for the present analysis. To perform a statistical study of correlation and phase-relationship between total intensity and Doppler velocity, we study their 20 different light-curves (cases), each of duration 20 minutes. These cases are selected to be located in the close neighbourhood of the power contours of 1–2 min periodicities (red contours in the average SJ image in Figure 6.3). The

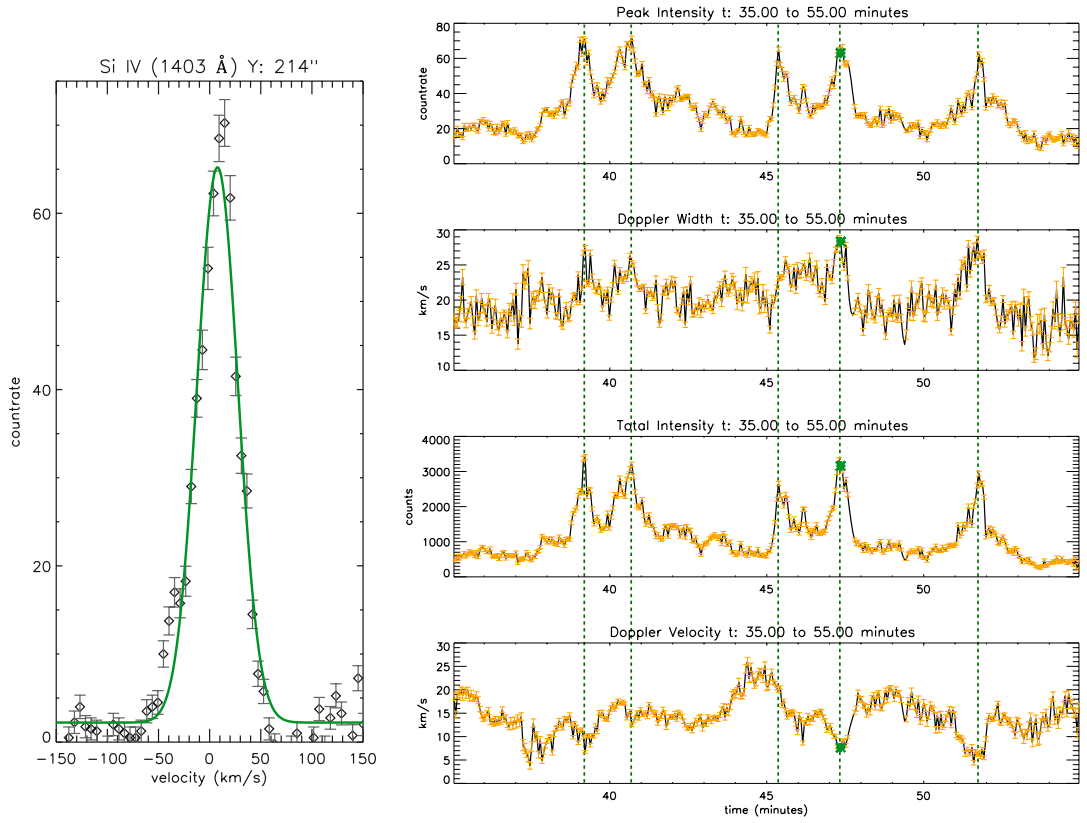

FIGURE 6.7: Left panel shows the observed spectral profiles (black symbols) of Si IV 1403 Å emission line at location B, with the Gaussian fit (green solid curve) for a particular instance. Panels on the right show the light-curves (in *black*) with the fitting errors (in *orange*) of different spectral parameters at B for a duration of 20 minutes. The *green* solid symbol over the light-curves marks the instant for which the spectral profile is shown in the left panel. The dotted lines shows some instances of the possible reconnection flows. An animation of this figure is available at `https://www.dropbox.com/sh/i09ud4qvn28vmo3/AABYOVCqZv22Oak5iUbsyPuwa?dl=0` which shows the evolution of the spectral profile with time.

locations of the selected cases are marked in *black* along the slit in the SJ image in Figure 6.3. Few specific time-intervals are considered at these locations in order to have further study about phase-relationship between total intensity and Doppler velocity.

Figure 6.9 shows the histograms of the period of oscillation for different IMFs of total intensity and Doppler velocity with the mean periods listed. As reflected by the value of mean periods, we will further regard the IMF0 to be associated with

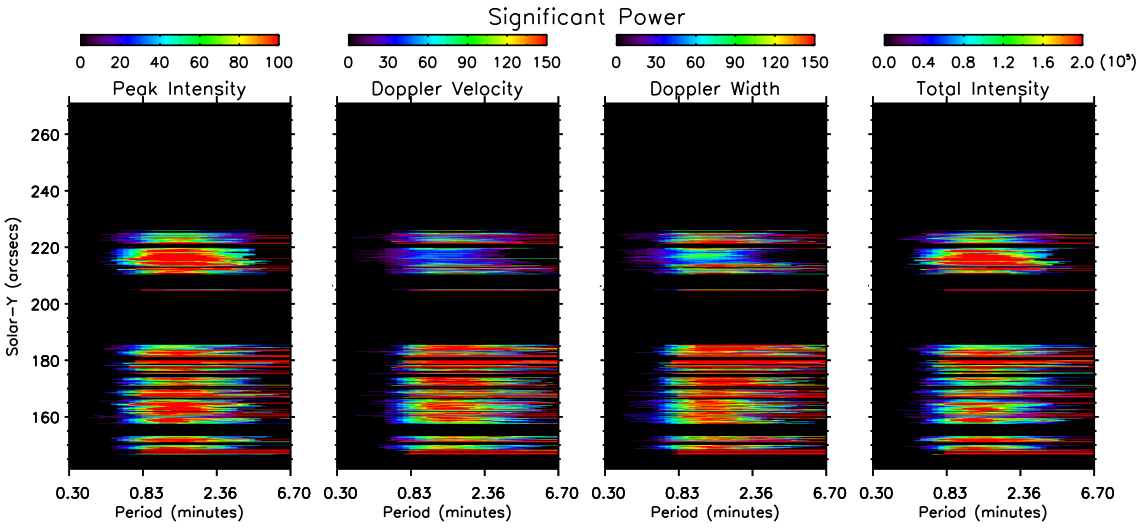

FIGURE 6.8: Power maps showing the significant power obtained from the variation of different spectral parameters of Si IV 1403 Å emission line in the period range of 0.3 to 6.7 minutes.

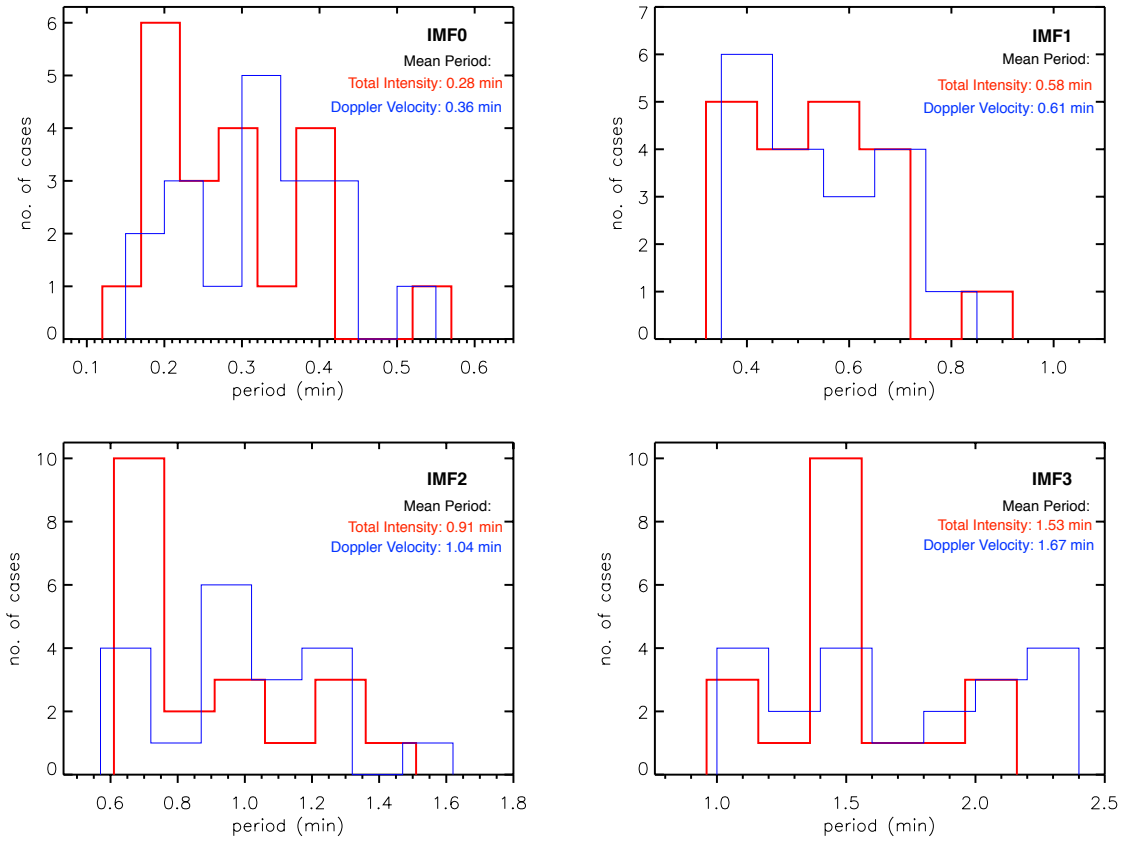

FIGURE 6.9: Histograms showing the distribution of periods of first four IMFs of total intensity in red and Doppler velocity in blue for the 20 selected cases.

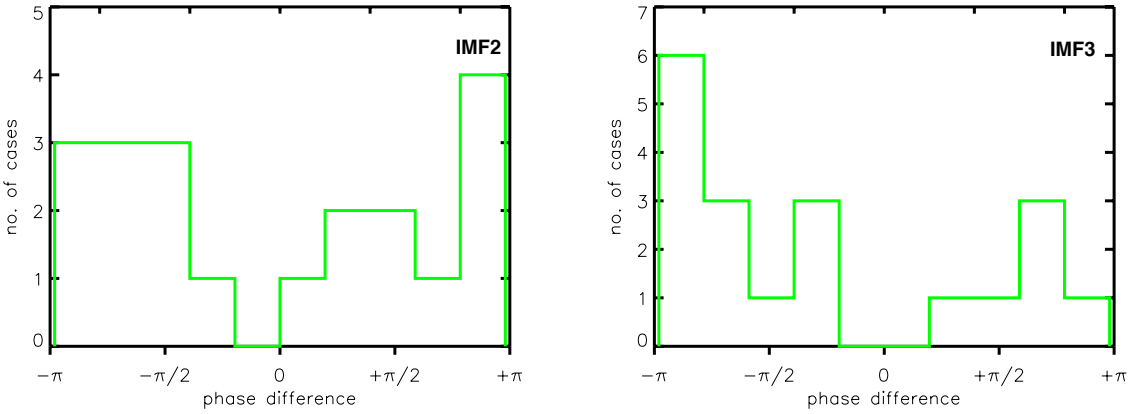

FIGURE 6.10: Histograms showing the distribution of phase-difference between total intensity and Doppler velocity for IMF2 nd IMF3 for the 20 selected cases.

the periodicity of ∼0.3 min, IMF1 with ∼0.6 min, IMF2 with ∼1.0 min and IMF3 with ∼1.6 min. The power maps in Figure 6.8 shows the absence of significant power in the periods below 0.6 min. Henceforth, for the further analysis about phase-relationship, we consider only the third and fourth IMFs, *i.e.*, IMF2 and IMF3. The phase-relation between total intensity and Doppler velocity at the short-periodicities is studied by correlating their respective IMFs for the 20 cases. Figure 6.10 shows the histograms of the phase difference between total intensity and Doppler velocity by considering IMF2 and IMF3. The histograms reveal the presence of phase-shifts in a wide range. The phase-shifts in the range of $\pi/4$ to $3\pi/4$ between total intensity and Doppler velocity indicates towards the presence of different wave modes. Whereas, the negligibly small phase-shifts ($<$ $\pi/4$) and large phase-shifts ($>$ $3\pi/4$) represent reconnection-like events. Such observed phase-relations shows that the MHD waves and repetitive reconnection, both can be held responsible for short-period variability in the different spectral parameters of the observed moss region.

The presence of phase shifts of $\sim \pm\pi$ indicate the presence of reconnection events. As shown in Figure 6.7, the increase in the intensity is accompanied by the increase in the Doppler width and decrease in Doppler velocity (blue-shifted flows,

De Pontieu *et al.* 2009; De Pontieu and McIntosh 2010) at many instances throughout the light-curve. Few of such instances are shown by vertical dotted lines in Figure 6.7. As shown in Figure 6.7, the instances of large amplitude fluctuations, which mostly have phase shift of $\sim \pi$ between Doppler velocity and total intensity, can be regarded as the clear signatures of quasi-periodic outflows (towards the observer) resulting from the reconnection process. The other instances of small amplitude fluctuations can be due the presence of slow magneto-acoustic waves. Very recently, Hansteen *et al.* (2014) and Brooks *et al.* (2016) have reported the presence of transition region fine loops with the aid of IRIS observations and numerical simulations. Such small scale loops with loop lengths of ∼1 to 2 Mm can harbour slow standing waves with periods of ∼1 min in transition region.

It is worth noting at this point that Wang *et al.* (2003); Taroyan *et al.* (2007); Taroyan and Bradshaw (2008) reported the presence of standing slow waves exclusively in hot coronal loops. In addition, Pant *et al.* (2017) reported the existence of standing slow waves in cool coronal loops (∼0.6 MK). In this work, we found evidence of the existence of slow waves in Si IV 1403 Å emission line whose formation temperature is ∼60000 K. In an ideal case, the phase-shift of $\sim\pm\pi/2$ is attributed to the presence of standing slow waves in the solar atmosphere (Wang *et al.* 2003; Taroyan *et al.* 2007; Taroyan and Bradshaw 2008; Moreels and Van Doorsselaere 2013). Further, it should be noted that the intensity and velocity changes phase in time due to the heating and cooling of the plasma (Taroyan and Bradshaw 2008) and due to presence of imperfect waveguides and drivers in reality, which deviates from the theoretical considerations (Keys *et al.* 2018). Thus the phase shift between intensity and velocity oscillations might differ in different regions and different time. This could be due to the intermittent nature of the flows and waves that might result in departure from the theoretically expected values of the phase-shifts. Hence we conjecture that the observed high-frequency oscillations are due to the presence of small-scale flows along with slow standing waves in TR fine loops. This supports both wave and reconnection like scenario

to be responsible for the periodicities of 1-2 min in moss regions.

6.3.3 Density diagnostics from Si IV 1403 Å and O IV 1401 Å emission lines

In order to obtain the information about density variations associated with the presence of waves and or reconnections flows, in the moss regions, we attempt to estimate density along the slit by using Si IV 1403 Å (λ = 1402.77 Å) and O IV 1401 Å (λ = 1401.16 Å) spectral lines from the IRIS spectra (as suggested by Young *et al.* (2018)). They introduced an empirical correction factor to normalize Si IV/O IV line intensity ratios. As first mentioned by Dupree (1972), the observed intensities of lines from the lithium and sodium-like iso-electronic sequences are usually stronger than that expected by the emission measures from other sequences formed at the same temperature. Doyle *et al.* (2005) showed that the electron density dependence of di-electronic recombination coupled with collisional ionization from metastable levels must be included while considering Li I like or Na I like lines. For example, Li I like C IV 1548 Å line shows a factor of three enhancement of intensity for the electron density of $\sim 10^{12}\, cm^{-3}$. Regarding Si IV and O IV lines, Doyle *et al.* (2013) showed that Si IV line intensity can be enhanced by a factor of 2–4, with the peak in the line contribution function occurring at a higher electron temperature due to transient ionization. On the other hand O IV line does not show such enhancement. Hence, such a correction factor is important to be applied to silicon line intensities. Table 2 of Young *et al.* (2018) gives the theoretical ratios of different lines after employing the correction factor (see QS DEM method as explained in Young *et al.* (2018); Young (2018)). We use Si IV (1402.77)/O IV (1401.16) line ratio from the table 2 of Young *et al.* (2018) for the estimation of electron density at a temperature of $log\ T/K = 4.88$ (temperature of maximum ionization of Si IV).

As O IV 1401 Å line is very weak in IRIS spectra, the spectra is averaged over every consecutive 7 pixels along the slit. In such averaging, for instance, the data value of the first 7 spatial pixels are replaced by their average value, the next 7 pixels are replaced by their respective average data-value, and so on. Similarly, time-averaging is also performed by considering 4 time steps along the temporal axis. In order to improve S/N, such averaging is performed only over O IV 1401 Å spectra as Si IV 1403 Å spectra contains significantly good signal. Figure 6.11 (a) and (b) shows the time-sequence maps of total intensity velocity along the slit for the Si IV 1403 Å and O IV 1401 Å line-profiles. A comparison between the two maps clearly shows that despite averaging the spectra (as explained above), we are able to obtain good S/N only for very few isolated O IV 1401 Å line-profiles in order to perform a reliable Gaussian fit, hence the total intensity values for O IV 1401 Å line is shown only for those isolated few pixels.

Figure 6.11(c) shows the theoretical Si IV (1403)/O IV (1401) ratio-density curve (Young *et al.* 2018) in *solid black* and the estimated density values are over-plotted in *magenta*. The density time-sequence map is also showcased in Figure 6.11(d). Note that we could estimate the density only at very few instances of some of the locations, as limited by the poor signal in O IV 1401 Å spectra. It can be observed in Figure 6.11(d) that we cannot find considerable examples of continuous density signal along time for some significant amount of duration over the entire observation. It is completely unreliable to perform any time series analysis over such light-curves. It appears that there are definite changes in the density but to relate that change with intensity and other line parameters for a definitive identification of the wave mode is beyond the quality of the current observations. Thus, we are still unable to obtain any results related to density oscillations with the present data.

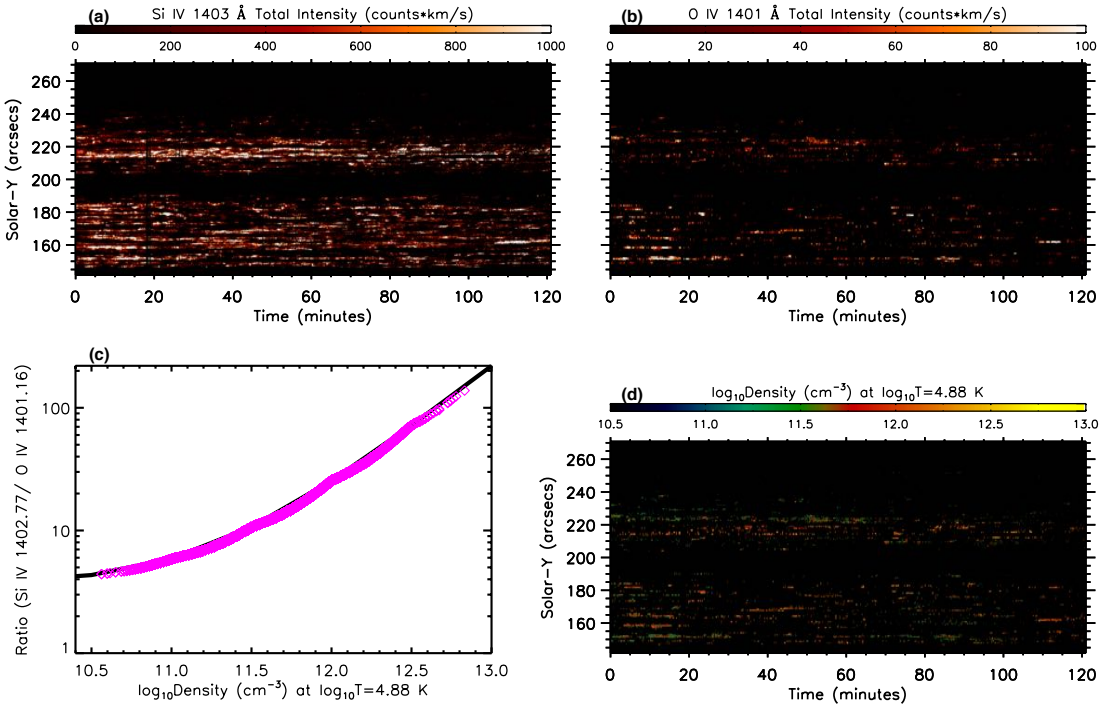

FIGURE 6.11: (a),(b) Time-sequence maps of total intensity of Si IV (1403 Å) and O IV (1401 Å) line. (c) Theoretical Si IV (1403)/O IV (1401) ratiodensity curve in *solid black* and the estimated values of the density in *magenta* corresponding to the observed ratios. (d) Time-sequence map of the estimated density.

6.4 Conclusions

In the present work, we study high-frequency dynamics of an active region moss by using high spatially and spectrally resolved observations of IRIS, with the fast cadence of 13 seconds for imaging and 3.3 seconds for spectral data. The techniques of wavelet and EMD analysis are employed in conjunction to explore the characteristics of the high-frequency oscillations. We have observed the persistent presence of periodicities in 1–2 min range in Si IV 1400 Å SJ intensity as well as in different spectral parameters (total intensity, peak intensity, Doppler velocity, and Doppler width) derived from Si IV 1403 Å emission line. The power maps

deduced from the SJ intensity variations show the concentration of power in short-periodicities generally in the bright regions of the moss. The power maps of the spectral parameters reveal the predominance of significant power in 1–2 min period range.

By adopting a statistical approach, we study phase-relationship of the high-frequency oscillations between total intensity and Doppler velocity. The observed phase-shifts, in the range of $\sim \pi/4$ to $3\pi/4$, supports the scenario of wave-like events. On the other hand, the phase shifts in the neighbourhood of zero and π supports the scenario of the nano-flare like events. In the case of approximately zero phase-shifts, the reconnection process results in near-simultaneous variation in the spectral parameters with the resultant mass flow projected away from the line-of-sight (red-shifts or positive Doppler velocity). In case of phase-shifts of $\sim \pi$, the reconnection process results in the mass flow projected towards the line-of-sight (blue-shifts or negative Doppler velocity). As the TR emission lines are red-shifted in general, the flows away from the line-of-sight will increase the value of the Doppler speeds with increase in the line intensity ($\sim$ zero phase-shift) due to reconnection process. Whereas, the flows towards the line-of-sight will appear to decrease the Doppler speeds with the increase in the intensity ($\sim \pi$ phase-shift). From the above discussions we conclude that the observed high-frequency oscillations in the bright moss regions are due to the combination of different wave modes and reconnection events.

As explained in section 6.3.3, we cannot obtain any reliable results from the density variations, although we are able to estimate the average density of the moss regions but to reliably study the density variation much better quality of data is required. Thus we are unable to confirm about the specific modes of the MHD waves, whether they are compressional in nature or non-compressional type. The high-frequency oscillations in the moss regions can be due to compressive (sausage) and/or in-compressive (kink/Alfv′enic) modes. The key to distinguish between

the different modes is to study the density oscillations which is not possible with present data because of low data-counts present in the O IV 1410 Å emission line. Some new instruments, with better sensitivity in the FUV wavelengths, especially in the density sensitive lines, may provide new insight and will enable us to specifically detect the particular wave modes responsible for such oscillations.

Chapter 7

Conclusions

The solar atmosphere above the photosphere is heated up to megakelvin temperatures and raised to a high level of dynamic activity through processes involving a pervading magnetic field. The different layers of the atmosphere are observed to be highly structured due to the presence of the solar magnetic field. This inhomogeneous and dynamic magnetic field gives rise to different features and events of various spatial scales and lifetimes throughout the atmosphere. The evolution of the complex magnetic structures at various scales in the different layers of the solar atmosphere determines the energetics of the atmosphere. In the recent past, small-scale features of sub-arcsecond sizes have gained more attention and importance and are being proposed to play a vital role in coronal heating and acceleration of solar wind. The technological advancements have provided new insight into the various properties of the rapidly evolving finer structures present in the atmosphere.

The chromosphere and transition region act as an interface between highly dense but cool photospheric plasma and hot low dense coronal plasma. Together, known as interface region, chromosphere and transition region play a key role in mass

and energy supply from photosphere to corona. These layers are home of various small-scale features and events which can be observed in different wavelength pass-bands (~ 6500 Å to 500 Å). Generally, these fine-scale structures are persistently observed throughout the solar surface with high occurrence rate and are thus important in the mass-energy cycle of the solar atmosphere. The complex interaction between the solar plasma and its magnetic field is responsible for such fascinating dynamic phenomena at finer spatial (sub-arcsec) and temporal (sub-minute) scales. In this thesis, I have studied some small-scale features observed in the interface region in an attempt to characterize their general properties statistically. Below, I have summarised the main results of the studies presented in the thesis. Recent developments in the field and possible future prospects are also discussed.

7.1 Main Results and Future Prospects

- ***Chromospheric Network Bright Points***: Recent dedicated *HINODE* polar campaigns revealed the presence of concentrated kilogauss patches of magnetic field in the polar regions of the Sun (Tsuneta *et al.* 2008a) which are also shown to be correlated with the facular bright-points at the photospheric level (Kaithakkal *et al.* 2013). We have demonstrated that this spatial intermittency of the magnetic field persists even up to the chromospheric heights. Using Ca H and SP observations of SOT, we observe very significant association between polar network bright-points and magnetic field concentrations. The network bright-points are also observed to be co-spatial with G-band bright-points or faculae. The maximum value of magnetic field strength reaches up to $\sim$1 kG within the bright-points. Despite covering only $\sim$0.5% of the total area, the bright-points posses the magnetic field $\sim$3.5 times that of the average magnetic field over the FOV. This led us to conclude that the

overall behaviour of polar magnetic field should be dictated by that under the network bright points.

Future attempts in the direction of relating the calcium intensity contrast of the network bright-points with the global value and behaviour of polar magnetic field are required (*e.g.* Priyal *et al.* (2014)). This, in turn, demand long-term availability of high-resolution observations of Sun's poles in Ca H or K pass-bands to build better statistics.

- ***Transition Region Network Jets***: Recent IRIS observations have revealed a prevalence of intermittent small-scale jets with apparent speeds of 80–250 km/s (Tian *et al.* 2014), emanating from small-scale bright regions inside network boundaries of coronal holes. We find that these network jets appear not only in coronal holes but also in quiet-sun regions. Using IRIS 1330 Å (C II) slit-jaw images, we extract several parameters of these network jets, *e.g.* apparent speed, length, lifetime and increase in foot-point brightness. Using several observations, we find that some properties of the jets are very similar but others are obviously different between the quiet sun and coronal holes. Our study shows that the coronal-hole jets appear to be faster and longer than those in the quiet sun. This can be directly attributed to a difference in the magnetic configuration of the two regions with open magnetic field lines rooted in coronal holes and magnetic loops often present in quiet sun. This proposed idea is well supported by our observations which clearly show some compact bright loops to be present in QS but generally absent in CH at TR heights. These small loop-like regions are generally devoid of network jets. In spite of different magnetic structures in the coronal hole and quiet sun in the transition region, there appears to be no substantial difference for the increase in foot-point brightness of the jets, which suggests that the generation mechanism of these network jets is likely the same in both regions.

Very recently, De Pontieu *et al.* (2017) have argued that the observed fast apparent motions of such jets are not the mass flows, but signatures of heating fronts travelling with Alfv′en speeds within the spicules (based on 2.5D radiative MHD numerical simulations by Martínez-Sykora *et al.* (2017)). Despite not being real mass flows, the observed demarcation (statistically, in speed and length) between CH and QS network jets is consistent with the numerical simulation by Iijima and Yokoyama (2015). They showed that the chromospheric or TR jets are projected farther outwards with higher speeds when overlying coronal gas pressure is lower (similar to that in coronal hole) and shorter when the coronal gas pressure is higher (similar to that in quiet sun), which agrees with our observations. This has also indicated that in the case of active region, where the coronal pressure is much higher, the jets would be even much shorter and have much lower speeds. This scenario can be explored further by performing a similar statistical comparison of active region jets with CH and QS jets.

- ***Two-Component Emission Lines in TR***: Emission lines originating from solar transition region often show deviations from the single Gaussian profile (Peter 2000, 2001). Our results clearly reveal that the solar TR is populated with highly dynamic small-scale features which manifest themselves in the form of the secondary component of emission line profiles. A very close spatial association is observed between the raster images of the three spectral properties with intensity in SJIs and LOS magnetic field in magnetograms. Our analysis shows that the double Gaussian fitting model is preferred over the single Gaussian model in bright network regions and neighbouring locations. Doppler velocity maps of single Gaussian fits and primary components of double Gaussian reveal the presence of some excess red and blue shifts in the ambient regions of the bright network. The secondary component of double Gaussian fits also shows high Doppler speeds ($> 20\,\mathrm{km/s}$) and small non-thermal widths ($< 40\,\mathrm{km/s}$) at these locations.

On comparison with SJIs, these locations can be seen to be associated with the complex jet structures and can be claimed as signatures of TR transients. From this study, we have concluded that the double Gaussian model fitting to the spectral profiles of TR emission lines is a significant requirement for a better understanding of the dynamics of TR transients.

Further explorations in this context can be performed in order to understand the relation between non-Gaussian spectral profiles and TR explosive events (EEs, Innes *et al.* (1997a,b)). EEs are observed to have similar non-Gaussian line profiles with one or two satellite (secondary) components. The observation of two-secondary components will prove as the direct detection of bi-directional jets resulting from the magnetic reconnection occurring at small spatial scales of $\sim 0.35''$. Such analysis will require three-component model fitting to the observed line-profiles which I plan to perform in near future.

- ***High-Frequency Oscillations in TR***: Using fast cadence observations of IRIS, we have studied the high-frequency dynamics of an active region moss. The persistent presence of periodicities in 1–2 min range in Si IV 1400 Å SJ intensity and in different spectral parameters (total intensity, peak intensity, Doppler velocity and Doppler width) derived from Si IV 1403 Å emission line indicate towards the omnipresence of such oscillations. The power maps deduced from the SJ intensity variations show the concentration of power in short-periodicities generally in the bright regions of the moss. The power maps of the spectral parameters reveal the predominance of significant power in 1–2 min period range. The statistical analysis of phase-relationship of the high-frequency oscillations shows a wide range of phase-shifts to be present between total intensity and Doppler velocity. The phase-shifts in the range of $\sim \pi/4$ to $3\pi/4$ shows the presence of different wave modes. On the other hand, the smaller ($< \pi/4$) and larger phase-shifts ($> 3\pi/4$) may represent reconnection-like events. This led us to conclude that the MHD waves and

repetitive reconnections, together, cause the high-frequency oscillations in the bright moss regions (Pant *et al.* 2015a; Samanta *et al.* 2016).

The high-frequency oscillations in the moss regions can be due to compressive (sausage) and/or in-compressive (kink/Alfv′enic) modes. Some new instruments, with better sensitivity in the FUV wavelengths, especially in the density sensitive lines, will help us in estimating the density and enable us to specifically detect the particular wave modes responsible for such oscillations. In order to obtain a complete picture of the characteristics of high-frequency oscillations, a similar analysis has to be performed simultaneously in different layers of the atmosphere. This requires co-spatial and co-temporal observations of the photosphere, chromosphere, transition region and corona with high resolution and faster cadence.

7.2 Final Remarks

For future exploration in the solar observational studies, we may need to focus on the upper TR, since the plasma in this temperature regime (0.1 MK–0.8 MK) has not been frequently observed before. Existing TR observations are mostly focused on the lower TR (∼0.02–0.1 MK). Since IRIS has almost no strong lines that form in the upper TR, it is unclear whether the dynamical features studied in the thesis are heated to temperatures higher than 0.1 MK. The upper TR is a key regime when considering mass and energy transport in the solar atmosphere. Still, it is the least investigated region of the solar atmosphere, due to technical limitations. New instruments which can achieve high-resolution (sub-arcsec) imaging and spectroscopic observations of the upper TR are highly desired in the future. For instance, higher-resolution spectroscopic observations of the upper TR will be achieved through the Spectral Investigation of the Coronal Environment instrument (SPICE; Fludra *et al.* (2013)) onboard the upcoming Solar Orbiter mission

(Marsch *et al.* 2005; Müller *et al.* 2013). High-resolution imaging and spectroscopic observations of the upper TR will enable us to continuously track the mass and energy from the lower atmosphere to the corona. Such observations will also help us to effectively monitor solar eruptions, and to understand the initiation and heating mechanisms of coronal mass ejections and solar flares.

Bibliography

Axford, W. I. and McKenzie, J. F., 1992, "The origin of high speed solar wind streams", in *Solar Wind Seven Colloquium*, (Eds.) Marsch, E., Schwenn, R., [ADS]

Bevington, P. R. and Robinson, D. K., 1992, *Data reduction and error analysis for the physical sciences*. [ADS]

Brooks, David H., Reep, Jeffrey W. and Warren, Harry P., 2016, "Properties and Modeling of Unresolved Fine Structure Loops Observed in the Solar Transition Region by IRIS", *Astrophys. J.*, **826**, L18. [DOI], [ADS], [arXiv:1606.05440 [astro-ph.SR]]

Carlsson, M. and Stein, R. F., 1997, "Formation of Solar Calcium H and K Bright Grains", *Astrophys. J.*, **481**, 500–514. [ADS]

Chen, Yajie, Tian, Hui, Huang, Zhenghua, Peter, Hardi and Samanta, Tanmoy, 2019, "Investigating the Transition Region Explosive Events and Their Relationship to Network Jets", *Astrophys. J.*, **873**(1), 79. [DOI], [ADS], [arXiv:1901.11215 [astro-ph.SR]]

Cranmer, S. R., 2009, "Coronal Holes", *Living Reviews in Solar Physics*, **6**, 3. [DOI], [ADS], [arXiv:0909.2847 [astro-ph.SR]]

Cranmer, S. R. and Woolsey, L. N., 2015, "Driving Solar Spicules and Jets with Magnetohydrodynamic Turbulence: Testing a Persistent Idea", *ArXiv e-prints*. [ADS], [arXiv:1509.03263 [astro-ph.SR]]

Culhane, J. L., Harra, L. K., James, A. M., Al-Janabi, K., Bradley, L. J., Chaudry, R. A., Rees, K., Tandy, J. A., Thomas, P., Whillock, M. C. R., Winter, B., Doschek, G. A., Korendyke, C. M., Brown, C. M., Myers, S., Mariska, J., Seely, J., Lang, J., Kent, B. J., Shaughnessy, B. M., Young, P. R., Simnett, G. M., Castelli, C. M., Mahmoud, S., Mapson-Menard, H., Probyn, B. J., Thomas, R. J., Davila, J., Dere, K., Windt, D., Shea, J., Hagood, R., Moye, R., Hara, H., Watanabe, T., Matsuzaki, K., Kosugi, T., Hansteen, V. and Wikstol, Ø., 2007, "The EUV Imaging Spectrometer for Hinode", *Solar Phys.*, **243**, 19–61. [DOI], [ADS]

de Pontieu, B., 1999, "Numerical simulations of spicules driven by weakly-damped Alfvén waves. I. WKB approach", *Astron. Astrophys.*, **347**, 696–710. [ADS]

De Pontieu, B. and McIntosh, S. W., 2010, "Quasi-periodic Propagating Signals in the Solar Corona: The Signature of Magnetoacoustic Waves or High-velocity Upflows?", *Astrophys. J.*, **722**, 1013–1029. [DOI], [ADS], [arXiv:1008.5300 [astro-ph.SR]]

de Pontieu, B., McIntosh, S., Hansteen, V. H., Carlsson, M., Schrijver, C. J., Tarbell, T. D., Title, A. M., Shine, R. A., Suematsu, Y., Tsuneta, S., Katsukawa, Y., Ichimoto, K., Shimizu, T. and Nagata, S., 2007, "A Tale of Two Spicules: The Impact of Spicules on the Magnetic Chromosphere", *Pub. Astron. Soc. Japan*, **59**, S655–S662. [DOI], [ADS], [arXiv:0710.2934]

De Pontieu, B., McIntosh, S. W., Hansteen, V. H. and Schrijver, C. J., 2009, "Observing the Roots of Solar Coronal Heating in the Chromosphere", *Astrophys. J. Lett.*, **701**, L1–L6. [DOI], [ADS], [arXiv:0906.5434 [astro-ph.SR]]

De Pontieu, B., Rouppe van der Voort, L., McIntosh, S. W., Pereira, T. M. D., Carlsson, M., Hansteen, V., Skogsrud, H., Lemen, J., Title, A., Boerner, P., Hurlburt, N., Tarbell, T. D., Wuelser, J. P., De Luca, E. E., Golub, L., McKillop, S., Reeves, K., Saar, S., Testa, P., Tian, H., Kankelborg, C., Jaeggli, S., Kleint, L. and Martinez-Sykora, J., 2014a, "On the prevalence of small-scale twist in

the solar chromosphere and transition region", *Science*, **346**, 1255732. [DOI], [ADS], [arXiv:1410.6862 [astro-ph.SR]]

De Pontieu, B., Title, A. M., Lemen, J. R., Kushner, G. D., Akin, D. J., Allard, B., Berger, T., Boerner, P., Cheung, M., Chou, C., Drake, J. F., Duncan, D. W., Freeland, S., Heyman, G. F., Hoffman, C., Hurlburt, N. E., Lindgren, R. W., Mathur, D., Rehse, R., Sabolish, D., Seguin, R., Schrijver, C. J., Tarbell, T. D., Wülser, J.-P., Wolfson, C. J., Yanari, C., Mudge, J., Nguyen-Phuc, N., Timmons, R., van Bezooijen, R., Weingrod, I., Brookner, R., Butcher, G., Dougherty, B., Eder, J., Knagenhjelm, V., Larsen, S., Mansir, D., Phan, L., Boyle, P., Cheimets, P. N., DeLuca, E. E., Golub, L., Gates, R., Hertz, E., McKillop, S., Park, S., Perry, T., Podgorski, W. A., Reeves, K., Saar, S., Testa, P., Tian, H., Weber, M., Dunn, C., Eccles, S., Jaeggli, S. A., Kankelborg, C. C., Mashburn, K., Pust, N., Springer, L., Carvalho, R., Kleint, L., Marmie, J., Mazmanian, E., Pereira, T. M. D., Sawyer, S., Strong, J., Worden, S. P., Carlsson, M., Hansteen, V. H., Leenaarts, J., Wiesmann, M., Aloise, J., Chu, K.-C., Bush, R. I., Scherrer, P. H., Brekke, P., Martinez-Sykora, J., Lites, B. W., McIntosh, S. W., Uitenbroek, H., Okamoto, T. J., Gummin, M. A., Auker, G., Jerram, P., Pool, P. and Waltham, N., 2014b, "The Interface Region Imaging Spectrograph (IRIS)", *Solar Phys.*, **289**, 2733–2779. [DOI], [ADS], [arXiv:1401.2491 [astro-ph.SR]]

De Pontieu, B., McIntosh, S., Martinez-Sykora, J., Peter, H. and Pereira, T. M. D., 2015, "Why is Non-Thermal Line Broadening of Spectral Lines in the Lower Transition Region of the Sun Independent of Spatial Resolution?", *Astrophys. J. Lett.*, **799**(1), L12. [DOI], [ADS], [arXiv:1710.06807 [astro-ph.SR]]

De Pontieu, Bart, Martínez-Sykora, Juan and Chintzoglou, Georgios, 2017, "What Causes the High Apparent Speeds in Chromospheric and Transition Region Spicules on the Sun?", *Astrophys. J.*, **849**, L7. [DOI], [ADS], [arXiv:1710.06803 [astro-ph.SR]]

Deng, N., Chen, X., Liu, C., Jing, J., Tritschler, A., Reardon, K. P., Lamb, D. A., Deforest, C. E., Denker, C., Wang, S., Liu, R. and Wang, H., 2015, "Chromospheric Rapid Blueshifted Excursions Observed with IBIS and their Association with Photospheric Magnetic Field Evolution", *Astrophys. J.*, **799**, 219. [DOI], [ADS], [arXiv:1412.4038 [astro-ph.SR]]

Dere, K. P. and Mason, H. E., 1993, "Nonthermal velocities in the solar transition zone observed with the high-resolution telescope and spectrograph", *Solar Phys.*, **144**, 217–241. [DOI], [ADS]

Dowdy, J. F., Jr., Rabin, D. and Moore, R. L., 1986, "On the Magnetic Structure of the Quiet Transition Region", *Solar Phys.*, **105**, 35–45. [DOI], [ADS]

Doyle, J. G., Summers, H. P. and Bryans, P., 2005, "The effect of metastable level populations on the ionization fraction of Li-like ions", *Astron. Astrophys.*, **430**, L29–L32. [DOI], [ADS]

Doyle, J. G., Giunta, A., Madjarska, M. S., Summers, H., O'Mullane, M. and Singh, A., 2013, "Diagnosing transient ionization in dynamic events", *Astron. Astrophys.*, **557**, L9. [DOI], [ADS], [arXiv:1307.8251 [astro-ph.SR]]

Dupree, A. K., 1972, "Analysis of the Extreme-Ultraviolet Quiet Solar Spectrum", *Astrophys. J.*, **178**, 527–542. [DOI], [ADS]

Egamberdiev, S. A., 1983, "The Placement of X-Ray Bright Points Relative to the Chromospheric Network", *Soviet Astronomy Letters*, **9**, 385–387. [ADS]

Fludra, A., Griffin, D., Caldwell, M., Eccleston, P., Cornaby, J., Drummond, D., Grainger, W., Greenway, P., Grundy, T., Howe, C., McQuirk, C., Middleton, K., Poyntz-Wright, O., Richards, A., Rogers, K., Sawyer, C., Shaughnessy, B., Sidher, S., Tosh, I., Beardsley, S., Burton, G., Marshall, A., Waltham, N., Woodward, S., Appourchaux, T., Philippon, A., Auchere, F., Buchlin, E., Gabriel, A., Vial, J. C., Schühle, U., Curdt, W., Innes, D., Meining, S., Peter, H., Solanki, S., Teriaca, L., Gyo, M., Büchel, V., Haberreiter, M., Pfiffner, D.,

Schmutz, W., Carlsson, M., Haugan, S. V., Davila, J., Jordan, P., Thompson, W., Hassler, D., Walls, B., Deforest, C., Hanley, J., Johnson, J., Phelan, P., Blecha, L., Cottard, H., Paciotti, G., Autissier, N., Allemand, Y., Relecom, K., Munro, G., Butler, A., Klein, R. and Gottwald, A., 2013, "SPICE EUV spectrometer for the Solar Orbiter mission", in *Solar Physics and Space Weather Instrumentation V*, Society of Photo-Optical Instrumentation Engineers (SPIE) Conference Series, 8862, [DOI], [ADS]

Fontenla, J. M., Avrett, E. H. and Loeser, R., 1990, "Energy balance in the solar transition region. I - Hydrostatic thermal models with ambipolar diffusion", *Astrophys. J.*, **355**, 700–718. [DOI], [ADS]

Frazier, E. N., 1970, "Multi-Channel Magnetograph Observations. II. Supergranulation", *Solar Phys.*, **14**, 89–111. [DOI], [ADS]

Fu, H., Xia, L., Li, B., Huang, Z., Jiao, F. and Mou, C., 2014, "Measurements of Outflow Velocities in on-disk Plumes from EIS/Hinode Observations", *Astrophys. J.*, **794**, 109. [DOI], [ADS], [arXiv:1408.5473 [astro-ph.SR]]

Gabriel, A. H., 1976, "A magnetic model of the solar transition region", *Philosophical Transactions of the Royal Society of London Series A*, **281**, 339–352. [DOI], [ADS]

Gandorfer, A., Grauf, B., Barthol, P., Riethmüller, T. L., Solanki, S. K., Chares, B., Deutsch, W., Ebert, S., Feller, A., Germerott, D., Heerlein, K., Heinrichs, J., Hirche, D., Hirzberger, J., Kolleck, M., Meller, R., Müller, R., Schäfer, R., Tomasch, G., Knölker, M., Martínez Pillet, V., Bonet, J. A., Schmidt, W., Berkefeld, T., Feger, B., Heidecke, F., Soltau, D., Tischenberg, A., Fischer, A., Title, A., Anwand, H. and Schmidt, E., 2011, "The Filter Imager SuFI and the Image Stabilization and Light Distribution System ISLiD of the Sunrise Balloon-Borne Observatory: Instrument Description", *Solar Phys.*, **268**, 35–55. [DOI], [ADS], [arXiv:1009.1037 [astro-ph.IM]]

Goodman, M. L., 2014, "Acceleration of Type 2 Spicules in the Solar Chromosphere. II. Viscous Braking and Upper Bounds on Coronal Energy Input", *Astrophys. J.*, **785**, 87. [DOI], [ADS], [arXiv:1403.2694 [astro-ph.SR]]

Gupta, G. R. and Tripathi, D., 2015, "IRIS and SDO Observations of Recurrent Explosive Events", *Astrophys. J.*, **809**, 82. [DOI], [ADS], [arXiv:1506.05327 [astro-ph.SR]]

Gupta, G. R., Teriaca, L., Marsch, E., Solanki, S. K. and Banerjee, D., 2012, "Spectroscopic observations of propagating disturbances in a polar coronal hole: evidence of slow magneto-acoustic waves", *Astron. Astrophys.*, **546**, A93. [DOI], [ADS], [arXiv:1209.3524 [astro-ph.SR]]

Habbal, S. R., Withbroe, G. L. and Dowdy, Jr., J. F., 1990, "A comparison between bright points in a coronal hole and a quiet-sun region", *Astrophys. J.*, **352**, 333–342. [DOI], [ADS]

Habbal, S. R., Woo, R. and Arnaud, J., 2001, "On the Predominance of the Radial Component of the Magnetic Field in the Solar Corona", *Astrophys. J.*, **558**, 852–858. [DOI], [ADS]

Hansteen, V., De Pontieu, B., Carlsson, M., Lemen, J., Title, A., Boerner, P., Hurlburt, N., Tarbell, T. D., Wuelser, J. P., Pereira, T. M. D., De Luca, E. E., Golub, L., McKillop, S., Reeves, K., Saar, S., Testa, P., Tian, H., Kankelborg, C., Jaeggli, S., Kleint, L. and Martínez-Sykora, J., 2014, "The unresolved fine structure resolved: IRIS observations of the solar transition region", *Science*, **346**, 1255757. [DOI], [ADS], [arXiv:1412.3611 [astro-ph.SR]]

Hansteen, V. H. and Velli, M., 2012, "Solar Wind Models from the Chromosphere to 1 AU", *Space Sci. Rev.*, **172**, 89–121. [DOI], [ADS]

Harvey, K. L., 1985, "The relationship between coronal bright points as seen in He I Lambda 10830 and the evolution of the photospheric network magnetic fields", *Australian Journal of Physics*, **38**, 875–883. [ADS]

Harvey, K. L. and Martin, S. F., 1973, "Ephemeral Active Regions", *Solar Phys.*, **32**, 389–402. [DOI], [ADS]

Harvey, K. L. and White, O. R., 1999, "Magnetic and Radiative Variability of Solar Surface Structures. I. Image Decomposition and Magnetic-Intensity Mapping", *Astrophys. J.*, **515**, 812–831. [DOI], [ADS]

He, J.-S., Tu, C.-Y. and Marsch, E., 2007, "Can the solar wind originate from a quiet Sun region?", *Astron. Astrophys.*, **468**, 307–312. [DOI], [ADS]

Hollweg, J. V., Jackson, S. and Galloway, D., 1982, "Alfven waves in the solar atmosphere. III - Nonlinear waves on open flux tubes", *Solar Phys.*, **75**, 35–61. [DOI], [ADS]

Hou, Z., Huang, Z., Xia, L., Li, B., Madjarska, M. S., Fu, H., Mou, C. and Xie, H., 2016, "Narrow-line-width UV Bursts in the Transition Region above Sunspots Observed by IRIS", *Astrophys. J. Lett.*, **829**, L30. [DOI], [ADS], [arXiv:1608.04892 [astro-ph.SR]]

Huang, N. E., Shen, Z., Long, S. R., Wu, M. C., Shih, H. H., Zheng, Q., Yen, N. C., Tung, C. C. and Liu, H. H., 1998, "The empirical mode decomposition and the Hilbert spectrum for nonlinear and non-stationary time series analysis", *Proceedings of the Royal Society of London Series A*, **454**, 903–998. [DOI], [ADS]

Huang, Z., Madjarska, M. S., Xia, L., Doyle, J. G., Galsgaard, K. and Fu, H., 2014, "Explosive Events on a Subarcsecond Scale in IRIS Observations: A Case Study", *Astrophys. J.*, **797**, 88. [DOI], [ADS], [arXiv:1409.6425 [astro-ph.SR]]

Huang, Z., Madjarska, M. S., Scullion, E. M., Xia, L.-D., Doyle, J. G. and Ray, T., 2017, "Explosive events in active region observed by IRIS and SST/CRISP", *Mon. Not. Roy. Astron. Soc.*, **464**, 1753–1761. [DOI], [ADS], [arXiv:1609.07698 [astro-ph.SR]]

Iijima, H. and Yokoyama, T., 2015, "Effect of coronal temperature on the scale of solar chromospheric jets", *ArXiv e-prints*. [ADS], [arXiv:1509.06677 [astro-ph.SR]]

Innes, D. E., Brekke, P., Germerott, D. and Wilhelm, K., 1997a, "Bursts of Explosive Events in the Solar Network", *Solar Phys.*, **175**, 341–348. [DOI], [ADS]

Innes, D. E., Inhester, B., Axford, W. I. and Wilhelm, K., 1997b, "Bi-directional plasma jets produced by magnetic reconnection on the Sun", *Nature*, **386**, 811–813. [DOI], [ADS]

Ishikawa, Shin-nosuke, Kubo, Masahito, Katsukawa, Yukio, Kano, Ryouhei, Narukage, Noriyuki, Ishikawa, Ryohko, Bando, Takamasa, Winebarger, Amy, Kobayashi, Ken, Trujillo Bueno, Javier and Auchère, Frédéric, 2017, "CLASP/SJ Observations of Rapid Time Variations in the Lyα Emission in a Solar Active Region", *Astrophys. J.*, **846**, 127. [DOI], [ADS]

Ito, H., Tsuneta, S., Shiota, D., Tokumaru, M. and Fujiki, K., 2010, "Is the Polar Region Different from the Quiet Region of the Sun?", *Astrophys. J.*, **719**, 131–142. [DOI], [ADS], [arXiv:1005.3667 [astro-ph.SR]]

Jafarzadeh, S., Solanki, S. K., Stangalini, M., Steiner, O., Cameron, R. H. and Danilovic, S., 2017, "High-frequency Oscillations in Small Magnetic Elements Observed with Sunrise/SuFI", *Astrophys. J. Suppl.*, **229**, 10. [DOI], [ADS], [arXiv:1611.09302 [astro-ph.SR]]

Jiao, F., Xia, L., Li, B., Huang, Z., Li, X., Chandrashekhar, K., Mou, C. and Fu, H., 2015, "Sources of Quasi-periodic Propagating Disturbances above a Solar Polar Coronal Hole", *Astrophys. J. Lett.*, **809**, L17. [DOI], [ADS], [arXiv:1507.08440 [astro-ph.SR]]

Judge, P. G., de Pontieu, B., McIntosh, S. W. and Olluri, K., 2012, "The Connection of Type II Spicules to the Corona", *Astrophys. J.*, **746**, 158. [DOI], [ADS], [arXiv:1112.6174 [astro-ph.SR]]

Kaithakkal, A. J., Suematsu, Y., Kubo, M., Shiota, D. and Tsuneta, S., 2013, "The Association of Polar Faculae with Polar Magnetic Patches Examined with Hinode Observations", *Astrophys. J.*, **776**, 122. [DOI], [ADS], [arXiv:1311.0980 [astro-ph.SR]]

Kano, R., Bando, T., Narukage, N., Ishikawa, R., Tsuneta, S., Katsukawa, Y., Kubo, M., Ishikawa, S.-n., Hara, H., Shimizu, T., Suematsu, Y., Ichimoto, K., Sakao, T., Goto, M., Kato, Y., Imada, S., Kobayashi, K., Holloway, T., Winebarger, A., Cirtain, J., De Pontieu, B., Casini, R., Trujillo Bueno, J., Štepán, J., Manso Sainz, R., Belluzzi, L., Asensio Ramos, A., Auchère, F. and Carlsson, M., 2012, "Chromospheric Lyman-alpha spectropolarimeter (CLASP)", in *Space Telescopes and Instrumentation 2012: Ultraviolet to Gamma Ray*, 8443, [DOI], [ADS]

Keenan, F. P., Ahmed, S., Brage, T., Doyle, J. G., Espey, B. R., Exter, K. M., Hibbert, A., Keenan, M. T. C., Madjarska, M. S., Mathioudakis, M. and Pollacco, D. L., 2002, "The OIV and SIV intercombination lines in the ultraviolet spectra of astrophysical sources", *Mon. Not. Roy. Astron. Soc.*, **337**, 901–909. [DOI], [ADS]

Keys, Peter H., Morton, Richard J., Jess, David B., Verth, Gary, Grant, Samuel D. T., Mathioudakis, Mihalis, Mackay, Duncan H., Doyle, John G., Christian, Damian J., Keenan, Francis P. and Erdélyi, Robertus, 2018, "Photospheric Observations of Surface and Body Modes in Solar Magnetic Pores", *Astrophys. J.*, **857**, 28. [DOI], [ADS], [arXiv:1803.01859 [astro-ph.SR]]

Kjeldseth Moe, O. and Nicolas, K. R., 1977, "Emission measures, electron densities, and nonthermal velocities from optically thin UV lines near a quiet solar limb", *Astrophys. J.*, **211**, 579–586. [DOI], [ADS]

Klimchuk, James A., 2006, "On Solving the Coronal Heating Problem", *Solar Phys.*, **234**, 41–77. [DOI], [ADS], [arXiv:astro-ph/0511841 [astro-ph]]

Kobayashi, K., Cirtain, J., Winebarger, A. R., Korreck, K., Golub, L., Walsh, R. W., De Pontieu, B., DeForest, C., Title, A., Kuzin, S., Savage, S., Beabout, D., Beabout, B., Podgorski, W., Caldwell, D., McCracken, K., Ordway, M., Bergner, H., Gates, R., McKillop, S., Cheimets, P., Platt, S., Mitchell, N. and

Windt, D., 2014, "The High-Resolution Coronal Imager (Hi-C)", *Solar Phys.*, **289**, 4393–4412. [DOI], [ADS]

Kosugi, T., Matsuzaki, K., Sakao, T., Shimizu, T., Sone, Y., Tachikawa, S., Hashimoto, T., Minesugi, K., Ohnishi, A., Yamada, T., Tsuneta, S., Hara, H., Ichimoto, K., Suematsu, Y., Shimojo, M., Watanabe, T., Shimada, S., Davis, J. M., Hill, L. D., Owens, J. K., Title, A. M., Culhane, J. L., Harra, L. K., Doschek, G. A. and Golub, L., 2007, "The Hinode (Solar-B) Mission: An Overview", *Solar Phys.*, **243**, 3–17. [DOI], [ADS]

Kudoh, T. and Shibata, K., 1999, "Alfvén Wave Model of Spicules and Coronal Heating", *Astrophys. J.*, **514**, 493–505. [DOI], [ADS]

Lemen, J. R., Title, A. M., Akin, D. J., Boerner, P. F., Chou, C., Drake, J. F., Duncan, D. W., Edwards, C. G., Friedlaender, F. M., Heyman, G. F., Hurlburt, N. E., Katz, N. L., Kushner, G. D., Levay, M., Lindgren, R. W., Mathur, D. P., McFeaters, E. L., Mitchell, S., Rehse, R. A., Schrijver, C. J., Springer, L. A., Stern, R. A., Tarbell, T. D., Wuelser, J.-P., Wolfson, C. J., Yanari, C., Bookbinder, J. A., Cheimets, P. N., Caldwell, D., Deluca, E. E., Gates, R., Golub, L., Park, S., Podgorski, W. A., Bush, R. I., Scherrer, P. H., Gummin, M. A., Smith, P., Auker, G., Jerram, P., Pool, P., Soufli, R., Windt, D. L., Beardsley, S., Clapp, M., Lang, J. and Waltham, N., 2012, "The Atmospheric Imaging Assembly (AIA) on the Solar Dynamics Observatory (SDO)", *Solar Phys.*, **275**, 17–40. [DOI], [ADS]

Loukitcheva, M., Solanki, S. K. and White, S. M., 2009, "The relationship between chromospheric emissions and magnetic field strength", *Astron. Astrophys.*, **497**, 273–285. [DOI], [ADS], [arXiv:0910.1985 [astro-ph.SR]]

Marsch, Eckart, Marsden, Richard, Harrison, Richard, Wimmer-Schweingruber, Robert and Fleck, Bernhard, 2005, "Solar Orbiter—mission profile, main goals and present status", *Advances in Space Research*, **36**, 1360–1366. [DOI], [ADS]

Martínez-Sykora, J., De Pontieu, B., Hansteen, V. and McIntosh, S. W., 2011a, "What do Spectral Line Profile Asymmetries Tell us About the Solar Atmosphere?", *Astrophys. J.*, **732**, 84. [DOI], [ADS]

Martínez-Sykora, J., Hansteen, V. and Moreno-Insertis, F., 2011b, "On the Origin of the Type II Spicules: Dynamic Three-dimensional MHD Simulations", *Astrophys. J.*, **736**, 9. [DOI], [ADS], [arXiv:1011.4703 [astro-ph.SR]]

Martínez-Sykora, J., Rouppe van der Voort, L., Carlsson, M., De Pontieu, B., Pereira, T. M. D., Boerner, P., Hurlburt, N., Kleint, L., Lemen, J., Tarbell, T. D., Title, A., Wuelser, J.-P., Hansteen, V. H., Golub, L., McKillop, S., Reeves, K. K., Saar, S., Testa, P., Tian, H., Jaeggli, S. and Kankelborg, C., 2015, "Internetwork Chromospheric Bright Grains Observed With IRIS and SST", *Astrophys. J.*, **803**, 44. [DOI], [ADS], [arXiv:1502.03490 [astro-ph.SR]]

Martínez-Sykora, J., De Pontieu, B., Hansteen, V. H., Rouppe van der Voort, L., Carlsson, M. and Pereira, T. M. D., 2017, "On the generation of solar spicules and Alfvénic waves", *Science*, **356**, 1269–1272. [DOI], [ADS], [arXiv:1710.07559 [astro-ph.SR]]

Matsumoto, T. and Shibata, K., 2010, "Nonlinear Propagation of Alfvén Waves Driven by Observed Photospheric Motions: Application to the Coronal Heating and Spicule Formation", *Astrophys. J.*, **710**, 1857–1867. [DOI], [ADS], [arXiv:1001.4307 [astro-ph.SR]]

McIntosh, S. W. and De Pontieu, B., 2009a, "Observing Episodic Coronal Heating Events Rooted in Chromospheric Activity", *Astrophys. J. Lett.*, **706**, L80–L85. [DOI], [ADS], [arXiv:0910.2452 [astro-ph.SR]]

McIntosh, S. W. and De Pontieu, B., 2009b, "High-Speed Transition Region and Coronal Upflows in the Quiet Sun", *Astrophys. J.*, **707**, 524–538. [DOI], [ADS], [arXiv:0910.5191 [astro-ph.SR]]

McIntosh, S. W., Innes, D. E., de Pontieu, B. and Leamon, R. J., 2010, "STEREO observations of quasi-periodically driven high velocity outflows in polar plumes", *Astron. Astrophys.*, **510**, L2. [DOI], [ADS], [arXiv:1001.3377 [astro-ph.SR]]

McLaughlin, J. A., Verth, G., Fedun, V. and Erdélyi, R., 2012, "Generation of Quasi-periodic Waves and Flows in the Solar Atmosphere by Oscillatory Reconnection", *Astrophys. J.*, **749**, 30. [DOI], [ADS], [arXiv:1203.6846 [astro-ph.SR]]

Mitalas, R. and Sills, K. R., 1992, "On the photon diffusion time scale for the sun", *Astrophys. J.*, **401**, 759. [DOI], [ADS]

Moreels, M. G. and Van Doorsselaere, T., 2013, "Phase relations for seismology of photospheric flux tubes", *Astron. Astrophys.*, **551**, A137. [DOI], [ADS]

Morton, R. J. and McLaughlin, J. A., 2013, "Hi-C and AIA observations of transverse magnetohydrodynamic waves in active regions", *Astron. Astrophys.*, **553**, L10. [DOI], [ADS], [arXiv:1305.0140 [astro-ph.SR]]

Morton, R. J. and McLaughlin, J. A., 2014, "High-resolution Observations of Active Region Moss and its Dynamics", *Astrophys. J.*, **789**, 105. [DOI], [ADS], [arXiv:1405.5694 [astro-ph.SR]]

Müller, D., Marsden, R. G., St. Cyr, O. C. and Gilbert, H. R., 2013, "Solar Orbiter . Exploring the Sun-Heliosphere Connection", *Solar Phys.*, **285**, 25–70. [DOI], [ADS], [arXiv:1207.4579 [astro-ph.SR]]

Murray, M. J., van Driel-Gesztelyi, L. and Baker, D., 2009, "Simulations of emerging flux in a coronal hole: oscillatory reconnection", *Astron. Astrophys.*, **494**, 329–337. [DOI], [ADS]

Narang, N., Arbacher, R. T., Tian, H., Banerjee, D., Cranmer, S. R., DeLuca, E. E. and McKillop, S., 2016, "Statistical Study of Network Jets Observed in the Solar Transition Region: a Comparison Between Coronal Holes and Quiet-Sun Regions", *Solar Phys.*, **291**, 1129–1142. [DOI], [ADS], [arXiv:1604.06295 [astro-ph.SR]]

Ni, L., Kliem, B., Lin, J. and Wu, N., 2015, "Fast Magnetic Reconnection in the Solar Chromosphere Mediated by the Plasmoid Instability", *Astrophys. J.*, **799**, 79. [DOI], [ADS]

Nindos, A. and Zirin, H., 1998, "The Relation of CA II K Features to Magnetic Field", *Solar Phys.*, **179**, 253–268. [DOI], [ADS]

Pant, V., Datta, A. and Banerjee, D., 2015a, "Flows and Waves in Braided Solar Coronal Magnetic Structures", *Astrophys. J. Lett.*, **801**, L2. [DOI], [ADS], [arXiv:1501.06507 [astro-ph.SR]]

Pant, V., Dolla, L., Mazumder, R., Banerjee, D., Krishna Prasad, S. and Panditi, V., 2015b, "Dynamics of On-disk Plumes as Observed with the Interface Region Imaging Spectrograph, the Atmospheric Imaging Assembly, and the Helioseismic and Magnetic Imager", *Astrophys. J.*, **807**, 71. [DOI], [ADS], [arXiv:1505.04473 [astro-ph.SR]]

Pant, V., Tiwari, A., Yuan, D. and Banerjee, D., 2017, "First Imaging Observation of Standing Slow Wave in Coronal Fan Loops", *Astrophys. J. Lett.*, **847**, L5. [DOI], [ADS], [arXiv:1708.06946 [astro-ph.SR]]

Parker, E. N., 1978, "Hydraulic concentration of magnetic fields in the solar photosphere. VI - Adiabatic cooling and concentration in downdrafts", *Astrophys. J.*, **221**, 368–377. [DOI], [ADS]

Parker, E. N., 1988, "Nanoflares and the Solar X-Ray Corona", *Astrophys. J.*, **330**, 474. [DOI], [ADS]

Parnell, C. E. and De Moortel, I., 2012, "A contemporary view of coronal heating", *Philosophical Transactions of the Royal Society of London Series A*, **370**, 3217–3240. [DOI], [ADS], [arXiv:1206.6097 [astro-ph.SR]]

Pastor Yabar, A., Martínez González, M. J. and Collados, M., 2018, "Magnetic topology of the north solar pole", *ArXiv e-prints*. [ADS], [arXiv:1804.09075 [astro-ph.SR]]

Pereira, T. M. D., De Pontieu, B., Carlsson, M., Hansteen, V., Tarbell, T. D., Lemen, J., Title, A., Boerner, P., Hurlburt, N., Wülser, J. P., Martínez-Sykora, J., Kleint, L., Golub, L., McKillop, S., Reeves, K. K., Saar, S., Testa, P., Tian, H., Jaeggli, S. and Kankelborg, C., 2014, "An Interface Region Imaging Spectrograph First View on Solar Spicules", *Astrophys. J. Lett.*, **792**, L15. [DOI], [ADS], [arXiv:1407.6360 [astro-ph.SR]]

Pesnell, W. D., Thompson, B. J. and Chamberlin, P. C., 2012, "The Solar Dynamics Observatory (SDO)", *Solar Phys.*, **275**, 3–15. [DOI], [ADS]

Peter, H., 2000, "Multi-component structure of solar and stellar transition regions", *Astron. Astrophys.*, **360**, 761–776. [ADS]

Peter, H., 2001, "On the nature of the transition region from the chromosphere to the corona of the Sun", *Astron. Astrophys.*, **374**, 1108–1120. [DOI], [ADS]

Peter, H., 2010, "Asymmetries of solar coronal extreme ultraviolet emission lines", *Astron. Astrophys.*, **521**, A51. [DOI], [ADS], [arXiv:1004.5403 [astro-ph.SR]]

Phillips, K. J. H., Feldman, U. and Landi, E., 2012, *Ultraviolet and X-ray Spectroscopy of the Solar Atmosphere*. [ADS]

Priest, E., 2014, *Magnetohydrodynamics of the Sun*. [ADS]

Priyal, Muthu, Banerjee, Dipankar, Karak, Bidya Binay, Muñoz-Jaramillo, Andrés, Ravindra, B., Choudhuri, Arnab Rai and Singh, Jagdev, 2014, "Polar Network Index as a Magnetic Proxy for the Solar Cycle Studies", *Astrophys. J.*, **793**, L4. [DOI], [ADS], [arXiv:1407.4944 [astro-ph.SR]]

Pucci, S., Poletto, G., Sterling, A. C. and Romoli, M., 2014, "Birth, Life, and Death of a Solar Coronal Plume", *Astrophys. J.*, **793**, 86. [DOI], [ADS]

Reale, Fabio, 2010, "Coronal Loops: Observations and Modeling of Confined Plasma", *Living Reviews in Solar Physics*, **7**, 5. [DOI], [ADS], [arXiv:1010.5927 [astro-ph.SR]]

Rezaei, R., Schlichenmaier, R., Beck, C. A. R., Bruls, J. H. M. J. and Schmidt, W., 2007, "Relation between photospheric magnetic field and chromospheric emission", *Astron. Astrophys.*, **466**, 1131–1144. [DOI], [ADS], [astro-ph/0701896]

Rieutord, M. and Rincon, F., 2010, "The Sun's Supergranulation", *Living Reviews in Solar Physics*, **7**, 2. [DOI], [ADS], [arXiv:1005.5376 [astro-ph.SR]]

Rouppe van der Voort, L., Leenaarts, J., de Pontieu, B., Carlsson, M. and Vissers, G., 2009, "On-disk Counterparts of Type II Spicules in the Ca II 854.2 nm and Hα Lines", *Astrophys. J.*, **705**, 272–284. [DOI], [ADS], [arXiv:0909.2115 [astro-ph.SR]]

Rouppe van der Voort, L., De Pontieu, B., Pereira, T. M. D., Carlsson, M. and Hansteen, V., 2015, "Heating Signatures in the Disk Counterparts of Solar Spicules in Interface Region Imaging Spectrograph Observations", *Astrophys. J. Lett.*, **799**, L3. [DOI], [ADS], [arXiv:1412.4531 [astro-ph.SR]]

Rutten, R. J., de Pontieu, B. and Lites, B., 1999, "Internetwork Grains with TRACE", in *High Resolution Solar Physics: Theory, Observations, and Techniques*, (Eds.) Rimmele, T. R., Balasubramaniam, K. S., Radick, R. R., Astronomical Society of the Pacific Conference Series, 183, [ADS]

Samanta, T., Banerjee, D. and Tian, H., 2015, "Quasi-periodic Oscillation of a Coronal Bright Point", *Astrophys. J.*, **806**, 172. [DOI], [ADS], [arXiv:1505.00587 [astro-ph.SR]]

Samanta, T., Singh, J., Sindhuja, G. and Banerjee, D., 2016, "Detection of High-Frequency Oscillations and Damping from Multi-slit Spectroscopic Observations of the Corona", *Solar Phys.*, **291**, 155–174. [DOI], [ADS], [arXiv:1511.07160 [astro-ph.SR]]

Scharmer, G. B., Narayan, G., Hillberg, T., de la Cruz Rodríguez, J., Löfdahl, M. G., Kiselman, D., Sütterlin, P., van Noort, M. and Lagg, A., 2008, "CRISP Spectropolarimetric Imaging of Penumbral Fine Structure", *Astrophys. J. Lett.*, **689**, L69–L72. [DOI], [ADS], [arXiv:0806.1638]

Schou, J., Scherrer, P. H., Bush, R. I., Wachter, R., Couvidat, S., Rabello-Soares, M. C., Bogart, R. S., Hoeksema, J. T., Liu, Y., Duvall, T. L., Akin, D. J., Allard, B. A., Miles, J. W., Rairden, R., Shine, R. A., Tarbell, T. D., Title, A. M., Wolfson, C. J., Elmore, D. F., Norton, A. A. and Tomczyk, S., 2012, "Design and Ground Calibration of the Helioseismic and Magnetic Imager (HMI) Instrument on the Solar Dynamics Observatory (SDO)", *Solar Phys.*, **275**, 229–259. [DOI], [ADS]

Schrijver, C. J., 1993, "Relations between the photospheric magnetic field and the emission from the outer atmosphere of cool stars. III - The chromospheric emission from individual flux tubes", *Astron. Astrophys.*, **269**, 395–402. [ADS]

Schrijver, C. J., 2001, "The Coronae of the Sun and Solar-type Stars (CD-ROM Directory: contribs/schrijv)", in *11th Cambridge Workshop on Cool Stars, Stellar Systems and the Sun*, (Eds.) Garcia Lopez, R. J., Rebolo, R., Zapaterio Osorio, M. R., Astronomical Society of the Pacific Conference Series, 223, [ADS]

Schrijver, C. J., Cote, J., Zwaan, C. and Saar, S. H., 1989a, "Relations between the photospheric magnetic field and the emission from the outer atmospheres of cool stars. I - The solar CA II K line core emission", *Astrophys. J.*, **337**, 964–976. [DOI], [ADS]

Schrijver, C. J., Dobson, A. K. and Radick, R. R., 1989b, "The magnetic, basal, and radiative-equilibrium components in Mount Wilson CA II H + K fluxes", *Astrophys. J.*, **341**, 1035–1044. [DOI], [ADS]

Sekse, D. H., Rouppe van der Voort, L. and De Pontieu, B., 2012, "Statistical Properties of the Disk Counterparts of Type II Spicules from Simultaneous Observations of Rapid Blueshifted Excursions in Ca II 8542 and Hα", *Astrophys. J.*, **752**, 108. [DOI], [ADS], [arXiv:1204.2943 [astro-ph.SR]]

Sekse, D. H., Rouppe van der Voort, L., De Pontieu, B. and Scullion, E., 2013, "Interplay of Three Kinds of Motion in the Disk Counterpart of Type II Spicules:

Upflow, Transversal, and Torsional Motions", *Astrophys. J.*, **769**, 44. [DOI], [ADS], [arXiv:1304.2304 [astro-ph.SR]]

Sheeley, Jr., N. R., Cooper, T. J. and Anderson, J. R. L., 2011, "Carrington Maps of Ca II K-line Emission for the Years 1915-1985", *Astrophys. J.*, **730**, 51. [DOI], [ADS]

Shetye, J., Doyle, J. G., Scullion, E., Nelson, C. J., Kuridze, D., Henriques, V., Woeger, F. and Ray, T., 2016, "High-cadence observations of spicular-type events on the Sun", *Astron. Astrophys.*, **589**, A3. [DOI], [ADS], [arXiv:1601.08087 [astro-ph.SR]]

Shibata, K., Nakamura, T., Matsumoto, T., Otsuji, K., Okamoto, T. J., Nishizuka, N., Kawate, T., Watanabe, H., Nagata, S., UeNo, S., Kitai, R., Nozawa, S., Tsuneta, S., Suematsu, Y., Ichimoto, K., Shimizu, T., Katsukawa, Y., Tarbell, T. D., Berger, T. E., Lites, B. W., Shine, R. A. and Title, A. M., 2007, "Chromospheric Anemone Jets as Evidence of Ubiquitous Reconnection", *Science*, **318**, 1591–. [DOI], [ADS], [arXiv:0810.3974]

Simon, G. W. and Leighton, R. B., 1964, "Velocity Fields in the Solar Atmosphere. III. Large-Scale Motions, the Chromospheric Network, and Magnetic Fields.", *Astrophys. J.*, **140**, 1120. [DOI], [ADS]

Singh, J., Hasan, S. S., Gupta, G. R., Nagaraju, K. and Banerjee, D., 2011, "Spectroscopic Observation of Oscillations in the Corona During the Total Solar Eclipse of 22 July 2009", *Solar Phys.*, **270**, 213–233. [DOI], [ADS]

Skogsrud, H., Rouppe van der Voort, L., De Pontieu, B. and Pereira, T. M. D., 2015, "On the Temporal Evolution of Spicules Observed with IRIS, SDO, and Hinode", *Astrophys. J.*, **806**, 170. [DOI], [ADS], [arXiv:1505.02525 [astro-ph.SR]]

Skumanich, A., Smythe, C. and Frazier, E. N., 1975, "On the statistical description of inhomogeneities in the quiet solar atmosphere. I - Linear regression analysis and absolute calibration of multichannel observations of the Ca/+/ emission network", *Astrophys. J.*, **200**, 747–764. [DOI], [ADS]

Solanki, S. K., Steiner, O. and Uitenbroeck, H., 1991, "Two-dimensional models of the solar chromosphere. I - The CA II K line as a diagnostic: 1.5-D radiative transfer", *Astron. Astrophys.*, **250**, 220–234. [ADS]

Spiegel, E. A. and Zahn, J.-P., 1992, "The solar tachocline", *Astron. Astrophys.*, **265**, 106–114. [ADS]

Suematsu, Y., Tsuneta, S., Ichimoto, K., Shimizu, T., Otsubo, M., Katsukawa, Y., Nakagiri, M., Noguchi, M., Tamura, T., Kato, Y., Hara, H., Kubo, M., Mikami, I., Saito, H., Matsushita, T., Kawaguchi, N., Nakaoji, T., Nagae, K., Shimada, S., Takeyama, N. and Yamamuro, T., 2008, "The Solar Optical Telescope of Solar-B (Hinode): The Optical Telescope Assembly", *Solar Phys.*, **249**, 197–220. [DOI], [ADS]

Taroyan, Y. and Bradshaw, S., 2008, "Coronal loop oscillations and diagnostics with Hinode/EIS", *Astron. Astrophys.*, **481**, 247–252. [DOI], [ADS]

Taroyan, Y., Erdélyi, R., Wang, T. J. and Bradshaw, S. J., 2007, "Forward Modeling of Hot Loop Oscillations Observed by SUMER and SXT", *Astrophys. J. Lett.*, **659**, L173–L176. [DOI], [ADS]

Testa, P., De Pontieu, B., Martínez-Sykora, J., DeLuca, E., Hansteen, V., Cirtain, J., Winebarger, A., Golub, L., Kobayashi, K., Korreck, K., Kuzin, S., Walsh, R., DeForest, C., Title, A. and Weber, M., 2013, "Observing Coronal Nanoflares in Active Region Moss", *Astrophys. J. Lett.*, **770**, L1. [DOI], [ADS], [arXiv:1305.1687 [astro-ph.SR]]

Thompson, W. T., 2006, "Coordinate systems for solar image data", *Astron. Astrophys.*, **449**, 791–803. [DOI], [ADS]

Tian, H., Marsch, E., Tu, C.-Y., Xia, L.-D. and He, J.-S., 2008a, "Sizes of transition-region structures in coronal holes and in the quiet Sun", *Astron. Astrophys.*, **482**, 267–272. [DOI], [ADS], [arXiv:0906.3028 [astro-ph.SR]]

Tian, H., Tu, C.-Y., Marsch, E., He, J.-S. and Zhou, G.-Q., 2008b, "Signature of mass supply to quiet coronal loops", *Astron. Astrophys.*, **478**, 915–919. [DOI], [ADS], [arXiv:0906.3007 [astro-ph.SR]]

Tian, H., Marsch, E., Curdt, W. and He, J., 2009, "Upflows in Funnel-like Legs of Coronal Magnetic Loops", *Astrophys. J.*, **704**, 883–890. [DOI], [ADS], [arXiv:0909.0739 [astro-ph.SR]]

Tian, H., McIntosh, S. W. and De Pontieu, B., 2011a, "The Spectroscopic Signature of Quasi-periodic Upflows in Active Region Timeseries", *Astrophys. J. Lett.*, **727**, L37. [DOI], [ADS], [arXiv:1012.5112 [astro-ph.SR]]

Tian, H., McIntosh, S. W., De Pontieu, B., Martínez-Sykora, J., Sechler, M. and Wang, X., 2011b, "Two Components of the Solar Coronal Emission Revealed by Extreme-ultraviolet Spectroscopic Observations", *Astrophys. J.*, **738**, 18. [DOI], [ADS], [arXiv:1106.1141 [astro-ph.SR]]

Tian, H., McIntosh, S. W., Habbal, S. R. and He, J., 2011c, "Observation of High-speed Outflow on Plume-like Structures of the Quiet Sun and Coronal Holes with Solar Dynamics Observatory/Atmospheric Imaging Assembly", *Astrophys. J.*, **736**, 130. [DOI], [ADS], [arXiv:1105.3119 [astro-ph.SR]]

Tian, H., DeLuca, E. E., Cranmer, S. R., De Pontieu, B., Peter, H., Martínez-Sykora, J., Golub, L., McKillop, S., Reeves, K. K., Miralles, M. P., McCauley, P., Saar, S., Testa, P., Weber, M., Murphy, N., Lemen, J., Title, A., Boerner, P., Hurlburt, N., Tarbell, T. D., Wuelser, J. P., Kleint, L., Kankelborg, C., Jaeggli, S., Carlsson, M., Hansteen, V. and McIntosh, S. W., 2014, "Prevalence of small-scale jets from the networks of the solar transition region and chromosphere", *Science*, **346**, 1255711. [DOI], [ADS], [arXiv:1410.6143 [astro-ph.SR]]

Torrence, C. and Compo, G. P., 1998, "A Practical Guide to Wavelet Analysis.", *Bulletin of the American Meteorological Society*, **79**, 61–78. [DOI], [ADS]

Tsuneta, S., Ichimoto, K., Katsukawa, Y., Lites, B. W., Matsuzaki, K., Nagata, S., Orozco Suárez, D., Shimizu, T., Shimojo, M., Shine, R. A., Suematsu, Y.,

Suzuki, T. K., Tarbell, T. D. and Title, A. M., 2008a, "The Magnetic Landscape of the Sun's Polar Region", *Astrophys. J.*, **688**, 1374–1381. [DOI], [ADS], [arXiv:0807.4631]

Tsuneta, S., Ichimoto, K., Katsukawa, Y., Nagata, S., Otsubo, M., Shimizu, T., Suematsu, Y., Nakagiri, M., Noguchi, M., Tarbell, T., Title, A., Shine, R., Rosenberg, W., Hoffmann, C., Jurcevich, B., Kushner, G., Levay, M., Lites, B., Elmore, D., Matsushita, T., Kawaguchi, N., Saito, H., Mikami, I., Hill, L. D. and Owens, J. K., 2008b, "The Solar Optical Telescope for the Hinode Mission: An Overview", *Solar Phys.*, **249**, 167–196. [DOI], [ADS], [arXiv:0711.1715]

Tu, C.-Y., Zhou, C., Marsch, E., Xia, L.-D., Zhao, L., Wang, J.-X. and Wilhelm, K., 2005, "Solar Wind Origin in Coronal Funnels", *Science*, **308**, 519–523. [DOI], [ADS]

Uritsky, V. M., Davila, J. M., Viall, N. M. and Ofman, L., 2013, "Measuring Temperature-dependent Propagating Disturbances in Coronal Fan Loops Using Multiple SDO/AIA Channels and the Surfing Transform Technique", *Astrophys. J.*, **778**, 26. [DOI], [ADS], [arXiv:1308.6195 [astro-ph.SR]]

van Ballegooijen, A. A., Asgari-Targhi, M., Cranmer, S. R. and DeLuca, E. E., 2011, "Heating of the Solar Chromosphere and Corona by Alfvén Wave Turbulence", *Astrophys. J.*, **736**, 3. [DOI], [ADS], [arXiv:1105.0402 [astro-ph.SR]]

Vernazza, J. E., Avrett, E. H. and Loeser, R., 1981, "Structure of the solar chromosphere. III - Models of the EUV brightness components of the quiet-sun", *Astrophys. J. Suppl.*, **45**, 635–725. [DOI], [ADS]

Waldmeier, M., 1956, "Synoptische Karten der Sonnenkorona. Mit 16 Textabbildungen", *Z. Astrophys.*, **38**, 219. [ADS]

Wang, T. J., Solanki, S. K., Curdt, W., Innes, D. E., Dammasch, I. E. and Kliem, B., 2003, "Hot coronal loop oscillations observed with SUMER: Examples and statistics", *Astron. Astrophys.*, **406**, 1105–1121. [DOI], [ADS]

Wang, X., McIntosh, S. W., Curdt, W., Tian, H., Peter, H. and Xia, L.-D., 2013, "Temperature dependence of ultraviolet line parameters in network and internetwork regions of the quiet Sun and coronal holes", *Astron. Astrophys.*, **557**, A126. [DOI], [ADS]

Webb, D. F., Martin, S. F., Moses, D. and Harvey, J. W., 1993, "The correspondence between X-ray bright points and evolving magnetic features in the quiet sun", *Solar Phys.*, **144**, 15–35. [DOI], [ADS]

Wedemeyer-Böhm, S., Lagg, A. and Nordlund, Å., 2009, "Coupling from the Photosphere to the Chromosphere and the Corona", *Space Sci. Rev.*, **144**, 317–350. [DOI], [ADS], [arXiv:0809.0987]

Wiegelmann, T. and Solanki, S. K., 2004, "Similarities and Differences between Coronal Holes and the Quiet Sun: Are Loop Statistics the Key?", *Solar Phys.*, **225**, 227–247. [DOI], [ADS], [arXiv:0802.0120]

Wilhelm, K., Curdt, W., Marsch, E., Schühle, U., Lemaire, P., Gabriel, A., Vial, J.-C., Grewing, M., Huber, M. C. E., Jordan, S. D., Poland, A. I., Thomas, R. J., Kühne, M., Timothy, J. G., Hassler, D. M. and Siegmund, O. H. W., 1995, "SUMER - Solar Ultraviolet Measurements of Emitted Radiation", *Solar Phys.*, **162**, 189–231. [DOI], [ADS]

Yang, L., He, J., Peter, H., Tu, C., Chen, W., Zhang, L., Marsch, E., Wang, L., Feng, X. and Yan, L., 2013, "Injection of Plasma into the Nascent Solar Wind via Reconnection Driven by Supergranular Advection", *Astrophys. J.*, **770**, 6. [DOI], [ADS]

Young, P. R., 2018, "Element Abundance Ratios in the Quiet Sun Transition Region", *Astrophys. J.*, **855**, 15. [DOI], [ADS], [arXiv:1801.05886 [astro-ph.SR]]

Young, P. R., Keenan, F. P., Milligan, R. O. and Peter, H., 2018, "A Si IV/O IV Electron Density Diagnostic for the Analysis of IRIS Solar Spectra", *Astrophys. J.*, **857**, 5. [DOI], [ADS], [arXiv:1803.01721 [astro-ph.SR]]

Yurchyshyn, V., Abramenko, V. and Goode, P., 2013, "Dynamics of Chromospheric Upflows and Underlying Magnetic Fields", *Astrophys. J.*, **767**, 17. [DOI], [ADS], [arXiv:1303.4766 [astro-ph.SR]]